BROADBAND HIGH-GAIN PLANAR LEAKY-WAVE ANTENNAS

by

Alexandros Feresidis, BSc, MSc

A Doctoral Thesis

Submitted in partial fulfilment of the requirements for the award of the degree of Doctor of Philosophy by Loughborough University

1 May 2002

Department of Electronic and Electrical Engineering
Loughborough University
United Kingdom

To my parents

Abstract

High-gain, low cost, planar antennas have attracted a lot of interest in recent years, with regard to applications as fixed wireless access, satellite reception and various point-to-point radio links. Microstrip patch arrays have primarily been good candidates, but the complex feeding mechanisms degrade the antenna performance. A method of producing a high gain planar antenna with a simple feed has been proposed in an earlier study. This technique utilises a partially reflective surface (PRS) to introduce a leaky wave and beamforming effect when placed in front of a waveguide aperture in a ground plane. The partial reflection can be obtained from periodic arrays, also referred to as Frequency Selective Surfaces (FSSs) when used for their filtering properties. The research effort in this thesis focuses on the theory underpinning the beamforming effect of single and double-layer PRSs in a leaky-wave antenna configuration and subsequently on novel leaky-wave antenna designs.

An approximate theoretical model was initially used to obtain an insight of the physical behaviour of the antenna. The performance of the antenna was related to the reflection characteristics of the PRS, which were calculated using a plane wave modal analysis. The results of this study were used as guidelines to produce optimised single and double layer array designs for both high gain and broad bandwidth. The effect of the size of the PRS on the antenna performance has been investigated and the antenna in its entirety was simulated using 3-D time domain codes. Further improvements on the antenna performance have been achieved by optimising the feed. An open cavity has also been used to suppress the side-lobes and increase the gain further. Lastly, a multiple feed configuration has been proposed based on simulation results.

Keywords – High-Gain Antennas, Leaky-Wave Antennas, Arrays, Frequency Selective Surfaces (FSS), Microwave Links

Acknowledgements

I would like to thank my supervisor, Professor Yiannis Vardaxoglou, for his help and encouragement throughout the research.

I would like to acknowledge the kind provision of the Cray J90 computer by Advantica (formerly British Gas).

I extend my thanks to all the technical and administrative staff for their support in this research, especially Neville Carpenter, Peter Barrington, Mark Snape and Susan Dart.

I am deeply indebted to Dr Dave Lockyer for his help and useful advice and to Pádraig McEvoy for his friendship, help and constant encouragement.

I would also like to thank all my colleagues in the Wireless Communications group at Loughborough, Richard, Mohan, Alford, Gavin, Chin, Nikos. Their help and support in the course of the research was very important.

Special thanks to Christina Koutsari, Argyris Zolotas and Vivi Pouli who, apart from being good friends, they were also a constant source of help and encouragement.

Last but not least, I would like to thank my parents for their love and encouragement all these years.

Publications from the research

Conferences

[1] COX, G.J., FERESIDIS, A. and VARDAXOGLOU, J.C. : 'Leaky Wave Action of Planar and Cylindrical FSS', Proc. PREP 2000, 2^{nd} Conference on Postgraduate Research in Electronics, Photonics and Related Fields, IEE, University of Nottingham, April 2000, pp. 273-278

[2] FERESIDIS, A. and VARDAXOGLOU, J.C.: 'Flat plate millimetre wave antenna based on partially reflective FSS', Proc. IEE International Conference on Antennas and Propag., ICAP, April 2001, Manchester, UK, pp. 33-36

[3] FERESIDIS, A. P. and VARDAXOGLOU, J. C. : 'Double layer partially reflective surfaces for high gain planar antennas', Proc. IEEE International Conference on Electromagnetics in Advanced Applications (ICEAA), Torino, Italy, September 2001, pp. 243-246

Journals

[1] FERESIDIS, A. P. and VARDAXOGLOU, J. C. : 'High gain planar antenna using optimised partially reflective surfaces', *IEE Proc., Microw., Antennas & Propag.*, vol. 148, No. 6, Dec. 2001, pp. 345-350

[2] FERESIDIS, A. P. and VARDAXOGLOU, J. C. : 'Bandwidth enhancement method for planar leaky-wave antennas', in preparation.

Contents

Chapter 1

Introduction

1.1 Background

Modern fixed and mobile communication systems require high-gain antennas which are small, easy to deploy and have low fabrication costs. Applications include fixed wireless access, such as the Local Multipoint Distribution System (LMDS), radio relay systems for connecting mobile base stations and direct broadcast satellite (DBS) systems. Reflector type antennas exhibit high gain and have been widely used throughout the past years in satellite and fixed communication systems [1]. Flat antenna arrays offer an attractive alternative that meets all requirements. Planar antennas offer several advantages over reflector antennas. Lower profile, lighter weight and better aesthetics are among the benefits. The implementation of planar antennas in multi-layer printed circuit structures adds the advantages of low cost fabrication and easier integration of antenna electronics such as RF circuits for electronic beam steering.

Flat plate antennas have been produced in recent years, using slotted-waveguide arrays [2]. However, the high manufacturing cost of the waveguides has been a key problem with these antennas. Microstrip patch arrays have been extensively researched in the last two decades for high-gain planar antenna applications [3-5]. A significant advantage of patch arrays is their implementation in printed circuit structures. However, the complex microstrip feed network in patch arrays incurs both gain loss and degradation in sidelobe and cross polarisation due to resistive loss and feed radiation [6, 7]. In particular, a reduction in gain and efficiency values occurs due to ohmic and dielectric losses in the feed lines and losses due to feed radiation, surface waves and manufacturing tolerance errors. The spurious radiation from the discontinuities in the feed lines also increase the sidelobe level and the cross-polar radiation.

An alternative way of producing a high gain planar antenna using a simple feed has been first introduced by Trentini [8] and further studied by James *et al.* [9]. Trentini first demonstrated how partially reflective planar arrays can significantly increase the directivity of a grounded waveguide aperture when placed at a certain distance in front of the ground plane. James *et al* presented an experimental investigation on the effect of multiple layer arrays on the directivity of a grounded waveguide aperture as well as a printed patch antenna.

The technique presented in both of the above papers dispenses with complex microstrip feed line networks used in patch array antennas. The radiation mechanism is based on a leaky-wave and beamforming effect introduced by the partially reflective screen when placed in front of the ground plane. This type of leaky-wave has also been observed in superimposed dichroic microstrip antenna arrays [10], as well as in waveguides with partially reflecting walls [11, 12]. The partial reflection in all these leaky-wave structures can be obtained from periodic arrays of passive elements (conducting patches or apertures in a conducting plane). The main impetus in this thesis is to study the beamforming effect of single and double layer arrays in a leaky-wave antenna configuration and produce novel leaky-wave antenna designs (see section 1.3 for a detailed overview). A brief introduction on planar periodic arrays is given in the next section.

1.2 Introduction to Passive Planar Periodic Arrays

Planar periodic arrays consist of identical elements arranged in a two dimensional doubly periodic grid. When used in a passive form, e.g. excited under plane wave illumination, they behave as electromagnetic filters [13]. In this case they are normally referred to as Frequency Selective Surfaces (FSS) or dichroic surfaces and they find a large number of applications in antennas for fixed and mobile communication systems [13, 14]. A large variety of elements can be used such as dipoles, cross dipoles, tripoles, square patches or loops, and rings. Each element exhibits a characteristic reflection/transmission response due to its geometry. For example tripole and loop elements exhibit a better angular stability and larger reflection/transmission bandwidths (at resonance) as compared to dipoles and patches. The choice of the element depends on the application and the desired design features. Some examples of element geometries are shown in Fig. 1.1.

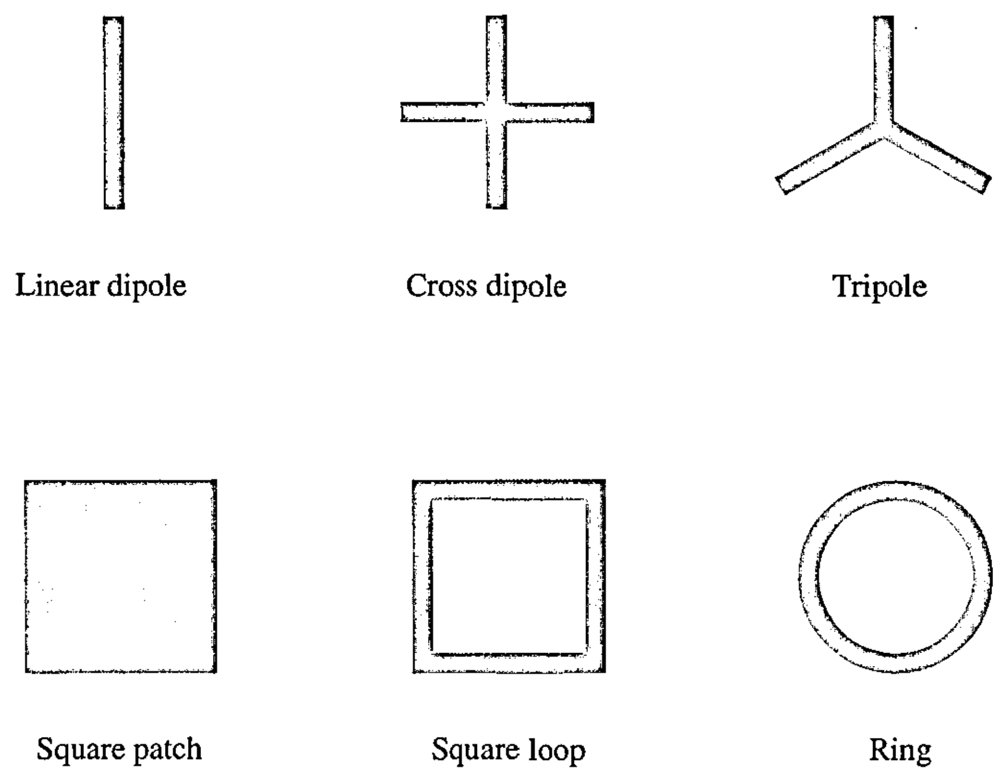

Figure 1.1 Some array element geometries

The elements may be arranged on several lattice geometries such as a simple rectangular or an off-axis triangular lattice with unequal sides. They can be either thin metallic patches supported on a dielectric substrate or apertures in a metallic screen. In the former case the array exhibits a capacitive behavior (Fig. 1.2). Its reflection magnitude increases with frequency and at resonance the FSS is totally reflective. The reflection phase decreases with frequency until it becomes $-\pi$ at resonance. The latter case produces an inductive effect and the reflection magnitude decreases with frequency until resonance, where the FSS is totally transparent. The reflection phase, in turn, also decreases with frequency until it takes a zero value at resonance. A typical frequency response of conducting as well as aperture element arrays is shown in Fig. 1.2.

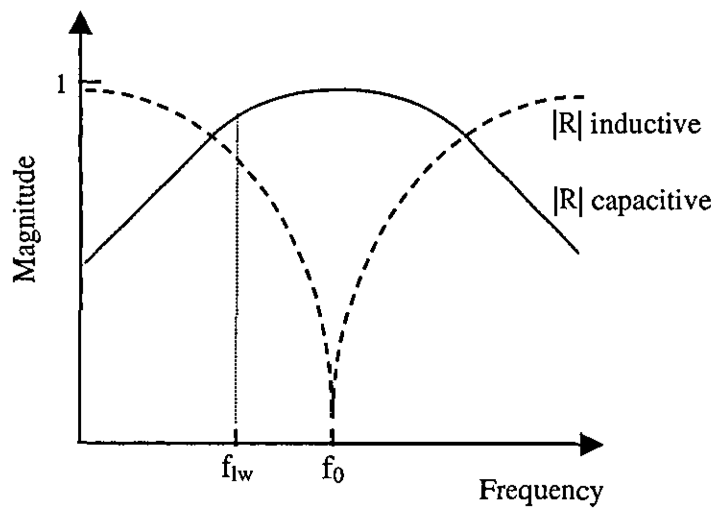

(a) Reflection coefficient magnitude

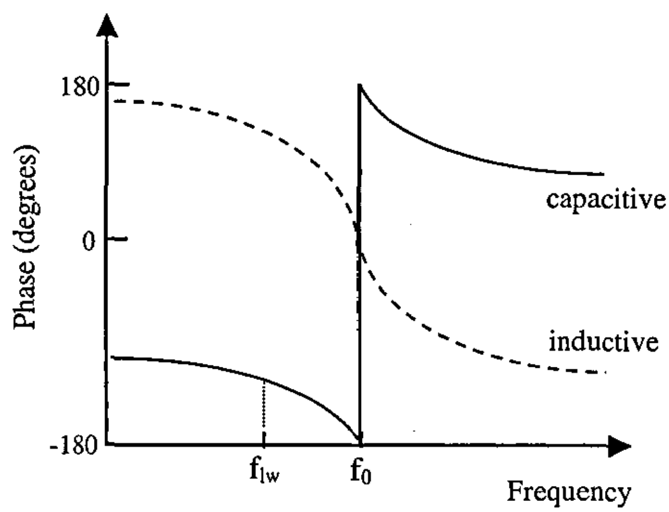

(b) Reflection coefficient phase

Figure 1.2 Typical frequency response of an array of conducting (capacitive) and aperture (inductive) elements

At frequencies near the resonance f_0, FSSs are partially reflective to a greater or lesser extend depending on their element geometry and periodicity. A certain amount of the incident radiation is transmitted through the screen, and the remaining (assuming no losses) is reflected. Throughout the rest of the thesis, the range of frequencies where this leakage occurs will be referred to as leaky-wave frequencies of the array (f_{lw}). When used in the leaky-wave frequency range the array behaves as a partially reflective surface (PRS). Due to this partial electromagnetic transparency at leaky-wave frequencies, PRSs exhibit a leaky-wave action when they are placed in parallel in front of a ground plane, as discussed in the previous section.

A further property of periodic arrays is that, in general, their reflection and transmission coefficients depend on the angle of incidence and in some cases vary rapidly with it. This effect prompts their use as spatial filtering arrays for beamforming in antenna systems [15]. In general, the variation of the transmission coefficient of a capacitive PRS with angle of incidence, assuming plane wane illumination at a fixed frequency and infinite size of the array, has the form shown in Fig. 1.3.

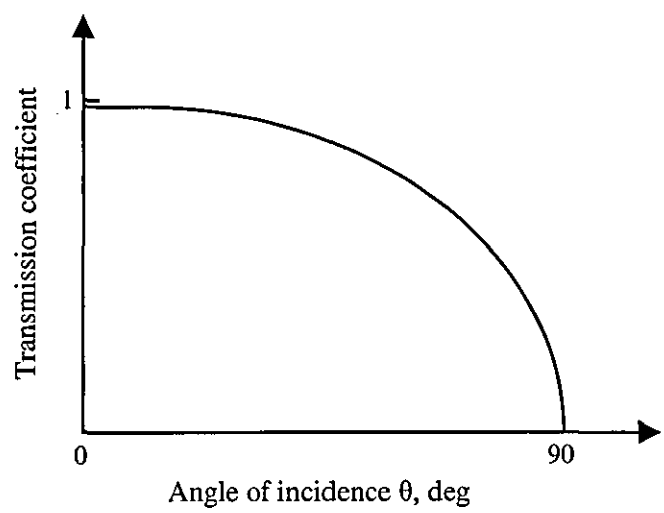

Figure 1.3 A typical response of a capacitive PRS with angle of incidence, θ.

1.3 Aim and Overview of the Thesis

The thesis begins with a review of the leaky-wave antenna configuration proposed in [8, 9]. Initially, this structure has been analysed using a simple ray theory approach based on multiple reflection between the partially reflective surface (PRS) and the ground plane. Both PRS and ground plane were assumed to be infinite. The reflection characteristics of the PRS were estimated using approximate formulas and at normal incidence [16]. Furthermore, the antenna bandwidth was quite narrow due to the resonant nature of the structure.

The research effort in this thesis focuses on the theory underpinning the beamforming effect of single and double-layer PRSs in a leaky-wave antenna configuration. A plane-wave modal analysis is implemented and used to compute the reflection response of single and double layer PRS arrays. A theoretical model of the antenna is produced based on geometrical optics in conjunction with the plane-wave modal analysis of the PRS. The model relates the antenna gain, bandwidth and radiation patterns to the reflection characteristics of the PRS. A new improved analysis of the leaky-wave antenna based on an angle-dependant modal analysis of the PRS is achieved [17, 18]. The effect of the phase and amplitude of the reflection coefficient of the PRS on the antenna performance is studied [19]. The study leads to the derivation of two analytical equations which describe the optimum PRS reflection response for a high-gain and wideband leaky-wave antenna performance. According to these equations it was discovered for the first time that a high PRS reflection magnitude constant with frequency and a reflection phase increasing linearly with frequency would result in a high-gain and wideband antenna performance.

Novel PRS designs for obtaining planar leaky-wave antennas with high gain and broad bandwidth are proposed and investigated. Single layer PRSs are optimised to a certain extent and used to produce high-gain antennas with improved bandwidth [19]. A novel double-layer PRS design is proposed, whereby the reflection phase increases with frequency, for further bandwidth enhancement of the antenna [20]. To the author's knowledge this is the first time that this characteristic reflection phase response is reported in the literature. This has paved the way for further improvements in the antenna performance by using an open cavity feed technique which increases the gain and improves the radiation patterns. Moreover, an investigation has been carried out on a multiple feed technique based on simulations. Simulation results have indicated a significant increase in gain whilst low sidelobe level was maintained.

The initial theoretical analysis used to model the leaky-wave antenna is approximate and doesn't take into account the finite size of the PRS and the ground plane. In addition to the theoretical analysis, full-wave simulation packages have been used to model the antenna. Initially, a 2.5D frequency domain package, Ensemble, has been used to simulate the edge effects due to the finite size of the PRS. Nevertheless, approximations had to be made for the waveguide aperture feed and the size of the ground plane. An FDTD simulation package, called LC, has been used for a full 3D simulation of the antenna, including the grounded waveguide feed. Although the code was parallelised (executed on an eight-processor Cray machine kindly provided by Advantica - formerly British gas) it was not fully developed and there were limitations in its modelling capabilities. Unfortunately, due to unforeseen circumstances, the access to the Cray computer stopped towards the last stages of the research. The effort was then switched to a 3D TLM based package, called Microstripes, that became available to the research group. This was a fully developed package for PC machines. It provided significant advantages in modelling, i.e. non-uniform meshing, symmetry conditions and automatic return loss calculation. All of these features resulted in a significant reduction of the computational size. In addition, its good visualisation options provided an insight into the fields and currents on the antenna.

The organisation of the thesis is as follows:

An introduction to the work carried out in the thesis is given in this chapter. Initially, a brief background on existing designs of high-gain antennas is given and the advantages and disadvantages are discussed. The concept of passive planar periodic arrays used as partially reflective surfaces (or leaky-wave arrays) is introduced and examples of different array geometries are given. The aim of the research is outlined and an overview of the work carried out is presented.

Chapter 2 covers the theoretical model and simulation methods used to analyse the antenna. The approximate analysis of the leaky-wave antenna based on geometrical optics is presented. The analysis is further developed to produce a better insight of the function of the antenna as well as valuable design guidelines for gain and bandwidth enhancement. The plane wave modal analysis that is used to simulate the reflection characteristics of the PRSs is described for both single and double layer arrays with dielectric support. Finally, a brief description of the software packages used to simulate the antenna is included at the end of the chapter.

In Chapter 3 the leaky-wave antenna with single-layer PRSs is studied. Initially, an improved angle-dependant analysis of the antenna is presented. Subsequently, the effect of the amplitude and phase of the reflection coefficient of the PRS on the antenna gain and bandwidth is investigated. A single-layer PRS is optimised for high gain and broad bandwidth and used to produce a leaky-wave antenna with improved characteristics. Ensemble has been used to model the edge effects due to the finite size PRS in the antenna and verify the optimisation procedure. The antenna has also been simulated using a 3D FDTD code, called LC. Finally, the effect of the size of the PRS on the antenna gain and efficiency has been studied.

Chapter 4 considers double layer PRS designs for further bandwidth enhancement of the leaky-wave antenna. A novel configuration of the double layer structure is presented, which results in a plane wave PRS response whereby the reflection phase increases with frequency in a certain frequency range. Double layer dipole and square patch PRS optimised designs are produced and used to form broadband high gain leaky-wave antennas. A waveguide-fed slot in the ground plane is used as feeding antenna in order to improve the matching. Microstripes has been used to calculate the return loss and design the waveguide-fed slot. The same package is used to produce simulation results of the antenna with the square patch PRS.

In Chapter 5 new feed strategies are investigated resulting in an improved antenna performance. An open cavity feed is designed after simulation in Microstripes for a better gain performance and lower sidelobe level. Simulations have also been carried out in order to investigate the performance of the antenna with a multiple slot-feed structure, for an improvement of the illumination of the PRS.

Finally, Chapter 6 draws conclusions from the work presented in the thesis and discusses the results. Further improvements of the leaky-wave antenna designs are considered and future developments are proposed.

References

[1] BALANIS, C. A. : 'Antenna Theory: Analysis and Design', John Wiley, New York, 1997

[2] ANDO, M., HIROKAWA, J., YAMAMOTO, T., AKIYAMA, A., KIMURA, Y. and GOTO, N. :'Novel single-layer waveguides for high-efficiency millimeter-wave arrays', *IEEE Trans. Microwave Theory Tech.*, vol. MTT-46, No. 6, June 1998, pp. 792-799

[3] JAMES, J.R., and HALL, P.S.: 'Handbook of microstrip antennas' (Peter Peregrinus Ltd., London, 1989)

[4] POZAR, D.M. and SCHAUBERT, D.H., Eds: 'Microstrip antennas' (New York: IEEE Press, 1995)

[5] JAMES, J. R. and HENDERSON, A. : 'Low-cost flat-plate array with squinted beam for DBS reception', *IEE Proc., Microw., Antennas & Propag.*, pt. H, vol. 134, Dec. 1987, pp. 509-514

[6] HALL, P. S. and HALL, C. M. : 'Coplanar corporate feed effects in microstrip patch arrays design', *IEE Proc., Microw., Antennas & Propag.*, pt. H, vol. 135, June 1988, pp. 180-186

[7] LEVINE, E., MALAMUD, G., SHTRIKMAN, S. and TREVES, D. : 'A study of microstrip array antennas with the feed network' *IEEE Trans. Antennas and Propagation,* vol. AP-37, No. 4, April. 1989, pp. 426-434

[8] TRENTINI, G. V.: 'Partially reflecting sheet arrays', *IRE Trans. Antennas Propag.*, 1956, **AP-4**, pp. 666-671

[9] JAMES, J. R., KINANY, S.J.A., PEEL, P.D., and ANDRASIC, G.: 'Leaky-wave multiple dichroic beamformers," *Electron. Lett.,* 1989, **25**, pp. 1209-1211

[10] JAMES, J.R., and ANDRASIC, G.: 'Superimposed dichroic microstrip antenna arrays', *IEE Proc. H, Microw., Antenna & Propag.*, 1988, **135**, (5), pp. 304-312

[11] ROBINSON, A.J, VARDAXOGLOU, J.C., and SEAGER, R.D.: 'Wave guidance and radiation from a hollow tube formed from frequency-selective surfaces', *Electron. Lett.*, 1993, **29**, pp. 1531-1533

[12] VARDAXOGLOU, J.C., ROBINSON, A.J. and SEAGER, R.D.: 'Towards a new class of waveguiding structures and lightweight horn antennas using passive arrays', Proc. IEEE International Conference on Electromagnetics in Aerospace Applications, ICEAA, Sept. 1993, Torino, Italy, pp.343-346

[13] VARDAXOGLOU, J. C.: 'Frequency Selective Surfaces: Analysis and Design' (Research Studies Press, Somerset, England, 1997)

[14] MITTRA R., CHAN C. H., and CWIK T., 'Techniques for analyzing frequency selective surfaces – A review' *Proc. IEEE,* vol. 76, No. 12, Dec. 1988, pp. 1593-1615

[15] CHADRAN S. and VARDAXOGLOU J. C. : 'Performance of two single-layer frequency-selective surfaces as spatial filters', *Microwave Opt. Technol. Lett.,* vol. 6, May 1993, pp. 339-342

[16] LEE S. W., ZARRILLO G., and LAW C. K. : 'Simple formulas for transmission through periodic metal grids or plates', *IEEE Trans. Antennas Propagat.,* vol. AP-30, 1982, pp. 904-909

[17] COX, G.J., FERESIDIS, A. and VARDAXOGLOU, J.C. : 'Leaky Wave Action of Planar and Cylindrical FSS', Proc. PREP 2000, 2nd Conference on Postgraduate

Research in Electronics, Photonics and Related Fields, IEE, University of Nottingham, April 2000, pp. 273-278

[18] FERESIDIS, A. and VARDAXOGLOU, J.C.: 'Flat plate millimetre wave antenna based on partially reflective FSS', Proc. 11th International Conference on Antennas and Propag., ICAP, April 2001, Manchester, UK, pp. 33-36

[19] FERESIDIS, A. P. and VARDAXOGLOU, J. C. : 'High gain planar antenna using optimised partially reflective surfaces', *IEE Proc., Microw., Antennas & Propag.*, vol. 148, No. 6, Dec. 2001, pp. 345-350

[20] FERESIDIS, A. P. and VARDAXOGLOU, J. C. : 'Double layer partially reflective surfaces for high gain planar antennas', Proc. IEEE International Conference on Electromagnetics in Advanced Applications (ICEAA), Torino, Italy, September 2001, pp. 243-246

Chapter 2

Theory and Simulation Methods

2.1 Introduction

This chapter covers the theoretical model used in the antenna design as well as the numerical methods used for a rigorous simulation of the antenna. A ray theory analysis is employed to describe the leaky-wave and beamforming effect of the PRSs and subsequently to produce useful design guidelines. These are guidelines for high-gain and broadband antenna performance and they will be the objectives upon which the design and optimisation of the PRSs will be based. The ray analysis relates the antenna performance to the reflection characteristics of the PRS array. A modal analysis is used to compute the reflection/transmission coefficient of large ($\approx 10\lambda$) periodic arrays under plane-wave illumination. The analysis is based on the Floquet theorem and it is presented for single and double layer arrays of conducting patches printed on dielectric substrates. The ray analysis in conjunction with the modal calculation of the reflection response of the PRS array provides an approximate theoretical model of the antenna with large PRSs.

In addition to the theoretical model, three full wave simulation packages have been used for more rigorous simulations of the antenna with small size PRSs. Initially, Ensemble has been used to simulate the edge effects due to the finite size of the PRS. Time domain codes have also been used for a 3D simulation of the antenna. A 3D FDTD based code, LC, has provided simulation results of the antenna in its entirety. However, the code was not fully developed and there were limitations in the structures that could be modeled. Non-uniform meshing and symmetry conditions (electric and magnetic walls) were not available, which increased the computer memory requirements. A fully developed and more robust simulation package, Microstripes, was used in the last stages of the research and proved to be a valuable design tool. A brief introduction to all three simulation packages is given and the advantages and disadvantages are discussed.

2.2 Leaky-Wave and Beam-Forming Action of PRS

A geometrical optics (also called ray optics) approach can be used to describe mathematically the leaky wave action of a PRS placed in front of a ground plane. A ray optics approach was first presented by Trentini in [1], where he demonstrated how several types of partially reflective array sheets can considerably increase the directivity of a grounded waveguide aperture. Geometrical optics (GO) is an approximate high frequency method, which describes the paths of transmitted and reflected rays [2, 3]. The ray paths are perpendicular to the wavefronts and are in the direction of the Poynting vector at each point. The GO approximation is used when the wavelength is several times smaller than the dimensions of the radiating or scattering structure. This results in two things: diffraction effects are not dominant in the final response and there are no higher order coupling effects.

In the geometry studied here, a PRS is positioned in parallel at a distance L_r in front of a ground plane (Fig. 2,1). The PRS considered throughout the thesis is a single or double layer planar periodic array of conducting elements printed on dielectric substrate. The PRS is assumed to be of infinite size and the distance L_r is in the order of a wavelength, thus allowing for a GO approximation. An aperture within the ground plane (waveguide aperture or slot) is used as the primary antenna. The frequency of operation of the antenna is in the range of leaky-wave frequencies of the PRS (see section 1.2), so that an amount of the incident wave is transmitted through it and the remaining is reflected back towards the ground plane. The leaky-wave function of the antenna can be described as follows. Waves emerging from the primary antenna travel long paths as a result of multiple reflections between the ground plane and the PRS. A phase shift is introduced by the path length, the total reflection on the ground plane and also by the phase of the reflection coefficient of the PRS. The transmitted power can be calculated by the interference of the waves partially transmitted through the PRS. This leaky-wave effect is illustrated in Fig. 2.1.

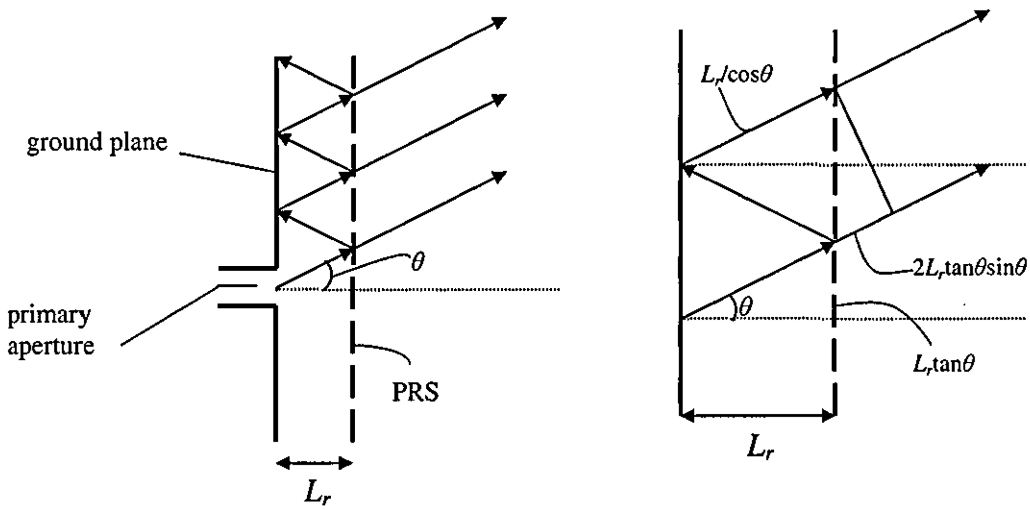

Figure 2.1 Geometry of the antenna and leaky-wave effect.

The mathematical description of the leaky-wave effect can be derived using the GO approach. A ray is emitted at an angle θ from a centre point of the primary antenna, which has a radiation pattern $F(\theta)$. The angle θ coincides with the angle of incidence θ^i of the PRS array co-ordinate system (see Fig. 2.6). The complex reflection coefficient of the PRS is $R(\theta)e^{j\phi(\theta)}$, where $R(\theta)$ the magnitude and $\varphi(\theta)$ the phase and it is a function of θ and of the array geometry for a fixed frequency of illumination.

If R_p is the power reflection coefficient of the PRS screen, the radiated power density S_0 of the primary transmitted ray 0 is proportional to $(1-R_p)$ and assuming no transmission losses the energy conservation law can be written:

$$S_0(\theta) = S_i(\theta)(1 - R_p(\theta)) \tag{2.1}$$

where S_i is the incident power density.

In terms of the amplitudes of the electric field and since $S \propto E^2$, we have:

$$E_0(\theta) = E_i(\theta)\sqrt{1 - R(\theta)^2} \tag{2.2}$$

where E_i is the incident field amplitude.

In the same manner, the field amplitudes of the transmitted rays 1 and 2, which have been reflected by the PRS once and twice respectively, are :

$$E_1(\theta) = E_i(\theta)R(\theta)\sqrt{1 - R(\theta)^2} \quad \text{and} \quad E_2(\theta) = E_i(\theta)R^2(\theta)\sqrt{1 - R(\theta)^2} \tag{2.3}$$

Thus, for the n^{th} transmitted ray,

$$E_n(\theta) = E_i(\theta)R^n(\theta)\sqrt{1 - R(\theta)^2} \tag{2.4}$$

The electric field in the far-field region consists of the vector sum of all n rays, and for an infinite screen and ground plane we can write:

$$E(\theta) = \sum_{n=0}^{\infty} F(\theta)E_i(\theta)R^n(\theta)\sqrt{1 - R(\theta)^2}\, e^{j\Theta_n(\theta)} \tag{2.5}$$

The phase angle Θ_n is the total phase change of the n-times reflected ray from both the PRS and the ground plane. The phase difference between two successive transmitting rays is formed by the phase shifts due to a partial reflection from the PRS ($\phi(\theta)$), a complete reflection from the conductive screen (π), and the optical path difference $(l_1 - l_2)$ of the rays [4]. The phase shift due to the partial transmission from the PRS is the same for both rays and it is not taken into account. From the geometry in Fig. 2.1:

$$(l_1 - l_2) = 2L(\tan\theta \sin\theta - \frac{1}{\cos\theta}) = -2L\cos\theta \tag{2.6}$$

and the phase change is given by:

$$\Phi(\theta) = \frac{2\pi}{\lambda}(l_1 - l_2) - \pi + \phi(\theta) \ , \tag{2.7}$$

where λ is the wavelength.

Thus,

$$\Theta_n(\theta) = n\Phi(\theta) = n\left[-\frac{4\pi}{\lambda}L\cos\theta - \pi + \phi(\theta)\right] \tag{2.8}$$

Equation (2.5) is now written

$$E(\theta) = F(\theta)E_i(\theta)\sqrt{1 - R(\theta)^2}\sum_{n=0}^{\infty}\left[R(\theta)e^{j\Phi(\theta)}\right]^n \tag{2.9}$$

and since $0 < R(\theta) < 1$, we have [5]:

$$\sum_{n=0}^{\infty}\left[R(\theta)e^{j\Phi}\right]^n = \frac{1}{1 - R(\theta)e^{j\Phi}} \tag{2.10}$$

Substituting Eqn. (2.10) into Eqn. (2.9) and taking the absolute value yields

$$|E(\theta)| = |E_i(\theta)| F(\theta) \sqrt{\frac{1 - R^2(\theta)}{1 + R^2(\theta) - 2R(\theta)\cos\Phi(\theta)}} \tag{2.11}$$

Therefore, the power pattern is:

$$P(\theta) = \frac{\left[1 - R^2(\theta)\right]}{1 + R^2(\theta) - 2R(\theta)\cos\left[\phi(\theta) - \pi - \frac{4\pi L_r}{\lambda}\right]} F^2(\theta). \tag{2.12}$$

Following Eqn. (2.12) we have maximum power at boresight ($\theta = 0°$), when the following phase condition is satisfied:

$$\phi(0) - \pi - \frac{4\pi L_r}{\lambda} = 2N\pi, \qquad \text{where } N = 0, 1, 2, \ldots$$

Hence, the equation determining the physical distance between the PRS and the ground plane is:

$$L_r = \left(\frac{\phi(0)}{\pi} - 1\right)\frac{\lambda}{4} + N\frac{\lambda}{2}, \qquad \text{where } N = 1, 2, 3 \ldots \tag{2.13}$$

It should be noted that in the case of a capacitive screen (e.g. array of conducting elements) the reflection coefficient phase should be expressed in positive values, i.e. $\pi < \phi(0) < 2\pi$. The value $N = 0$ is rejected for $\phi(0) < \pi$, because it gives negative values of L_r, which has no physical meaning. For $\pi < \phi(0) < 2\pi$, it gives small values of resonant distance, and in particular for highly reflective screens with phase close to π, the distances become impractical. Therefore $N = 0$ is omitted in Eqn. (2.13).

The antenna structure is essentially a resonant cavity, formed by one totally and one partially reflective mirror. L_r is the physical distance where the cavity resonates for a certain frequency, and is called the resonant distance. As we can see from Eqn. (2.13), the resonant distance depends only on $\phi(0)$ and the operating frequency. The principle of the analysis presented above is similar to the resonant optical cavity theory [6], which also follows a ray tracing approach to describe the optical ray trips between two highly reflective mirrors. In an optical instrument such as the Fabry-Perot interferometer, partially metallised mirrors are used with their reflection phase response close to π and independent of frequency. In contrast, the reflection/transmission response (magnitude and phase) of the arrays used in this study is dependant on frequency and this has been taken into account in the analysis. The optical resonant cavity approach has also been used in recent years to describe the response of double layer FSS, [7].

The approximate formula (2.12) can be used to calculate the radiation pattern of the leaky-wave antenna when the complex reflection coefficient of the PRS and the radiation pattern of the primary antenna (e.g. waveguide aperture) are known. The complex reflection coefficient of various PRSs are calculated using the plane-wave Floquet modal analysis combined with a method of moments solution of the integral equations, as described in section 2.4. The radiation pattern $F(\theta)$ of a grounded waveguide aperture used as the primary antenna can be calculated by approximate analytical expressions. Assuming an infinite ground plane and TE_{10} mode field distribution in the waveguide, the H and E-plane radiation patterns are given by [3]:

$$F_H(\theta) = \cos\theta \frac{\cos\left(\frac{ka}{2}\sin\theta\right)}{1-\left(\frac{2}{\pi}\frac{ka}{2}\sin\theta\right)^2} \qquad \text{(H-plane)} \qquad (2.14)$$

$$F_E(\theta) = \frac{\sin\left(\frac{kb}{2}\sin\theta\right)}{\frac{kb}{2}\sin\theta} \qquad \text{(E-plane)} \qquad (2.15)$$

where $-\frac{\pi}{2} \leq \theta \leq \frac{\pi}{2}$.

The approximations made in the modelling of the antenna are:

- The wavelength is assumed to be considerably smaller than the dimensions of the antenna (GO approximation), although the resonant distance is in the magnitude scale of a wavelength.

- The array and the ground plane are assumed to be of infinite extent so that there are no escaping rays. Therefore, diffraction effects, which would appear at the edges of a finite size PRS and ground plane, are not taken into account.

- The amplitude of the incident on the PRS field decreases as we move away from the primary antenna due to continuous leakage. This means that the coupling fields are non uniform across the antenna's surface. However, in the calculation of $R(\theta)e^{j\phi(\theta)}$, as it is discussed later, we assume a uniform illumination of the PRS.

2.3 High Gain and Wide Bandwidth Requirements

The analysis presented in section 2.2 can produce some further valuable conclusions with regard to the antenna gain and bandwidth [8]. Rearranging Eqn. (2.12) we have an expression of the directivity or gain - since losses are not taken into account - relative to the primary antenna. The following equation gives the relative gain at boresight ($\theta = 0°$):

$$G = \frac{P}{F^2} = \frac{\left(1-R^2\right)}{1+R^2-2R\cos\left(\phi-\pi-\frac{4\pi f L_r}{c}\right)} \qquad (2.16)$$

The values of reflection coefficient magnitude and phase in Eqn. (2.16) correspond to normal incidence on the PRS and are dependent on frequency. Inserting Eqn. (2.13), which gives the resonance phase condition, into Eqn. (2.12), yields an expression for the maximum relative gain:

$$G = \frac{P}{F} = \frac{1+R}{1-R} \tag{2.17}$$

The maximum relative gain is expressed as a function of only one variable: the reflection coefficient magnitude of the PRS under normal incidence. It increases considerably with *R*, as we can see from Eqn. (2.17), and very high gain can be obtained with a highly reflective screen. This is illustrated in Fig. 2.2.

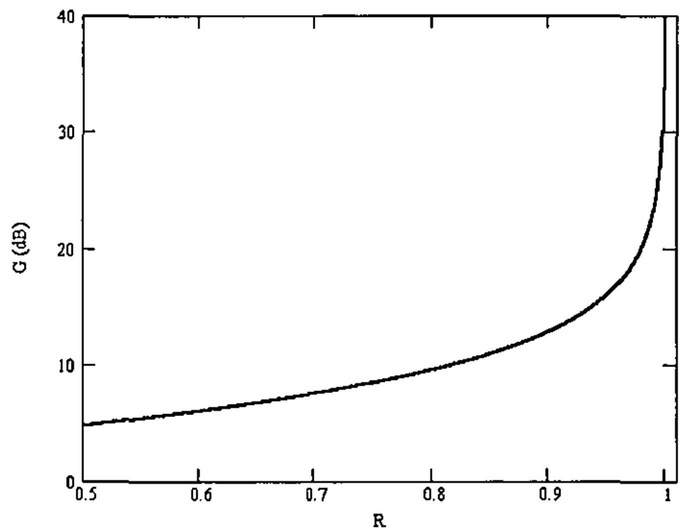

Figure 2.2 Maximum relative gain as a function of the PRS reflection coefficient

If we assume that the PRS is highly reflective, with $\phi(f) \approx \pi$, then

$\Phi = \phi - \pi - \dfrac{2 \cdot 2\pi f L_r}{c} = 2kL_r$, where $k = \dfrac{2\pi f}{c}$ is the wave vector magnitude

and $\dfrac{\Phi}{2} = kL_r$, which is the electrical length of the cavity.

Since $\cos 2\theta = 1 - 2\sin^2\theta$ ([5]), Eqn. (2.16) is written:

$$G = \frac{\left(1 - R^2\right)}{(1-R)^2 + 4R\sin^2\left(\frac{\Phi}{2}\right)} \tag{2.18}$$

It is quite instructive to plot the relative gain of the antenna formed with a highly reflective screen, which is given by Eqn. (2.18), as a function of the electrical length $\Phi/2$, Fig. 2.3.

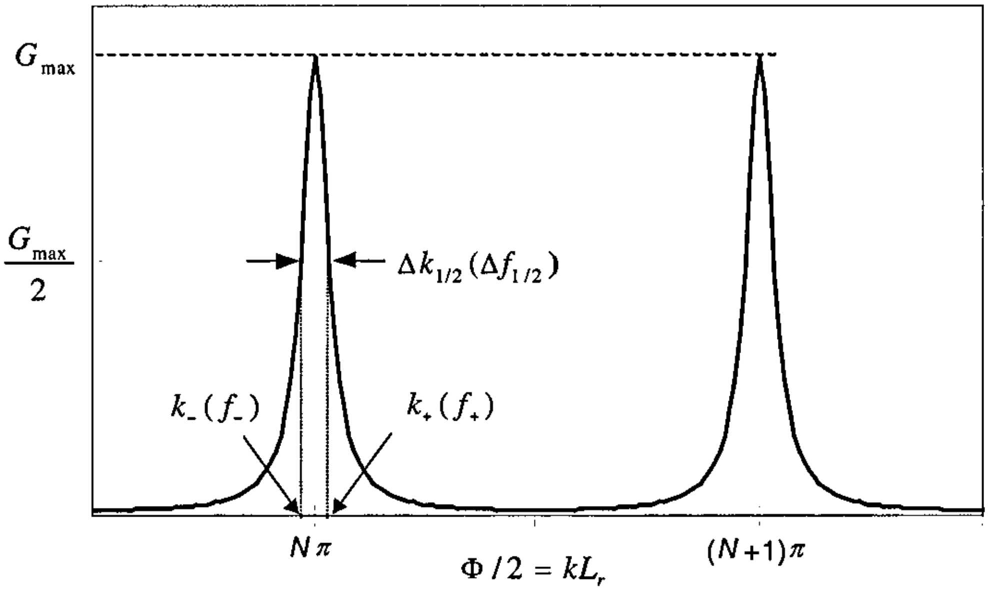

Figure 2.3 Gain characteristics of resonant leaky-wave cavity

The gain peaks at resonance $N\pi$, as expected, with a maximum value given by Eqn. (2.17). For highly reflective screens, the resonant peak may reach a very high value, but it also becomes very sharp. Thus, the bandwidth decreases dramatically. A measure of the sharpness of the cavity resonance is the Q (for quality factor) [6]:

$$Q = \frac{f_0}{\Delta f_{1/2}} \tag{2.19}$$

where $\Delta f_{1/2}$ is the full width at half maximum, i.e. the bandwidth and f_0 is the resonant frequency. The inverse of Q is the fractional bandwidth (BW), which is a measure of the frequency range where the antenna gain is appreciable:

$$BW = \frac{\Delta f_{1/2}}{f_0} \tag{2.20}$$

The frequencies, f_+ and f_-, where the gain decreases to one half of the maximum value, can be calculated using Eqn. (2.18). For a highly reflective screen, the electrical angle will deviate only slightly from $N\pi$ and one can use the small-angle approximation for $\sin(N\pi + \Delta\Phi) \approx \Delta\Phi$.

$$G_{f\pm} = \frac{G_{\max}}{2}$$

or $$\frac{\left(1-R^2\right)}{(1-R)^2 + 4R\sin^2\left(\frac{2\pi f_\pm}{c} L_r\right)} = \frac{1}{2}\frac{1+R}{1-R}$$

or $$\sin\left(\frac{2\pi f_\pm}{c} L_r\right) = \pm\frac{1-R}{2\sqrt{R}}$$

or $$f_\pm = N\frac{c}{2L_r} \pm \frac{c}{2L_r}\frac{1-R}{2\pi\sqrt{R}}$$

Therefore

$$\Delta f_{1/2} = f_+ - f_- = \frac{c}{2L_r}\frac{1-R}{\pi\sqrt{R}}$$

Thus, the fractional bandwidth is given by

$$BW = \frac{\Delta f_{1/2}}{f_0} = \frac{c}{2\pi f_0 L_r} \frac{1-R}{\sqrt{R}} \tag{2.21}$$

In Eqn. (2.21) the bandwidth is expressed as a function of the reflection coefficient magnitude and the resonant distance. The first valuable information obtained from Eqn. (2.21) is that narrower bandwidth is expected for resonant distances beyond the first one, i.e. $N>1$ in Eqn. (2.13). Thus, for the highest available bandwidth N should be equal to 1 and this will be the case for the rest of the thesis. The dependence of BW with R is also obtained from Eqn. (2.21) and it is plotted in Fig. 2.4.

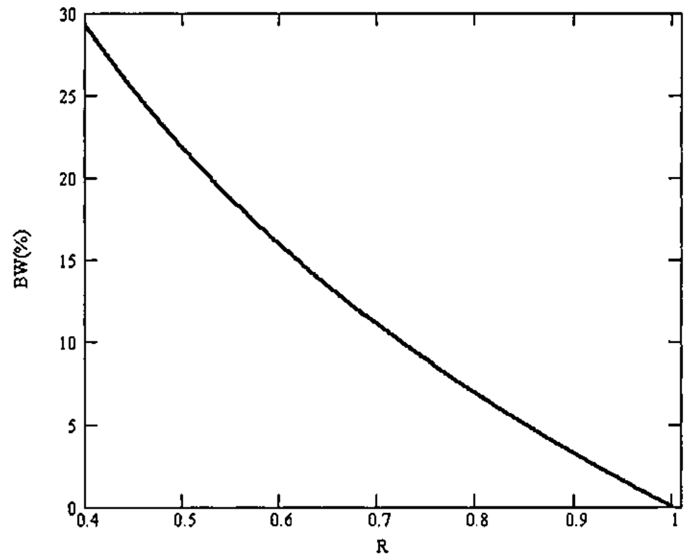

Figure 2.4 Fractional bandwidth as a function of the reflection magnitude of the PRS

Highly reflective PRS screens, which are needed for high gain, decrease the antenna bandwidth dramatically. This is a result of the resonant nature of the leaky-wave antenna configuration. However, there is a way to increase the bandwidth even further than the values presented in Fig. 2.4.

It is useful to remind here that the results presented above are based on the assumption of constant magnitude and phase values of the reflection coefficient with frequency. *For a wide-band response, the reflection magnitude should ideally be constant, so that, according to Eqn. (2.17), the maximum gain would not vary with frequency.* However, it is the phase condition, Eqn. (2.13), that determines the frequencies where this maximum gain occurs, hence the operating frequency band of the antenna. Rearranging the terms, the phase condition can be written:

$$\phi = \frac{4\pi L_r}{c} f - (2N-1)\pi \tag{2.22}$$

Equation (2.22) provides a somewhat different representation of the phase condition and it is used to obtain a theoretical requirement for wide-band performance. Consider the physical distance L_r to be constant and equal to the first resonance distance corresponding to a resonant frequency f_0. In order to achieve maximum gain in a wide range of frequencies around f_0, e.g. f_1 to f_2, ϕ should satisfy Eqn. (2.22) for all the frequencies in $[f_1, f_2]$. Therefore, *the reflection phase should increase linearly with frequency, with a gradient of* $4\pi L_r / c$. *This is the optimum PRS phase response for wide bandwidth.*

To illustrate the effect of the phase variation (with frequency) to the antenna bandwidth, a graph of the gain against frequency, for two fictitious PRSs with different phase responses, is plotted in Fig. 2.5. The reflection magnitude is assumed constant, ($R = 0.9$), for both PRSs. The reflection phase of the first PRS is assumed constant, whereas the reflection phase of the second is equal to the optimum in the frequency range between f_1 and f_2.

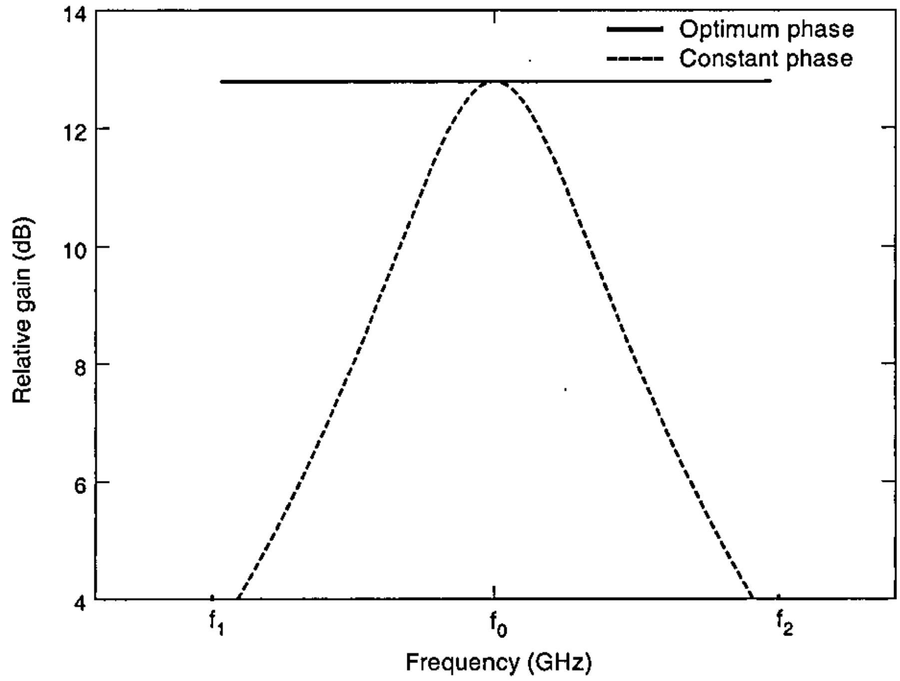

Figure 2.5 Gain of leaky-wave antenna with frequency, for optimum and constant reflection phase response of the PRS (for constant reflection magnitude)

It is apparent from Fig. 2.5 that the optimum phase along with a constant reflection magnitude provides a flat plateau of wide-band response. Of course, in practise it is difficult to find such reflection responses, as it will be discussed in Chapters 3 and 4. A large part of this thesis is focused on novel designs of single and double layer PRSs with reflection characteristics close to the optimum.

2.4 Analysis of Planar Periodic Arrays

A full wave modal analysis of single and double layer planar periodic arrays of conducting elements on dielectric substrates excited under plane wave illumination is presented here. The analysis is based on [9, 10] and is used to compute the reflection/transmission coefficients of large periodic arrays as a function of frequency as well as angle of incidence on the array. It provides the values of reflection coefficient of the PRS array, which are required in the approximate theoretical model of the leaky-wave antenna.

The electromagnetic scattering problem from arrays of relatively large size ($\approx 10\lambda$) is simplified by the assumption that they are infinite in extent. A spectral domain approach based on Floquet's theorem, [11], reduces the analysis from one that considers the entire surface to one that only considers a single periodic cell.

Floquet's theorem is an extension of the Fourier series theorem for periodic functions. The extension permits a modal description of any field or function, which repeats itself periodically except for a progressive exponential multiplier. Such a periodic function is an appropriate description for the field in the vicinity of an infinite planar periodic array under plane wave illumination [11]. Therefore, the scattered fields as well as the induced currents can be expressed as a Fourier series with periodicity equal to that of the unit cell.

An integral equation for the unknown currents induced on the array unit element is formed by matching the fields at different boundaries. In the case of double layer array structures, the currents on each array are linked together by the formation of two coupled integral equations (CIEs), which contain terms for the currents on both arrays. The method of moments (MoM) is then used to reduce the integral equations into a system of linear equations, whereby the currents are represented by a set of basis functions. Using an appropriate numerical technique, these equations can be solved for the unknown currents, which in turn are used to calculate the reflected and transmitted fields, and hence, the reflection and transmission coefficients.

2.4.1 Wave analysis

Fig. 2.6 shows the coordinate system used in the analysis as well as a small section of the infinite array (arbitrary elements) arranged in a rectangular lattice. The cross section of the array supported on a dielectric substrate has also been sketched. A plane wave with wave vector $\underline{k}^i$ is incident in an arbitrary direction defined by the angles θ^i and ϕ^i. The incident field is linearly polarised along the y-axis. The lattice vectors D_x, D_y specify the two periodicity axes. We assume time harmonic fields with an $e^{j\omega t}$ dependence which will be implicit throughout the rest of the analysis.

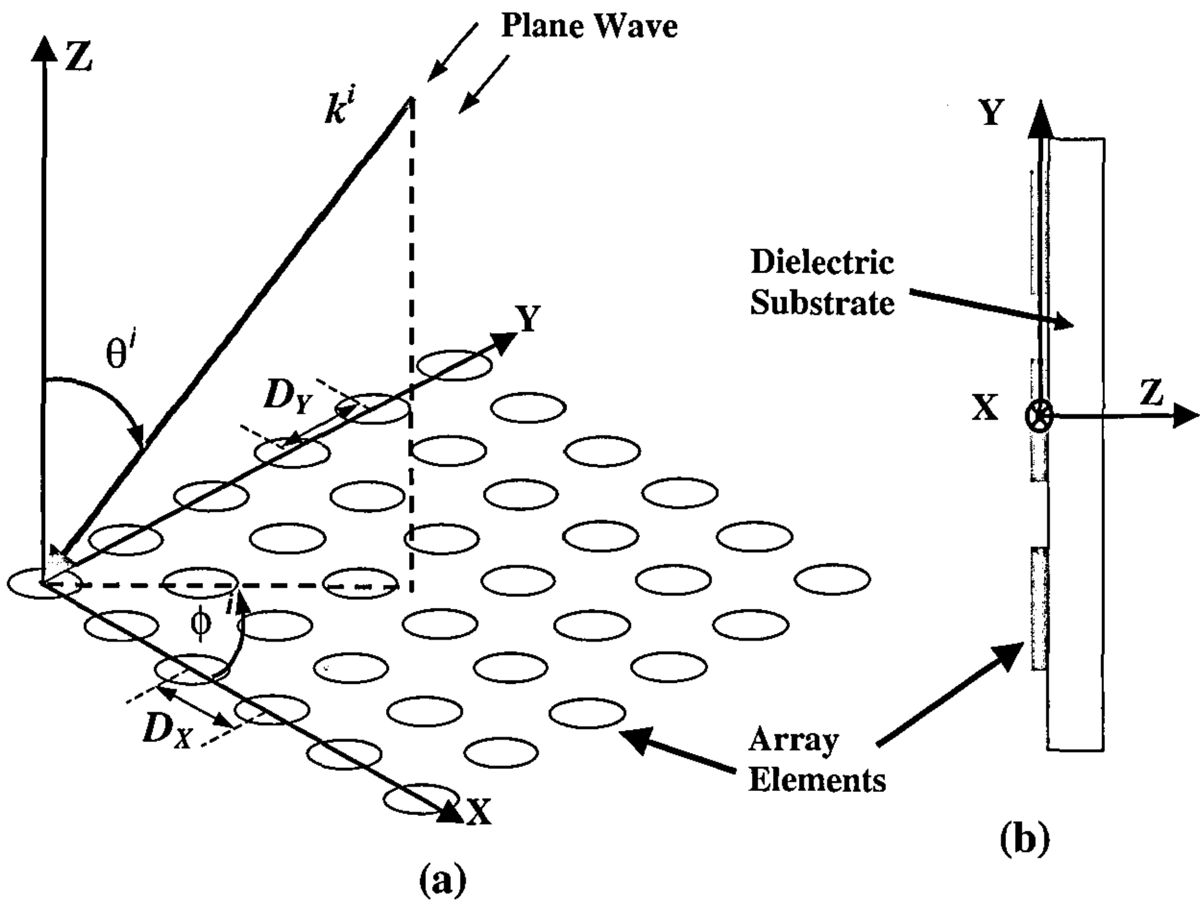

Figure 2.6 (a) Planar array on rectangular lattice and coordinate system (b) Cross section of the array supported on a dielectric substrate

To allow for a more general analysis, an arbitrary lattice geometry is considered. A typical array geometry on an arbitrary lattice is depicted in Fig. 2.7. The lattice vectors $\underline{D}_u$, $\underline{D}_v$ specify the two periodicity axes u and v, along which the arbitrary elements of the array are arranged. In the rectangular coordinate system they are written:

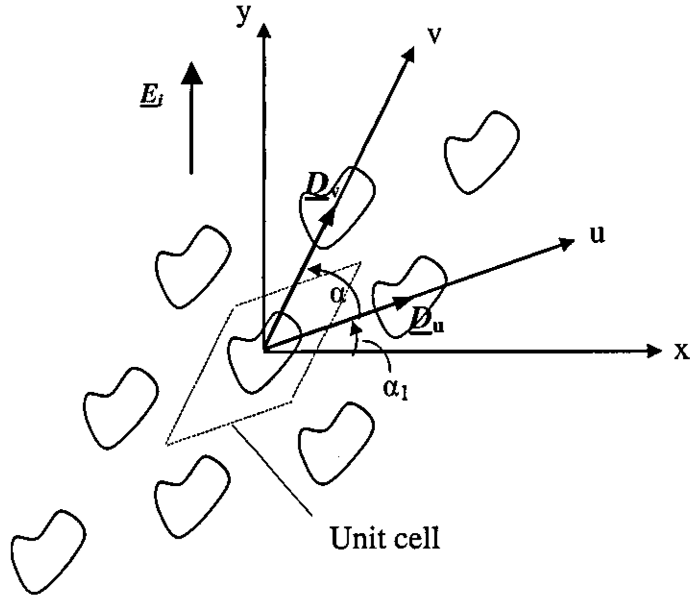

Figure 2.7 Geometry of planar array on an arbitrary lattice

$$\underline{D}_u = D_u(\cos\alpha_1\hat{x} + \sin\alpha_1\hat{y})$$

$$\underline{D}_v = D_v(\cos\alpha_2\hat{x} + \sin\alpha_2\hat{y}) \tag{2.23}$$

where $\alpha_2 = \alpha + \alpha_1$ and $D_u = |\underline{D}_u|$, $D_v = |\underline{D}_v|$

The scalar Floquet modes for an arbitrary lattice are given by:

$$\Xi_{pq}(x, y, z) = \Psi_{pq}(x, y)e^{-j\beta_{pq}z} = e^{-j\underline{k}_{tpq}\cdot\underline{r}}e^{\pm j\beta_{pq}z} \tag{2.24}$$

where the positive (negative) sign denotes fields propagating in the negative (positive) direction, and

$$p, q = 0, \pm 1, \pm 2, \ldots$$

$$\begin{aligned} \underline{k}_{tpq} &= \underline{k}_{t00} + p\underline{k}_1 + q\underline{k}_2 \\ &= k_x \hat{x} + k_y \hat{y} \end{aligned} \qquad (2.25)$$

$$\begin{aligned} \underline{k}_{t00} &= k \sin\theta^i \cos\varphi^i \hat{x} + k \sin\theta^i \sin\varphi^i \hat{y} \\ &= k_{00x}\hat{x} + k_{00y}\hat{y} \end{aligned}$$

$$\underline{k}_1 = -\frac{2\pi}{A}\hat{z}\times\underline{D}_v , \qquad \underline{k}_2 = \frac{2\pi}{A}\hat{z}\times\underline{D}_u$$

$$k = k_0\sqrt{\varepsilon_r} , \qquad k_0 = \frac{2\pi}{\lambda_0}$$

ε_r, the relative permittivity of the dielectric

$$\underline{r} = x\hat{x} + y\hat{y}$$

$A = \left|\underline{D}_u \times \underline{D}_v\right| = D_u D_v \sin\alpha$, the unit cell area.

The propagation constant is given by:

$$\begin{aligned} \beta_{pq} &= \sqrt{k^2 - (k_x^2 + k_y^2)} \\ &= (k^2 - \underline{k}_{tpq} \cdot \underline{k}_{tpq})^{1/2} \end{aligned} \qquad (2.26)$$

For propagating waves $k^2 \geq k_x^2 + k_y^2$ and β_{pq} is real and positive.

For evanescent waves $k^2 < k_x^2 + k_y^2$ and β_{pq} is imaginary and negative.

Propagating waves with Floquet indices $p, q \neq 0$ are referred to as grating responses and are generally undesirable, due to the distortion of the radiation pattern of the array (i.e. grating lobes).

An orthogonal complete set of vector Floquet modes, Eqn. (2.27), can be derived from Eqn. (2.24). These are TM (transverse magnetic) modes where the entire magnetic vector mode is parallel to the plane of the array and TE (transverse electric) modes where the entire electric vector is parallel to the array [9].

$$\underline{\Xi}_{mpq} = \Xi_{pq}\underline{K}_{mpq} = e^{\pm j\beta_{pq}z}\Psi_{pq}(\underline{r})\underline{K}_{mpq} \tag{2.27}$$

where

$m = 1$ for TM modes, 2 for TE modes

$\underline{K}_{1pq} = \dfrac{\underline{k}_{tpq}}{\left|\underline{k}_{tpq}\right|}$, the TM modes unit vector

$\underline{K}_{2pq} = \hat{z} \times \underline{K}_{1pq}$, the TE modes unit vector

The tangential to the array EM field may now be expressed as a linear combination of TM and TE vector Floquet modes.

$$\underline{E}(\underline{r}, z) = \sum_{mpq} a_{mpq} e^{\pm j\beta_{pq}z}\Psi_{pq}(\underline{r})\underline{K}_{mpq} \tag{2.28}$$

$$\underline{H}(\underline{r}, z) = \mp\sum_{mpq} \eta_{mpq} a_{mpq} e^{\pm j\beta_{pq}z}\Psi_{pq}(\underline{r})\hat{z} \times \underline{K}_{mpq} \tag{2.29}$$

where

η_{pq} is the modal admittance,

which for TM modes is $\eta_{1pq} = \dfrac{k}{\beta_{pq}}\eta$

and for TE modes $\quad \eta_{2pq} = \dfrac{\beta_{pq}}{k}\eta$,

with $\eta = \sqrt{\dfrac{\varepsilon}{\mu}}$, and ε, μ are the permittivity and permeability respectively of the relevant medium.

2.4.2 Single layer array

The scattering from an array of conducting elements printed on a dielectric substrate is studied in this section. Using the formulation presented in section 2.4.1 and applying the standard electromagnetic boundary conditions at different interfaces an electric field integral equation (EFIE) can be derived, where the unknown is the current induced on the conductors. In the derivation of the EFIE some intermediate steps are omitted, since the analysis has been covered elsewhere [9, 10].

The cross sectional view of an array supported on a single layer of dielectric material is shown in Fig. 2.8. The thickness of the array elements is considered zero but it is sketched oversized for better visualisation. There can also be more complicated structures, such as an array sandwiched between several dielectric layers. A general analysis that includes this kind of structure can be found in [9]. In this thesis only one dielectric layer has been used to support the various arrays under investigation, thus the analysis presented is limited to the structure shown in Fig. 2.8.

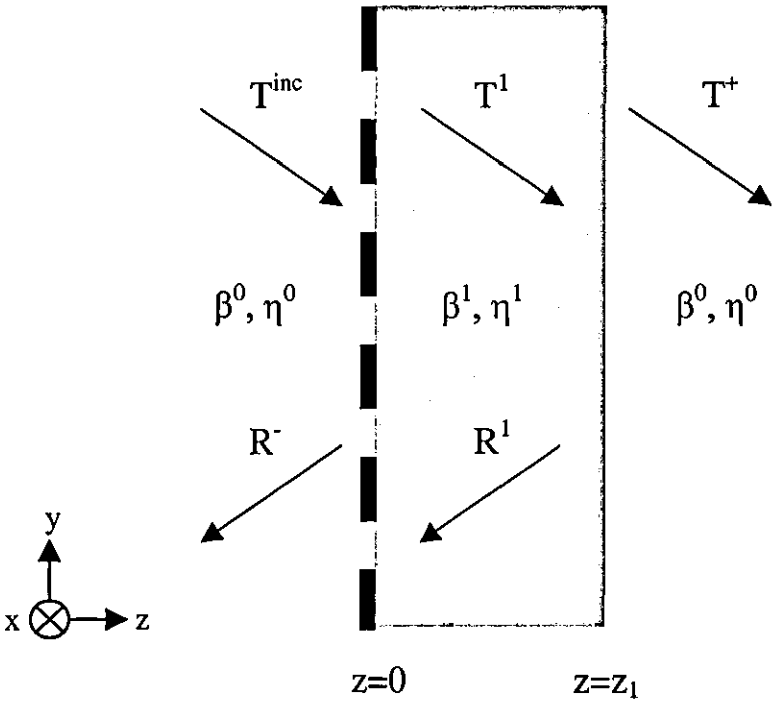

Figure 2.8 Cross section of array on dielectric substrate

The tangential field expansion for the different media are as follows:

For $z \leq 0$

$$\underline{E}^{-}(\underline{r}, z) = \underline{E}^{inc} + \sum_{mpq} R^{-}_{mpq} e^{j\beta^{0}_{pq} z} \Psi_{pq}(\underline{r}) \underline{K}_{mpq} \tag{2.30}$$

$$\underline{H}^{-}(\underline{r}, z) = \underline{H}^{inc} - \sum_{mpq} \eta^{0}_{mpq} R^{-}_{mpq} e^{j\beta^{0}_{pq} z} \Psi_{pq}(\underline{r}) \cdot \hat{z} \times \underline{K}_{mpq} \tag{2.31}$$

For $0 \leq z \leq z_1$

$$\underline{E}^1(\underline{r},z)=\sum_{mpq}(T^1_{mpq}e^{-j\beta^1_{pq}z}+R^1_{mpq}e^{j\beta^1_{pq}z})\Psi_{pq}(\underline{r})\underline{K}_{mpq} \tag{2.32}$$

$$\underline{H}^1(\underline{r},z)=\sum_{mpq}\eta^1_{mpq}(T^1_{mpq}e^{-j\beta^1_{pq}z}-R^1_{mpq}e^{j\beta^1_{pq}z})\Psi_{pq}(\underline{r})\cdot\hat{z}\times\underline{K}_{mpq} \tag{2.33}$$

For $z \geq z_1$

$$\underline{E}^+(\underline{r},z)=\sum_{mpq}T^+_{mpq}e^{-j\beta^0_{pq}z}\Psi_{pq}(\underline{r})\underline{K}_{mpq} \tag{2.34}$$

$$\underline{H}^+(\underline{r},z)=\sum_{mpq}\eta^0_{mpq}T^+_{mpq}e^{-j\beta^0_{pq}z}\Psi_{pq}(\underline{r})\cdot\hat{z}\times\underline{K}_{mpq} \tag{2.35}$$

where the incident field is expressed in terms of the zeroth order Floquet mode (*p, q* = 0):

$$\underline{E}^{inc}(\underline{r},z)=\sum_{m=1}^{2}T^{inc}_{m00}e^{-j\beta^0_{00}z}\Psi_{00}(\underline{r})\underline{K}_{m00} \tag{2.36}$$

$$\underline{H}^{inc}(\underline{r},z)=\sum_{m=1}^{2}\eta^0_{m00}T^{inc}_{m00}e^{-j\beta^0_{00}z}\Psi_{00}(\underline{r})\cdot\hat{z}\times\underline{K}_{m00} \tag{2.37}$$

The standard electromagnetic boundary conditions are applied at the interfaces:

At $z = z_1$ the tangential electric and magnetic fields are continuous, i.e.

$$\underline{E}^1(\underline{r}, z_1) = \underline{E}^+(\underline{r}, z_1) \text{ and } \underline{H}^1(\underline{r}, z_1) = \underline{H}^+(\underline{r}, z_1) \tag{2.38}$$

At $z = 0$ it is:

$$\begin{aligned} &\underline{E}^-(\underline{r}, 0) = \underline{E}^1(\underline{r}, 0) \\ &\underline{H}^-(\underline{r}, 0) - \underline{H}^1(\underline{r}, 0) = \hat{z} \times \underline{J}(\underline{r}, 0) \qquad \text{where } \underline{r} \in A' \end{aligned} \tag{2.39}$$

A' is the conducting area of the unit cell and $\underline{J}$ is the electric current density on the element.

The integral equation is formed by enforcing the boundary condition that the tangential electric field component should vanish at the conducting element surface:

$$\begin{aligned} &\underline{E}^-(\underline{r}, 0) = 0 \qquad \underline{r} \in A' \\ &\underline{E}^{inc}(\underline{r}, 0) + \sum_{mpq} R^-_{mpq} \Psi_{pq}(\underline{r}) \underline{K}_{mpq} = 0 \end{aligned} \tag{2.40}$$

With some algebraic manipulation the EFIE at $z = 0$ can be derived:

$$\sum_{mpq} \frac{1}{A(\eta^0_{mpq} + \zeta_{mpq}\eta^1_{mpq})} \tilde{J}_{mpq} \Psi_{pq}(\underline{r}) \underline{K}_{mpq} = \sum_{m00} \left(1 + \rho^0_{m00}\right) T^{inc}_{m00} \Psi_{00}(\underline{r}) \underline{K}_{m00} \tag{2.41}$$

where,

$$\rho^0_{m00} = \frac{\eta^0_{m00} - \zeta_{m00}\eta^1_{m00}}{\eta^0_{m00} + \zeta_{m00}\eta^1_{m00}}$$

$$\zeta_{mpq} = \frac{1-\rho_{mpq}}{1+\rho_{mpq}}$$

$$\rho_{mpq} = \frac{\eta^1_{mpq} - \eta^0_{mpq}}{\eta^1_{mpq} + \eta^0_{mpq}} e^{-2j\beta^1_{pq} z_1}$$

$\tilde{J}_{mpq}$ is the Floquet transform of the current density and is defined by the inner product:

$$\tilde{J}_{mpq} = \left\langle \underline{J}(\underline{r}) \cdot \underline{\kappa}_{mpq}, \Psi_{pq}(\underline{r}) \right\rangle_{A'} = \underline{\tilde{J}}_{pq} \cdot \underline{\kappa}_{mpq} \tag{2.42}$$

The reflected and transmitted field amplitudes are written in terms of $\tilde{J}_{mpq}$ as follows:

$$R^-_{mpq} = \delta_{p0}\delta_{q0}\rho^0_{m00}T^{inc}_{m00} - \frac{1}{\eta^0_{mpq} + \zeta_{mpq}\eta^1_{mpq}} \frac{\tilde{J}_{mpq}}{A}$$

$$(2.43)$$

$$T^+_{mpq} e^{-j\beta^0_{mpq} z_1} = \tau^1_{mpq} \left(\delta_{p0}\delta_{q0}(1+\rho^0_{m00})T^{inc}_{m00} - \frac{1}{\eta^0_{mpq} + \zeta_{mpq}\eta^1_{mpq}} \frac{\tilde{J}_{mpq}}{A} \right)$$

where

$$\tau^1_{mpq} = \frac{e^{-j\beta^1_{mpq} z_1} + \rho_{mpq} e^{j\beta^1_{mpq} z_1}}{1+\rho_{mpq}}$$

and δ_{ij} is Kronecker's symbol, defined by

$$\begin{aligned} \delta_{ij} &= 1 \qquad i = j \\ &= 0 \qquad i \neq j \end{aligned}$$

2.4.3 Double layer array

In this section, the analysis is extended to a double layer array structure shown in Fig. 2.9. The arrays are separated by two different dielectric layers, one used as a substrate to the first array and the other as spacer. The substrate of the second array is also taken into account. For the two-layer array structure studied here, two coupled EFIEs will be formed, each containing terms for the currents in both arrays. The Coupled Integral Equations (CIEs) are developed assuming the same number of Floquet modes for the unit cells on each array, such that the same Floquet indices p and q denote the same order Floquet mode in each unit cell of the two arrays. In addition, it is assumed that the lattices in the two arrays are identical. Some intermediate steps are omitted, since the is based on superposition of field, [9].

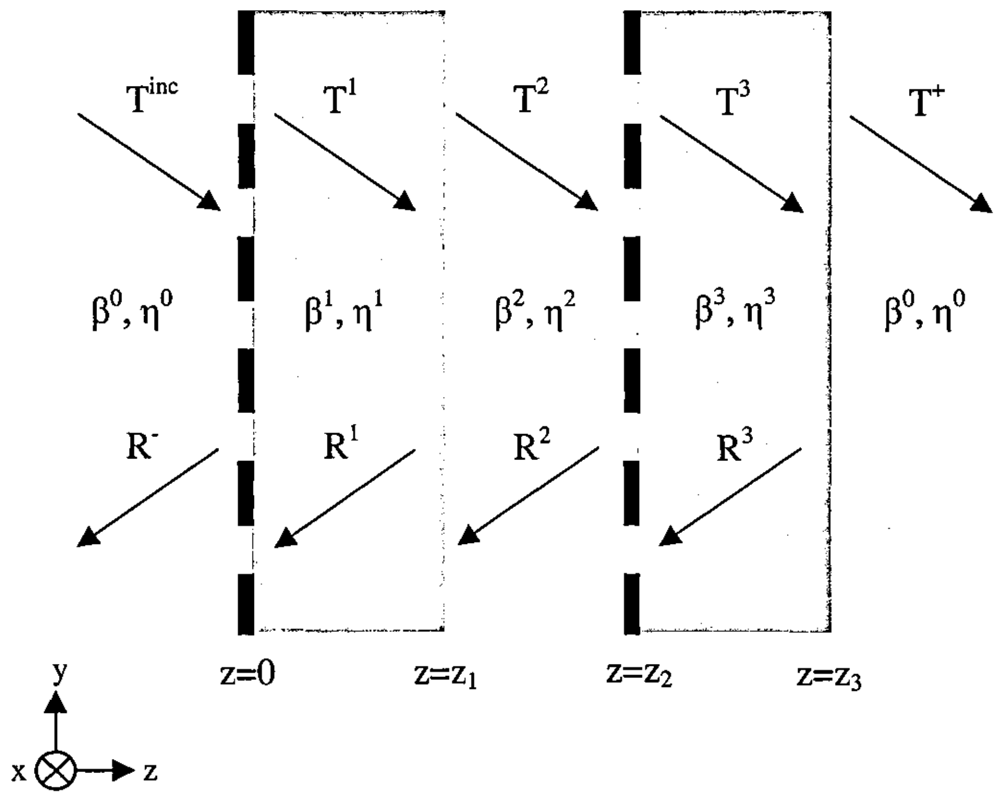

Figure 2.9 Cross section of double layer array structure

As in section 2.3.2, the tangential fields in the different media are expanded in terms of TM and TE vector Floquet modes:

For $z \leq 0$

$$\underline{E}^{-}(\underline{r}, z) = \underline{E}^{inc} + \sum_{mpq} R_{mpq}^{-} e^{j\beta_{pq}^{0} z} \Psi_{pq}(\underline{r}) \underline{K}_{mpq} \tag{2.44}$$

$$\underline{H}^{-}(\underline{r}, z) = \underline{H}^{inc} - \sum_{mpq} \eta_{mpq}^{0} R_{mpq}^{-} e^{j\beta_{pq}^{0} z} \Psi_{pq}(\underline{r}) \cdot \hat{z} \times \underline{K}_{mpq} \tag{2.45}$$

For $0 \leq z \leq z_1$

$$\underline{E}^{1}(\underline{r}, z) = \sum_{mpq} (T_{mpq}^{1} e^{-j\beta_{pq}^{1} z} + R_{mpq}^{1} e^{j\beta_{pq}^{1} z}) \Psi_{pq}(\underline{r}) \underline{K}_{mpq} \tag{2.46}$$

$$\underline{H}^{1}(\underline{r}, z) = \sum_{mpq} \eta_{mpq}^{1} (T_{mpq}^{1} e^{-j\beta_{pq}^{1} z} - R_{mpq}^{1} e^{j\beta_{pq}^{1} z}) \Psi_{pq}(\underline{r}) \cdot \hat{z} \times \underline{K}_{mpq} \tag{2.47}$$

For $z_1 \leq z \leq z_2$

$$\underline{E}^{2}(\underline{r}, z) = \sum_{mpq} (T_{mpq}^{2} e^{-j\beta_{pq}^{2} z} + R_{mpq}^{2} e^{j\beta_{pq}^{2} z}) \Psi_{pq}(\underline{r}) \underline{K}_{mpq} \tag{2.48}$$

$$\underline{H}^{2}(\underline{r}, z) = \sum_{mpq} \eta_{mpq}^{2} (T_{mpq}^{2} e^{-j\beta_{pq}^{2} z} - R_{mpq}^{2} e^{j\beta_{pq}^{2} z}) \Psi_{pq}(\underline{r}) \cdot \hat{z} \times \underline{K}_{mpq} \tag{2.49}$$

For $z_2 \leq z \leq z_3$

$$\underline{E}^{3}(\underline{r}, z) = \sum_{mpq} (T_{mpq}^{3} e^{-j\beta_{pq}^{3} z} + R_{mpq}^{3} e^{j\beta_{pq}^{3} z}) \Psi_{pq}(\underline{r}) \underline{K}_{mpq} \tag{2.50}$$

$$\underline{H}^3(\underline{r},z)=\sum_{mpq}\eta^3_{mpq}(T^3_{mpq}e^{-j\beta^3_{pq}z}-R^3_{mpq}e^{j\beta^3_{pq}z})\Psi_{pq}(\underline{r})\cdot\hat{z}\times\underline{K}_{mpq} \tag{2.51}$$

For $z \geq z_3$

$$\underline{E}^+(\underline{r},z)=\sum_{mpq}T^+_{mpq}e^{-j\beta^0_{pq}z}\Psi_{pq}(\underline{r})\underline{K}_{mpq} \tag{2.52}$$

$$\underline{H}^+(\underline{r},z)=\sum_{mpq}\eta^0_{mpq}T^+_{mpq}e^{-j\beta^0_{pq}z}\Psi_{pq}(\underline{r})\cdot\hat{z}\times\underline{K}_{mpq} \tag{2.53}$$

where the incident field is given by Eqns (2.36) and (2.37)

The standard boundary conditions are applied at the interfaces. In the case of the interfaces between different dielectrics only, the boundary condition has the form of Eqn. (2.38) and in the presence of an array in takes the form of Eqn. (2.39). Of course, the appropriate indices should be used. The integral equations can be formed by enforcing the tangential electric field on the conducting element to be zero.

At $z=0$

$$\underline{E}^-(\underline{r},0)=0 \qquad \underline{r}\in A_1'$$

$$\underline{E}^{inc}(\underline{r},0)+\sum_{mpq}R^-_{mpq}\Psi_{pq}(\underline{r})\underline{K}_{mpq}=0 \tag{2.54}$$

and at $z=z_2$

$$\underline{E}^2(\underline{r},z_2)=0 \qquad \underline{r}\in A_2' \tag{2.55}$$

$$\sum_{mpq} (T_{mpq}^2 e^{-j\beta_{pq}^2 z_2} + R_{mpq}^2 e^{j\beta_{pq}^2 z_2}) \Psi_{pq}(\underline{r}) \underline{K}_{mpq} = 0$$

where A_1' and A_2' are the conducting areas of the first and second layer unit cells respectively.

With some algebraic manipulation the EFIEs can be formed:

At $z = 0$ the EFIE is given by:

$$\frac{1}{A} \sum_{mpq} \tau_{mpq}^0 (\tau_{mpq}^1 \tau_{mpq}^2 \tilde{J}_{mpq}^2 + \tilde{J}_{mpq}^1) \Psi_{pq}(\underline{r}) \underline{K}_{mpq} = \sum_{m00} \left(1 + \rho_{m00}^0\right) T_{m00}^{inc} \Psi_{00}(\underline{r}) \underline{K}_{m00} \tag{2.56}$$

and at $z = z_2$ the EFIE is:

$$\begin{aligned} &\frac{1}{A} \sum_{mpq} \tau_{mpq}^2 (\Omega_{mpq} \tilde{J}_{mpq}^2 + \tau_{mpq}^0 \tau_{mpq}^1 \tilde{J}_{mpq}^1) \Psi_{pq}(\underline{r}) \underline{K}_{mpq} \\ &\quad = \sum_{m00} \tau_{mpq}^0 \tau_{mpq}^2 \left(1 + \rho_{m00}^0\right) T_{m00}^{inc} \Psi_{00}(\underline{r}) \underline{K}_{m00} \end{aligned} \tag{2.57}$$

where

$$\tau_{mpq}^0 = \frac{1 + \rho_{mpq}^0}{2\eta_{mpq}^0}$$

$$\tau_{mpq}^n = \frac{e^{-j\beta_{pq}^n z_n} + \rho_{mpq}^n e^{j\beta_{pq}^n z_n}}{e^{-j\beta_{pq}^n z_{n-1}} + \rho_{mpq}^n e^{j\beta_{pq}^n z_{n-1}}} \qquad n = 1, 2$$

$$\zeta_{mpq}^n = \frac{e^{-j\beta_{pq}^n z_{n-1}} - \rho_{mpq}^n e^{j\beta_{pq}^n z_{n-1}}}{e^{-j\beta_{pq}^n z_{n-1}} + \rho_{mpq}^n e^{j\beta_{pq}^n z_{n-1}}}, \qquad n = 1, 2, 3$$

$$\rho^n_{mpq} = \frac{\eta^n_{mpq} - \zeta^{n+1}_{mpq}\eta^{n+1}_{mpq}}{\eta^n_{mpq} + \zeta^{n+1}_{mpq}\eta^{n+1}_{mpq}} e^{-2j\beta^n_{pq}z_n} \qquad n = 1,2,3$$

$$\Omega_{mpq} = \tau^1_{mpq}\tau^2_{mpq}\left(\tau^0_{mpq}\tau^1_{mpq} + \frac{e^{j\beta^1_{pq}z_1} - e^{-j\beta^1_{pq}z_1}}{2\eta^1_{mpq}}\right) + \frac{e^{j\beta^2_{pq}z_2} - e^{-j\beta^2_{pq}z_2}}{2\eta^2_{mpq}}$$

$\tilde{J}^1_{mpq}$ and $\tilde{J}^2_{mpq}$ are the Floquet transforms of the electric current densities $\underline{J}^1$ and $\underline{J}^2$, induced on the elements at $z = 0$ and $z = z_2$ respectively. They are defined by the inner products:

$$\tilde{J}^n_{mpq} = \left\langle \underline{J}^n(\underline{r}) \cdot \underline{K}_{mpq}, \Psi_{pq}(\underline{r}) \right\rangle_{A_n'} = \tilde{\underline{J}}^n_{pq} \cdot \underline{K}_{mpq} \qquad n = 1,2 \tag{2.58}$$

The reflected and transmitted field amplitudes are written in terms of the currents as follows:

$$R^-_{mpq} = \delta_{p0}\delta_{q0}\rho^0_{m00}T^{inc}_{m00} - \tau^2_{mpq}\tau^1_{mpq}\tau^0_{mpq}\frac{\tilde{J}^2_{mpq}}{A_2} - \tau^0_{mpq}\frac{\tilde{J}^1_{mpq}}{A_1}$$

$$(2.59)$$

$$T^+_{mpq} = e^{j\beta^0_{mpq}z_3}\tau^3_{mpq}\tau^2_{mpq}\left(\delta_{p0}\delta_{q0}\tau^1_{mpq}(1+\rho^0_{m00})T^{inc}_{m00} - \tau^1_{mpq}\tau^0_{mpq}\frac{\tilde{J}^1_{mpq}}{A_1} - \Omega_{mpq}\frac{\tilde{J}^2_{mpq}}{A_2}\right)$$

2.4.4 Method of moments

The method of moments (MoM) [12, 13] is an efficient technique to solve the integral equations (IEs) derived from the modal analysis of the FSS. The IEs are reduced to a linear system of equations, which can also be represented by a matrix equation. This is achieved by expanding the electric current on the unit cell as a series of orthonormal basis functions

$$\underline{J}(\underline{r}) = \sum_{n=1}^{N} c_n \underline{h}_n(\underline{r}_n) \tag{2.60}$$

where N is the finite number of functions which are used to approximate the unknown current distributions. The choice of the basis functions depends on the type of conductors (e.g. dipole, tripole, patch) used as array elements. These can be entire-domain or sub-domain basis functions [14].

In the case of the single layer array, taking the inner product of both sides of the IE, Eqn. (2.41), with the testing functions $\underline{h}_i$, results in a matrix equation of the form:

$$[Z_{in}][c_n] = [\tilde{E}_i] \tag{2.61}$$

where

$$\tilde{E}_i = \sum_{m00} \left(1 + \rho^0_{m00}\right) T^{inc}_{m00} \tilde{h}^*_i(\underline{k}_{tpq})$$

and

$$Z_{in} = \sum_{mpq} \frac{1}{A(\eta^0_{mpq} + \zeta_{mpq}\eta^1_{mpq})} \tilde{h}^*_i(\underline{k}_{tpq}) \tilde{h}_n(\underline{k}_{tpq})$$

The Ritz-Galerkin method is used here, whereby the testing functions are the same as the basis functions. The square matrix $[Z_{in}]$ is of finite order, thus the unknown current coefficients can be calculated by matrix inversion, i.e.

$$[c_n] = [Z_{in}]^{-1}[\tilde{E}_i].$$

The inversion is performed here using an elimination technique, Crout's factorisation with partial pivoting, which is available in several numerical packages.

In the case of the double layer array, the CIEs, Eqns (2.56) and (2.57), are coupled together in an equation of the form:

$$\frac{1}{A}\sum_{mpq}\begin{bmatrix}\Xi_{11} & \Xi_{12}\\ \Xi_{12} & \Xi_{22}\end{bmatrix}\begin{bmatrix}\tilde{J}^1_{mpq}\\ \tilde{J}^2_{mpq}\end{bmatrix}\Psi_{pq}\underline{K}_{mpq}=\sum_{m00}\begin{bmatrix}\Xi_{10}\\ \Xi_{20}\end{bmatrix}\Psi_{00}\underline{K}_{m00} \tag{2.62}$$

where Ξ_{12} and Ξ_{21} represent the coupling between the arrays. The MoM can now be applied by expanding the unknown currents $\tilde{J}^1_{mpq}$, $\tilde{J}^2_{mpq}$ similarly to Eqn. (2.60). By substituting the expanded currents in (2.62) and taking the inner product with their corresponding test functions one arrives at:

$$\begin{bmatrix}[ZI_{11}] & [ZI_{12}]\\ [ZI_{12}] & [ZI_{22}]\end{bmatrix}\begin{bmatrix}[C_1]\\ [C_2]\end{bmatrix}=\begin{bmatrix}[EI_1]\\ [EI_2]\end{bmatrix} \tag{2.63}$$

where the submatrices ZI_{11}, ZI_{22} are similar to those that would be produced in the case of individual layers and ZI_{12}, ZI_{21} represent the coupling between the layers. It is:

$$EI_{1i}=\sum_{m00}\left(1+\rho^0_{m00}\right)T^{inc}_{m00}\tilde{h}^*_{1i}(\underline{k}_{tpq})$$

$$EI_{2i}=\sum_{m00}\tau^0_{mpq}\tau^2_{mpq}\left(1+\rho^0_{m00}\right)T^{inc}_{m00}\tilde{h}^*_{2i}(\underline{k}_{tpq})$$

and

$$ZI_{11in}=\sum_{mpq}\frac{\tau^0_{mpq}}{A}\tilde{h}^*_{1i}(\underline{k}_{tpq})\tilde{h}_{1n}(\underline{k}_{tpq})$$

$$ZI_{12in}=\sum_{mpq}\frac{\tau^0_{mpq}\tau^1_{mpq}\tau^2_{mpq}}{A}\tilde{h}^*_{1i}(\underline{k}_{tpq})\tilde{h}_{2n}(\underline{k}_{tpq})$$

$$ZI_{21in} = \sum_{mpq} \frac{\tau^0_{mpq}\tau^1_{mpq}\tau^2_{mpq}}{A} \tilde{h}^*_{2i}(\underline{k}_{tpq})\tilde{h}_{1n}(\underline{k}_{tpq})$$

and

$$ZI_{22in} = \sum_{mpq} \frac{\tau^2_{mpq}\Omega_{mpq}}{A} \tilde{h}^*_{2i}(\underline{k}_{tpq})\tilde{h}_{2n}(\underline{k}_{tpq})$$

The Ritz-Galerkin technique is used here too and Eqn. (2.63) is solved for the unknown coefficients by matrix inversion.

The size of the matrices in Eqns (2.61) and (2.63) depends on N and the number of Floquet modes chosen. Due to computational limitations, only a certain number of basis functions and Floquet modes can be chosen. Therefore, to ensure the accuracy of the analysis, the relative convergence must be examined [15]. Usually, the Floquet mode number is increased keeping the same number of current basis functions. A sufficient number of Floquet harmonics is needed so that at least the main lobe of the spectrum is included. In addition, the number of basis functions must be sufficient for a reasonably accurate modeling of the induced current. Convergence tests for the several array geometries used will be discussed in Chapters 3 and 4.

2.4.5 Reflection and transmission coefficients

The complex reflection and transmission coefficients are calculated here for the zero order propagating mode. This is the fundamental mode, always propagating. The reflection and transmission coefficients are defined as the projection of the total electric fields on to the incident field direction $\underline{B}^{inc}$. They are also referred to as the copolar component, $\underline{E}^{rc}$ at the first interface (say $z = z_0$) and $\underline{E}^{tc}$ at the last interface (say $z = z_2$ as in the double layer case):

$$\underline{E}^{rc}(\underline{r}, z_0) = E^{rc}(\underline{r}, z_0)\underline{B}^{inc} \tag{2.64}$$

where

$$E^{rc}(\underline{r}, z_0) = \underline{E}^{rT}(\underline{r}, z_0)\underline{B}^{inc}$$

and in transmission

$$\underline{E}^{tc}(\underline{r}, z_2) = E^{tc}(\underline{r}, z_2)\underline{B}^{inc} \tag{2.65}$$

where

$$E^{tc}(\underline{r}, z_2) = \underline{E}^{tT}(\underline{r}, z_2)\underline{B}^{inc}$$

The total reflected electric field at $z = z_0$ and total transmitted electric field at $z = z_2$ can also be expressed in terms of:

$$\underline{E}^{rT}(\underline{r}, z_0) = (R_x^r\hat{x} + R_y^r\hat{y} + R_z^r\hat{z})e^{j\beta_{pq}z_0}\Psi_{pq}(\underline{r}) \tag{2.66}$$

where $$R_x^r = R_{mpq}^{-}\underline{K}_{m00x}$$

$$R_y^r = R_{mpq}^{-}\underline{K}_{m00y}$$

$$R_z^r = -\frac{(R_x^r \sin\theta\cos\phi + R_y^r \sin\theta\sin\phi)}{\cos\theta}$$

and

$$\underline{E}^{tT}(\underline{r}, z_2) = (T_x^t\hat{x} + T_y^t\hat{y} + T_z^t\hat{z})e^{-j\beta_{pq}z_2}\Psi_{pq}(\underline{r}) \tag{2.67}$$

where $T_x^t = T_{mpq}^{+} \underline{K}_{m00x}$

$$T_y^t = T_{mpq}^{+} \underline{K}_{m00y}$$

$$T_z^t = -\frac{(T_x^t \sin\theta \cos\phi + T_y^t \sin\theta \sin\phi)}{\cos\theta}$$

The complex reflection and transmission coefficients in the copolar direction are given by:

$$R_{coeff}^{cpo} = \frac{E^{rc}(\underline{r}, z_0)}{E^{Tinc}(\underline{r}, z_0)} = R_x^r B_x^{inc} + R_y^r B_x^{inc} + R_z^r B_z^{inc} \tag{2.68}$$

$$T_{coeff}^{cpo} = \frac{E^{tc}(\underline{r}, z_2)}{E^{Tinc}(\underline{r}, z_2)} = T_x^t B_x^{inc} + T_y^t B_x^{inc} + T_z^t B_z^{inc} \tag{2.69}$$

The values of magnitude and phase of the reflection coefficient given by Eqn. (2.68) will be inserted in Eqns (2.12) and (2.13) derived from the ray analysis (see section 2.2) in order to predict the leaky-wave antenna gain and radiation patterns. Eqns (2.68) and (2.69) provide the reflection and transmission response of the PRSs and they will be used in the design of PRSs in Chapters 3 and 4.

2.5 Ensemble

A commercially available simulation package, Ensemble^{TM}, has been used in a first attempt to model the finite size of the PRS arrays in the leaky-wave antenna. Ensemble is a 2.5D electromagnetic simulation software package that computes full-wave fields for microstrip and planar microwave structures, including planar antennas [16]. The simulation features available in the package include S-parameters, near and far-field radiation, surface currents and bistatic radar cross section.

The simulation technique used in Ensemble is based on the mixed potential integral equation (MPIE) [17]. The method of moments (MoM) is applied to the MPIE to solve for J, the current distribution on the surfaces of the model. The current is expressed in terms of sub-domain basis functions. The surface of the geometric model is automatically divided into triangles, which form the mesh. On each triangle, the components of the current that are normal to the three edges of the triangle are stored. The current inside each triangle is the superposition of these normal values. As in the majority of simulation methods based on meshing, the level of accuracy increases with the resolution of the mesh. Higher resolution typically gives more accurately results but increases considerably the size of the simulation in terms of required computer memory. Thus, there is a trade-off between the size of the mesh and the amount of available computing resources. Usually, it is desirable to use a mesh that is fine enough to obtain an accurate current solution but not so fine that it overwhelms the available computer memory and processing power.

To produce an optimal mesh, Ensemble uses an iterative process in which the mesh is automatically refined in critical regions. First, it generates a solution based on a coarse initial mesh. Then, it refines the mesh in critical areas and generates a new solution. When the current and charge distributions on the structure converge to within the desired precision, the system breaks out of the loop. The technique is called adaptive meshing. Alternatively, a fixed dense mesh can be used by specifying a frequency near the upper end of the sweep range. A uniform mesh is generated however there is no indication about the convergence and hence the accuracy of the simulation.

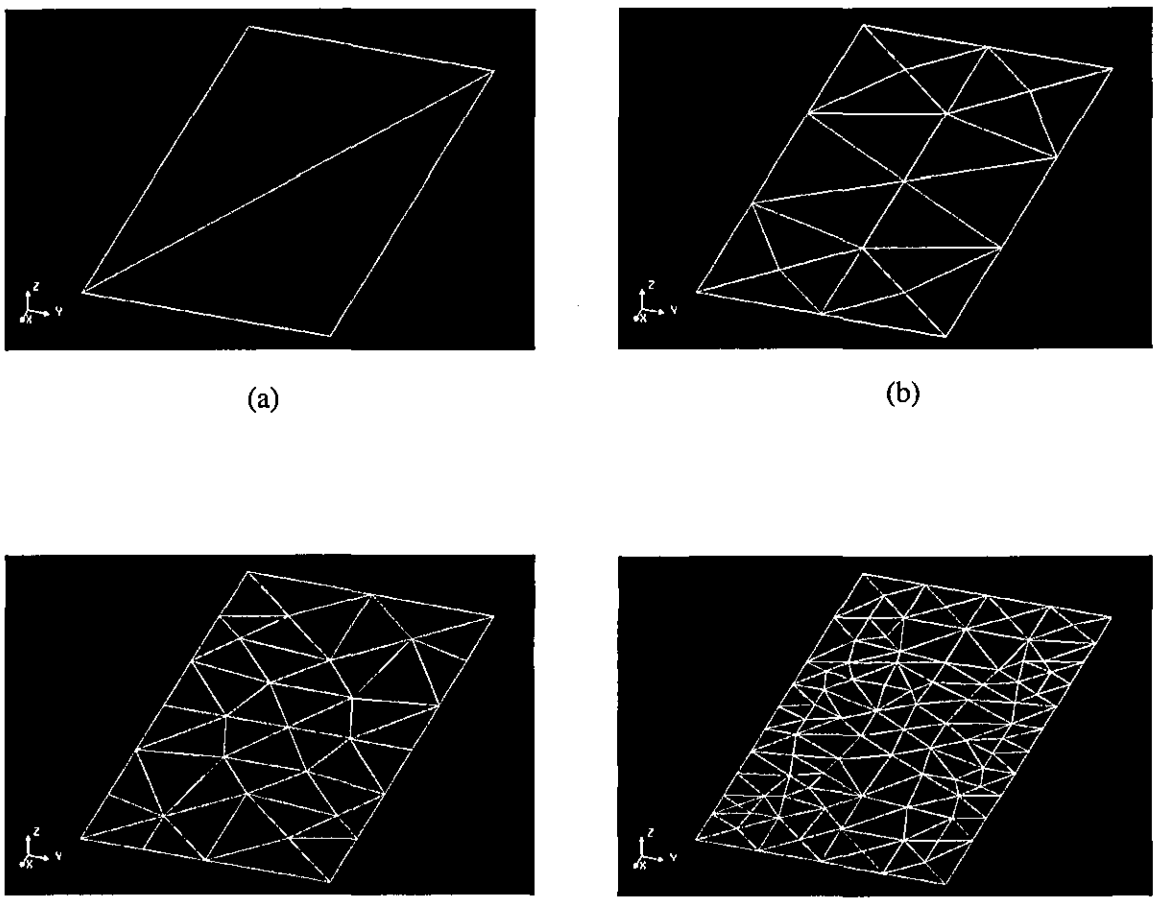

(a) (b) (c) (d)

Figure 2.10 (a) Initial mesh; (b) Mesh after adaptive pass 1; (c) Mesh after adaptive pass 2; (d) Mesh after adaptive pass 3

To illustrate the adaptive mesh technique, a rectangular aperture in an infinite ground plane under normal plane wave illumination is shown in Fig. 2.10. The figure shows four different meshes generated by successive adaptive runs.

The modelling of waveguides and 3D structures in general is not possible in Ensemble, with the exception of certain cavity models. The excitation may be an edge port, a probe or a plane wave. A plane wave excitation will be used to model the waveguide aperture in an infinite ground plane, as discussed in Chapter 3. The result obtained is the radar cross section (RCS) which is represented by [16]:

$$\sigma = \frac{4\pi r^2 \left|E_{scat}\right|^2}{\left|E_{inc}\right|^2} \tag{2.70}$$

where:

E_{scat} is the E-field of the scaterred waves

E_{inc} is the incident E-field. This is assumed to have a value of one.

The ratio of the RCS of the antenna (grounded primary aperture + PRS array) at boresight, σ_{ant}, over the RCS of the primary aperture alone, σ_{ap}, yields the boresight gain G_{rel} of the antenna relative to the gain of the primary aperture [18]:

$$\frac{\sigma_{ant}}{\sigma_{ap}} = \frac{\left|E_{sc.ant}\right|^2}{\left|E_{sc.ap}\right|^2} = \frac{P_{o,ant}}{P_{o,ap}} = G_{rel} \tag{2.71}$$

where $P_{o,ant}$ and $P_{o,ant}$ the power received at boresight from the antenna and the primary aperture alone respectively.

2.6 Time-Domain 3-D Simulation Methods

Time domain methods have been widely used in recent years for simulating the temporal behaviour of electromagnetic fields. One of the key attributes for the popularity of these methods is the significant growth in computer processing power and memory capacity, particularly during the last decade. Another important advantage of time-domain methods is that they can cover a wide range of frequencies with a single simulation run, by using a time domain excitation pulse (such as a Gaussian pulse) [19].

Two of the most popular and extensively researched 3-D time domain methods have been employed for a rigorous simulation of the antenna structure in its entirety. These are the Finite Difference Time Domain (FDTD) method and the Transmission Line Modeling (TLM) method. For the implementation of the former we have used a freeware beta version of the electromagnetic simulator LC [20], developed by Cray research. For the latter we have used a commercially available software package, Microstripes^{TM}, developed originally by KCC (now owned by Flomerics). A brief introduction to the software packages as well as a short description of the two numerical methods and their differences is given in this section.

2.6.1 LC (FDTD)

FDTD is currently one of the most popular electromagnetic modeling techniques. It was first presented by Yee [21] in 1966 and it has attracted a lot of interest during the last decade, mainly due to the significant advances in modern computers. A large amount of literature can be found, starting from some first improvements to the initial Yee-algorithm, [22], to further advances and applications of the method to antennas, scattering and EMC problems [23].

FDTD is an inherently simple technique based on Maxwell's curl equations in their differential form [24, 25]. The equations are simply modified to central-difference equations for a discretised three-dimensional space with discrete time steps. They are solved in a leap-frog manner; that is the electric field is solved at a given instant in time, then the magnetic field is solved at the next instant and the process is repeated likewise for a certain number of time steps until a steady state is reached. In order to use FDTD a computational domain must be established. The computational domain is simply a rectangular volume enclosing the model and it is discretised into a large number of cells. The dielectric, permeable, lossy and conducting material properties of each cell are incorporated into the field updates, which are performed iteratively in small time steps. An important factor in the FDTD method is that the E and H fields are computed at points separated half a cell. The time step duration is a function of the smallest cell size in the structure. In addition, the dimensions of each cell are set by the highest frequency which is required in the analysis. Typically a cell size of $\lambda/10$, where λ the minimum wavelength, should be used, although smaller cell sizes in the scale of say $\lambda/30$ are often required for more accurate results. The fundamental criterion is that the field should be nearly constant over a cell.

LC is an electromagnetic simulation tool based on the FDTD technique. It was originally developed by Cray research and it is being distributed in executable form for users of SGI and Cray computers. It has fully dynamic memory allocation and can use multiple processors in parallel to reduce the time to solution. Recently a Linux version has also become available .

LC performs its simulation within a rectangular three-dimensional mesh. It allows the user to define three different types of blocks within the mesh: materials, sources and probes. Source blocks have user defined electric or magnetic field waveforms on their surfaces, which radiate into the rest of the mesh. Probe blocks are particular regions of the mesh where information on the field values can be extracted. In addition, LC offers several types of boundary conditions. The perfectly matched layer (PML) boundary condition provides very low reflection values of signal back into the structure, although it requires more memory and computing time [25, 26]. However, the boundaries can be placed closer to the modelled structure, typically as close as 10 cells, which reduces the size of the simulation. The low reflection values are particularly important in the calculation of radiation patterns and gain. One of the limitations of the package is that non-uniform meshing is not available with PML boundaries, which causes problems in modelling certain structures. Furthermore, symmetry conditions such as electric and magnetic walls, are not available in the program. Thus the symmetries of structures under investigation cannot be exploited to reduce the computational space.

LC was used for a 3D-simulation of several leaky-wave antenna designs. For the simulations an eight-processor J90 Cray machine has been used, provided by Advantica (formerly British Gas). A large amount of memory (4Gb) was available. However, only ftp and telnet access was allowed due to security firewalls.. The graphical user interface where the antenna models were created was running on an SGI computer in Loughborough university and later on a Linux PC (when the Linux version became available). Towards the last stages of the research the access to the Cray machine was withdrawn and thus LC was not used in the last leaky-wave antenna designs.

2.6.2 Microstripes (TLM)

The TLM method was first presented by Johns and Beurle, [27], in 1971. Johns and Beurle used the earlier proposed principles of equivalent transmission line circuits and their application to the solution of electromagnetic problems, along with the theory of pulse propagation on transmission lines to develop a numerical technique compatible with computational methods for the solution of two-dimensional electromagnetic problems. This method has been used for many applications and it has been further developed [28]. The recent increase in computational power allowed for its widespread use.

TLM is a 'time-marching' scheme very similar to FDTD [29]. Instead of volume cells in space, the structure consists of nodes which are modelled as connected by a mesh of transmission lines with additional circuit elements (L, C, R) to model specific geometries. The voltages and currents in these lines represent the electric and magnetic fields, providing a considerable advantage over FDTD in that the E and H fields are determined at the same point. This makes the determination of impedance very much easier and also allows for changing the cell size more readily. Although not as extensively researched as FDTD, good accuracy has been reported in a number of applications. However, the problems regarding runtime and cell size still remain the same as in FDTD.

Microstripes is a 3-D electromagnetic simulation software package distributed by Flomerics and it is the most extensively used TLM based simulator. The most recent version, Microstripes v5.6, runs on a PC and offers a complete set of features that are usually required for electromagnetic simulations [30]. Some of them are the advanced modelling interface, S-parameters calculation, non-uniform meshing (multi-gridding), PML absorbing boundary conditions and symmetry conditions such as electric and magnetic walls. By using features as multi-gridding and symmetry conditions, depending on the simulated geometry, the solution time can be significantly reduced. Good visualisation tools such as surface currents, near fields and 3D radiation patterns are also available.

2.7 Conclusions

The methods used to analyse the leaky-wave antenna structure have been presented in this chapter. The leaky-wave action of PRSs has been described mathematically using an approximate ray analysis. Based on this analysis, the optimum PRS reflection characteristics for high-gain and wideband antenna performance have been produced. The optimum PRS response is used as guideline in the design of PRS arrays in Chapters 3 and 4. The plane-wave modal analysis used to compute the reflection response of PRS arrays has also been presented for single and double layer array structures supported on dielectric substrates. Finally, a brief introduction has been given into the simulation packages used to predict the performance on the leaky-wave antenna with small size PRSs.

References

[1] TRENTINI, G. V. : 'Partially reflecting sheet arrays', *IRE Trans. Antennas Propag.*, vol. **AP-4**, 1956, pp. 666-671

[2] KRAUSS, J. D. : 'Electromagnetics', McGraw Hill Inc, 1953

[3] STUTZMAN, W. and THIELE, G. : 'Antenna theory and design', John Wiley, New York, 1998.

[4] HECHT, E. : 'Optics', Addison-Wesley, Reading, Mass., 1990

[5] ABRAMOWITZ, S. and STEGUN, A. : 'Handbook of mathematical functions', Dover Publications Inc., New York, 1965.

[6] VERDEYEN, J. T. : 'Laser electronics', Prentice Hall Inc., 1989

[7] de LIMA, A. C. and PARKER, E. A. : 'Fabry-Perot approach to the design of double layer FSS', *IEE Proc., Microw., Antennas & Propag.*, vol. 143, No. 2, 1996, pp. 157-162

[8] FERESIDIS, A. P. and VARDAXOGLOU, J. C. : 'High gain planar antenna using optimised partially reflective surfaces', *IEE Proc., Microw., Antennas & Propag.*, vol. 148, No. 6, Dec. 2001, pp. 345-350

[9] VARDAXOGLOU, J. C. : 'Frequency Selective Surfaces: Analysis and Design', Research Studies Press, Somerset, England, 1997

[10] MONTGOMERY J. P. : 'Scattering by an infinite periodic array of thin conductors on a dielectric sheet,' *IEEE Trans. Antennas and Propagation,* vol. AP-23, No. 1, Jan. 1975, pp. 70-75,

[11] AMITAY, N., GALINDO, V. and WU, C. P. : 'Theory and Analysis of Phased Array Antennas', New York, Wiley-Interscience, 1972.

[12] HARRINGTON R. F., 'Matrix methods for fields problems' *Proc. IEEE*, vol. 55, February 1967, pp. 136-149

[13] HARRINGTON R. F., 'Field computation by moment methods', New York: MacMillan, 1968

[14] MITTRA R., CHAN C. H., and CWIK T., 'Techniques for analyzing frequency selective surfaces – A review' *Proc. IEEE*, vol. 76, No. 12, Dec. 1988, pp. 1593-1615.

[15] SHULEY, N. : 'A note on relative convergence for moment method solutions of integral equations of the first kind as applied to dichroic problems', *Electron. Lett.*, vol. 21, No. 3, 1985, pp.95-97

[16] Ansoft Corporation : 'Ensemble User's manual', © 1996-2000

[17] PETERSON, A. F., SCOTT, L. R. and MITTRA, R. : 'Computational methods for electromagnetics', IEEE Press, 1998

[18] BALANIS, C. A. : 'Antenna Theory: Analysis and Design', John Wiley, New York, 1997

[19] RAO, S. M. : 'Time Domain Electromagnetics', Academic Press, 1999

[20] LC homepage: http://lc.cray.com

[21] YEE, K. S. : 'Numerical solution of initial boundary value problems involving Maxwell's equations in isotropic media', *IEEE Trans. Antennas and Propagation*, vol. AP-14, May 1966, pp. 302-307

[22] TAFLOVE, A. and BRODWIN, M. E. : 'Numerical solution of steady-state electromagnetic scattering problems using the time-dependent Maxwell's equations', *IEEE Trans. Microw. Theory and Techniques*, vol. MTT-23, Aug. 1975, pp. 623-630

[23] SHLAGER, K. L. and SCHNEIDER, J. B. : 'A selective survey of the finite-difference time-domain literature', *IEEE Antennas and Propagation Magazine*, vol. 37, No. 4, 1995, pp. 39-56

[24] KUNZ, K. S. and LUEBBERS, R. J. : 'The Finite Difference Time Domain Method for Electromagnetics', CRC Press, Boca Raton, 1993

[25] TAFLOVE, A. : 'Advances in Computational Electrodynamics', Artech House, 1998

[26] BERENGER, J. P. : 'A perfectly matched layer for the absorption of electromagnetic waves' *Journal of Computational Physics*, vol. 114, 1994, pp. 185-200

[27] JOHNS, P. B. and BEURLE, R. L. : 'Numerical solution of 2-Dimensional scattering problems using a transmission line matrix', *Proc. IEEE*, vol. 118, 1971, pp. 1203-1209

[28] CHRISTOPOULOS, C. : 'Transmission line modelling method, TLM', IEEE Press, 1995

[29] FOSTER, P. R. : 'CAD for antenna systems', *IEE Electronics & Communication Engineering Journal*, Feb. 2000, pp. 3-14

[30] Flomerics Electromagnetics Division: 'Microstripes 5.6 reference manual:Issue 1', © 1994-2001

Chapter 3

Single Layer PRSs

3.1 Introduction

The beamforming effect of single-layer PRSs in a leaky-wave antenna configuration is investigated here. The theoretical model based on ray optics is employed for an initial prediction of the antenna gain and radiation patterns. The plane-wave modal analysis based on Floquet theorem is used to compute the frequency as well as angular reflection response of the PRS arrays. An angle-dependant analysis of the antenna, whereby the angular reflection response of the PRS is taken into account, yields an improved description of the antenna performance. Moreover, the effect of the phase as well as the amplitude of the reflection coefficient of the PRS on the antenna gain and bandwidth is studied. An optimisation procedure is carried out based upon the guidelines of the ray analysis for high-gain and wideband antenna performance. The PRS array geometry is optimised and a high gain antenna is produced using a dipole PRS. The optimisation is verified for a small size array using full wave models. Ensemble is used for the modelling of the edge effects due to the finite size of the array. In addition, the antenna in its entirety is simulated using a 3D FDTD simulation package (LC). Lastly, an efficiency test is performed by varying the size of the PRS and hence the antenna aperture.

3.2 Angle-Dependant Analysis

The ray analysis presented in section 2.2 has been used in [1, 2] to predict the radiation patterns of planar leaky-wave antennas formed by PRSs - otherwise called leaky-wave beamformers - as shown in Fig. 2.1. The analysis is restricted to large size PRSs, since it assumes an infinite size of PRS and ground plane. Due to the approximations considered in the analysis, only the beamwidth of the main lobe has been obtained thus far, as an indication of the antenna performance [2]. The reflection coefficient of the PRSs was obtained theoretically by approximate formulas [3], valid for normal incidence only.

A further development in the ray analysis can be achieved by taking into account the angle of incidence on the PRS in the calculation of the complex reflection coefficient values [4, 5]. The effect of the angle of incidence in the frequency and angular response of planar arrays (such as FSSs) is quite significant and has previously been reported [6]. In order to simulate the reflection characteristics of the PRS under plane wave illumination, the Floquet modal analysis is employed [7], resulting in an accurate computation of the reflection values as a function of the frequency as well as the incident angle.

3.2.1 Square patch PRS

A PRS comprised of an array of square copper patches is used, Fig. 3.1. The patches are of side $L = 6.75\,\text{mm}$ and they are printed on a thin polyester layer of thickness 32μm and dielectric constant 3. They are arranged in a square lattice with periodicity $D = 9.6\,\text{mm}$. The Floquet modal analysis is implemented in FORTRAN and it computes the magnitude and phase of the reflection coefficient of the square patch array. In order to simulate the current induced on the patch, entire domain basis functions have been used. For a rectangular patch with length L (y-axis) and width W (x-axis), the x and y components of the induced current can be expanded in terms of the following orthonormalised functions, [8]:

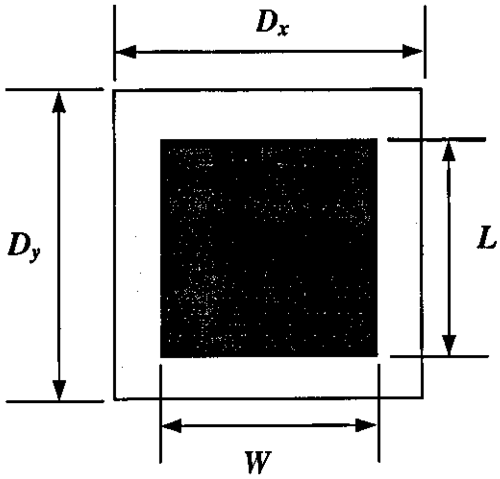

Figure 3.1 Unit cell of rectangular/square patch PRS

The x-components:

$$h_{xmn}^{c} = \sqrt{\frac{1}{NR}} \cos\left(\frac{n\pi x}{W}\right) \frac{T_m\left(\frac{2}{L}y\right)}{\left[1-\left(\frac{2}{L}y\right)^2\right]^{1/2}}, \qquad n = 1,3,...$$

$$h_{xmn}^{s} = \sqrt{\frac{1}{NR}} \sin\left(\frac{n\pi x}{W}\right) \frac{T_m\left(\frac{2}{L}y\right)}{\left[1-\left(\frac{2}{L}y\right)^2\right]^{1/2}}, \qquad n = 2,4,... \tag{3.1}$$

The y-components:

$$h_{ymn}^{c} = \sqrt{\frac{1}{NR}} \cos\left(\frac{n\pi y}{L}\right) \frac{T_m\left(\frac{2}{W}x\right)}{\left[1-\left(\frac{2}{W}x\right)^2\right]^{1/2}}, \qquad n = 1,3,...$$

$$h_{ymn}^{s} = \sqrt{\frac{1}{NR}} \sin\left(\frac{n\pi y}{L}\right) \frac{T_m\left(\frac{2}{W}x\right)}{\left[1-\left(\frac{2}{W}x\right)^2\right]^{1/2}}, \qquad n = 2,4,... \tag{3.2}$$

where $m = 0, 1, \ldots$, T_i is the ith order Chebyshev polynomial of the first kind [9], and $NR = \frac{WL}{2}$ is the normalisation factor arising from the orthogonality of the basis functions.

The Floquet transforms of the basis functions, Eqns (3.1) and (3.2), are obtained by substituting Eqns (3.1) and (3.2) into Eqn. (2.58):

$$\tilde{h}_{xmn}^{c} = \sqrt{NR}(\tilde{p}_{nx} + \tilde{q}_{nx})2\pi J_m\left(\frac{L}{2}k_y\right), \qquad n = 1,3,...$$

$$\tilde{h}_{xmn}^{s} = \sqrt{NR}\, j(-\tilde{p}_{nx} + \tilde{q}_{nx})2\pi J_m\left(\frac{L}{2}k_y\right), \qquad n = 2,4,... \tag{3.3}$$

and

$$\tilde{h}_{ymn}^{c} = \sqrt{NR}(\tilde{p}_{ny} + \tilde{q}_{ny})2\pi J_m\left(\frac{W}{2}k_x\right), \qquad n = 1,3,...$$

$$\tilde{h}_{ymn}^{s} = \sqrt{NR}\, j(-\tilde{p}_{ny} + \tilde{q}_{ny})2\pi J_m\left(\frac{W}{2}k_x\right), \qquad n = 2,4,... \tag{3.4}$$

where

$$\tilde{p}_{nx} = \text{sinc}\left[\left(k_x + \frac{n\pi}{W}\right)\frac{W}{2}\right], \quad \tilde{q}_{nx} = \text{sinc}\left[\left(k_x - \frac{n\pi}{W}\right)\frac{W}{2}\right], \tag{3.5}$$

$$\tilde{p}_{ny} = \text{sinc}\left[\left(k_y + \frac{n\pi}{L}\right)\frac{L}{2}\right], \quad \tilde{q}_{ny} = \text{sinc}\left[\left(k_y - \frac{n\pi}{L}\right)\frac{L}{2}\right] \tag{3.6}$$

J_i is the ith order Bessel function of the first kind and $\text{sinc}\,(\cdot) = \sin(\cdot)/(\cdot)$, [9].

The basis functions (3.1) and (3.2) have been chosen such that they incorporate the correct singularities for the current at the edges of the patch. This is better demonstrated in Fig. 3.2, where the y-directed basis functions, J_y, as used in the simulation code, are plotted. The x component, J_x, has exactly the same distribution, with orientation along x. Only the zeroth order Chebyshev polynomial (m=0) has been used in the code, and hence the zeroth order Bessel function in the Floquet transforms, since they approximate the induced currents sufficiently, as shown in Fig. 3.2. The functions are zero ended in the direction of the incident field and exhibit the characteristic edge singularity. Since the incident field in the plane wave measurements of the PRS as well as in the antenna structure is polarised along y, J_x is expected to be very small as compared to J_y.

Ten basis functions (Fig. 3.2), five for each axis, have been used to expand the unknown current on the patches. The convergence has been tested by increasing the number of Floquet modes. Fig. 3.3 shows the normalised frequency shift of the resonance with the number of Floquet modes used. A good relative convergence is obtained for $19\times19=361$ modes. The use of more basis functions has also been tested, but the differences in the resonance values were very small. Thus, the simulations were carried out using ten basis functions and 361 Floquet modes.

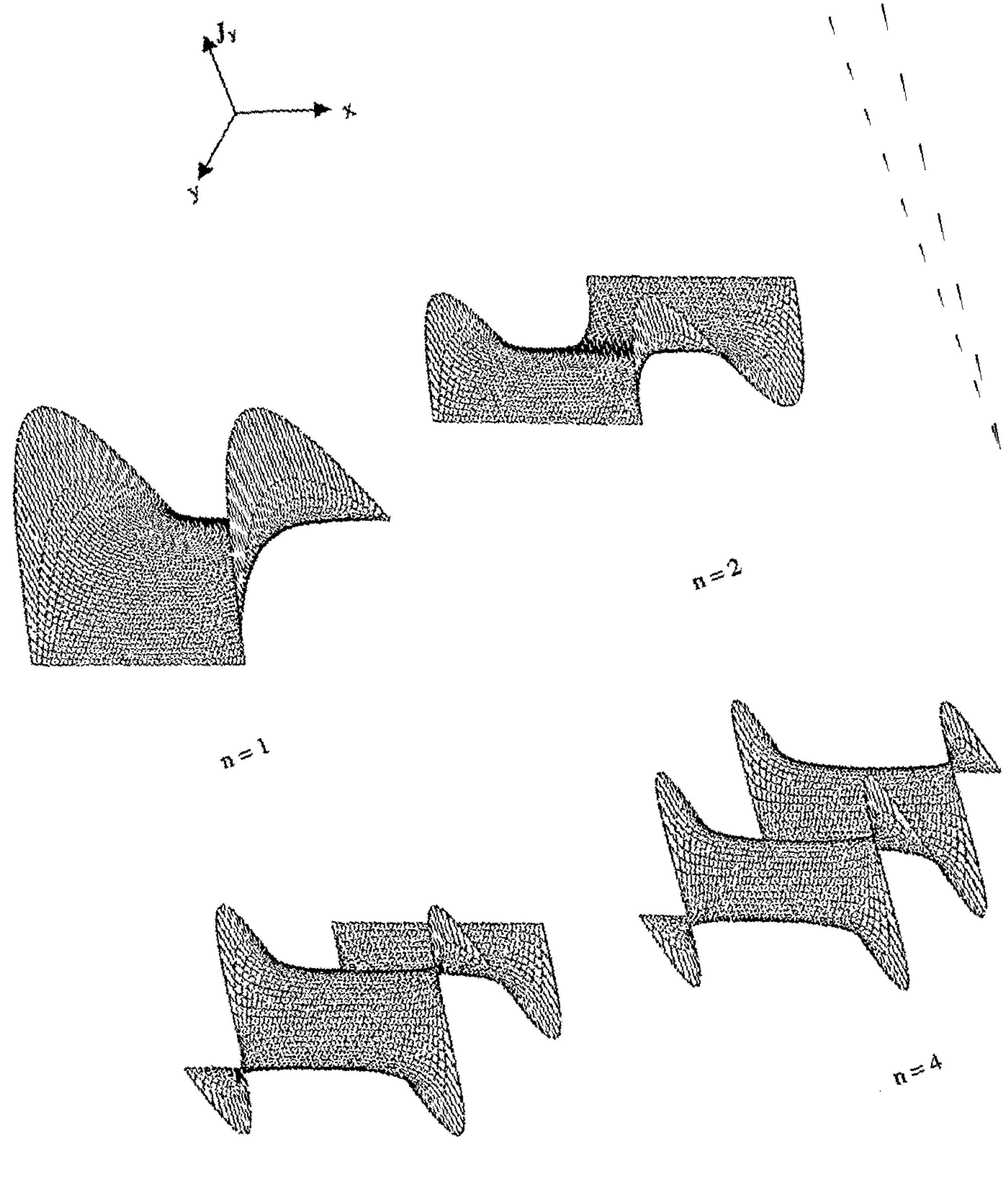

J_y
x
y
n = 1
n = 2
n = 3
n = 4

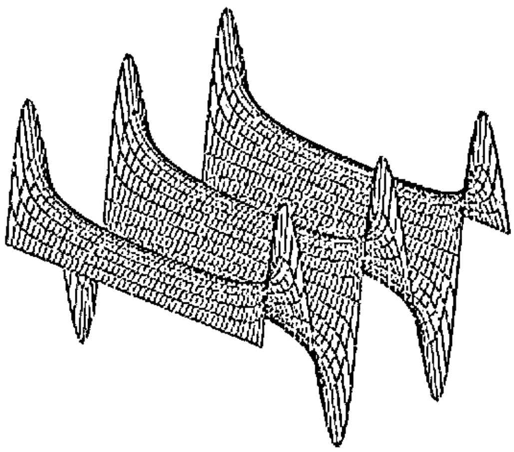

n = 5

Figure 3.2 First five basis functions for the current on the square patches

The PRS in the measurements was a $20\times20\,\text{cm}^2$ sheet placed within a solid cardboard frame and surrounded by absorbing material to eliminate diffraction. The measurements were carried out in an indoor anechoic chamber with plane wave measurement facilities. Two standard gain pyramidal horns have been used for transmitting and receiving over three bands: J-band (12-18 GHz), K-band (18-26 GHz) and Q-band (26-40 GHz). In all cases the PRS is in the far field of the horns, i.e. $r > 2D^2/\lambda_0$, where r is the distance between the horn and the PRS, D is the largest dimension of the horn and λ_0 is the wavelength of the incident field. Fig. 3.4 shows the transmission coefficient with frequency. The simulation results are in good agreement with measurements. A sharp peak appears in the simulated results at about 31 GHz due to the grating response of the array.

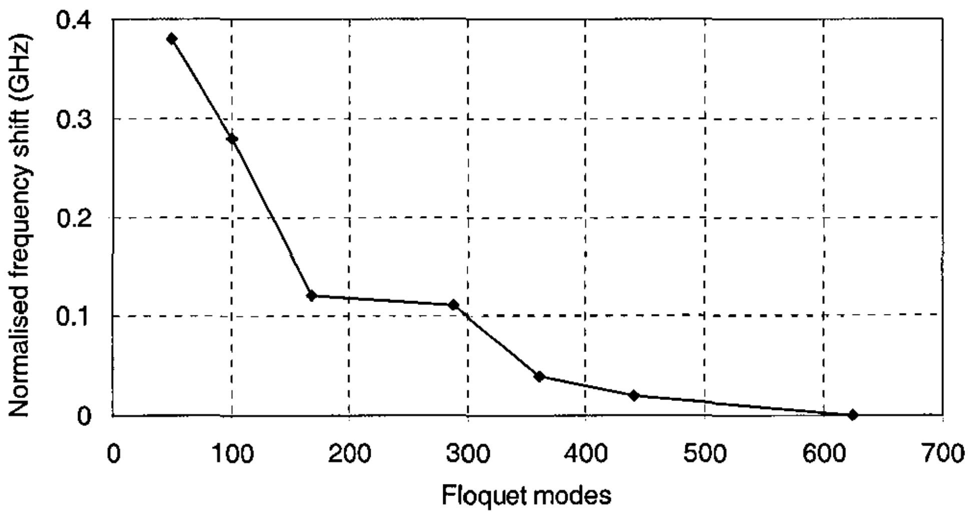

Figure 3.3 Convergence test using ten basis functions

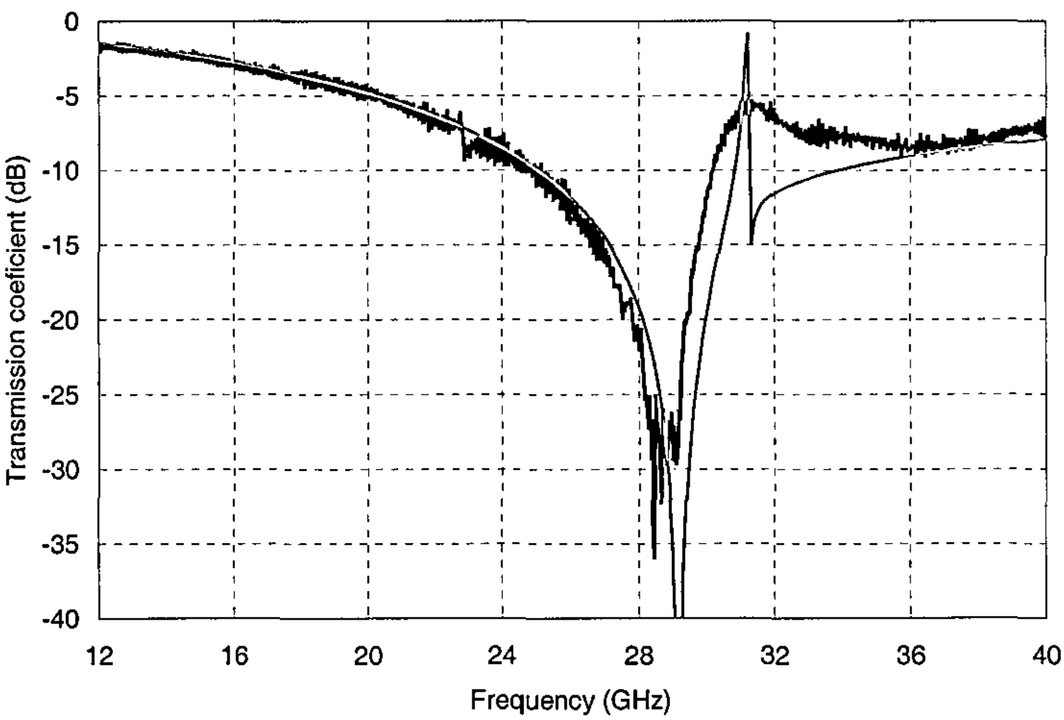

Figure 3.4 Transmission response of square patch PRS; black, measured; grey, simulation

3.2.2 Antenna performance

The square patch PRS has been used in the leaky-wave antenna configuration shown in Fig. 2.1. Measurements have been carried out in an earlier work [10]. A J-band rectangular waveguide with inner dimensions $15.8 \times 7.9\,\text{mm}^2$ was used as the primary antenna. It was mounted in a $20 \times 20\,\text{cm}^2$ aluminium ground plane and was fed by a coax-to-waveguide transition. At the frequencies of operation of the antenna, only the dominant TE_{10} mode was propagating. The PRS was placed at a distance of about 9 mm in front of the ground plane and in parallel with it. The receiving horn was placed at a distance of 1.2m from the antenna.

The frequency sweep of the boresight gain is shown in Fig. 3.5. The ray analysis presented in section 2.2 predicts the relative gain approximately, using Eqns (2.12) and (2.13), for a resonant distance of 9.75 mm. The measured gain of the grounded waveguide aperture is added to yield the overall gain. The resonant frequency, where the gain is maximum, is $f = 17.36\,\text{GHz}$. The measured maximum gain was 13.3 dBi and the predicted one 13.7 dBi.

The plane wave modal analysis has also been used to simulate the angular response of the square patch PRS at the resonant frequency. The complex reflection coefficient, magnitude and phase, was obtained, Fig. 3.6. The magnitude of the reflection coefficient initially increases with angle and it exhibits a minimum value of nearly zero reflection at about 53 degrees. This is the grating lobe angle and it appears due to the grating response of the PRS array. The grating lobes enter the visible space of the array at this angle and thus the reflection values decrease dramatically.

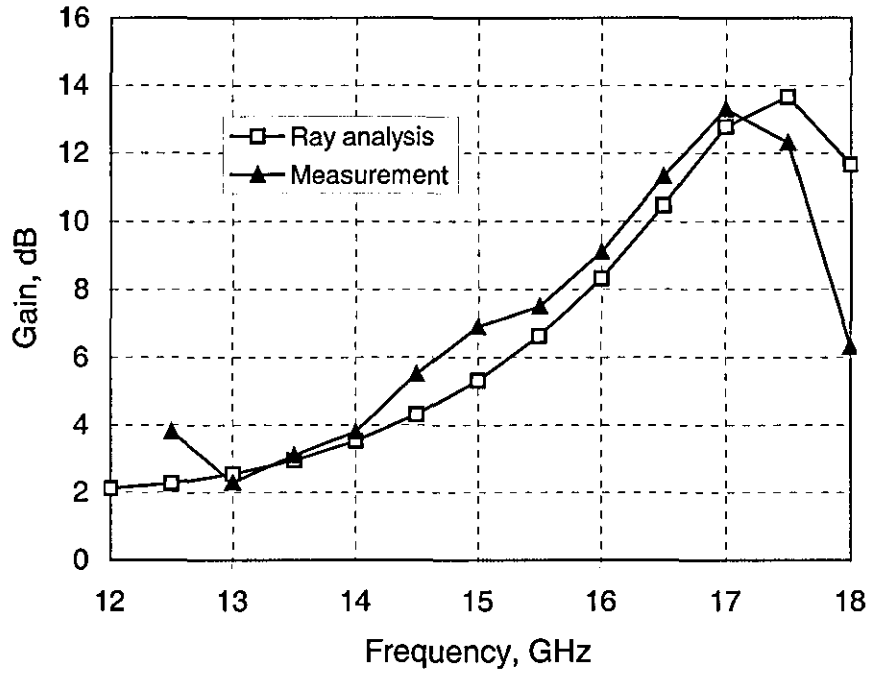

Figure 3.5 Gain of antenna with square patch PRS

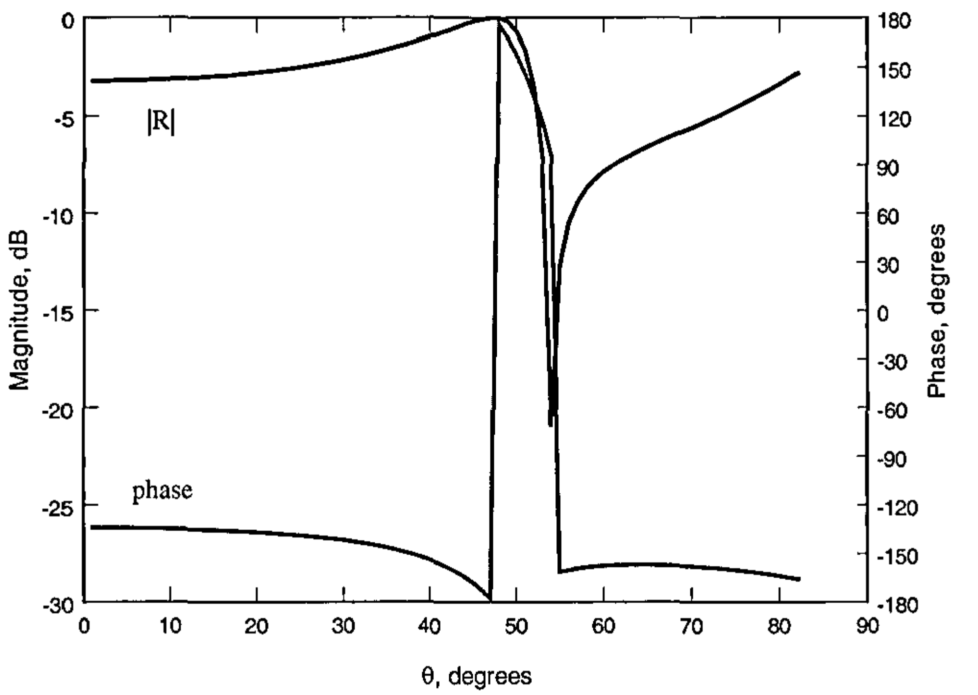

Figure 3.6 Angular response (reflection coefficient) of PRS at 17.36 GHz for TE incidence

The angle dependent values of the reflection coefficient are inserted in Eqn. (2.12) to produce the radiation pattern of the leaky-wave antenna. The result is shown in Fig. 3.7. The figure also shows the measured radiation pattern as well as the pattern calculated using the reflection coefficient values for normal incidence only, as in [2]. A comparison between the simulation results shows that the angle-dependent analysis predicts more accurately the main lobe, it detects the null and gives a good estimate of the sidelobes. The pattern of the grounded waveguide aperture has also been plotted to illustrate the beamforming caused by the PRS.

It must be noted that the angle dependent analysis presented here can only be used for PRSs of large size, e.g. PRSs of side 10λ or more. Smaller size arrays, would have altered spectral and angular responses and furthermore diffraction effects would be more dominant in the antenna performance.

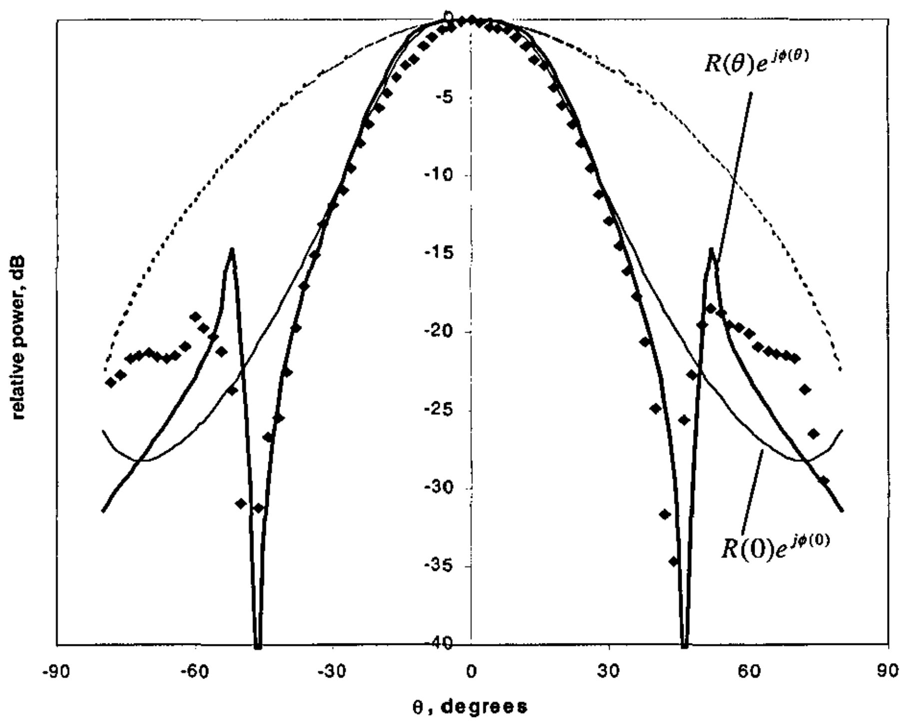

Figure 3.7: H-plane normalised radiation patterns of antenna with square patch PRS at 17.36GHz : solid lines, simulation results; dots, measurements; dashed line, grounded waveguide aperture

3.3 Optimisation of PRS for Gain and Bandwidth

The high-gain and wide bandwidth requirements discussed in section 2.3 are used here as guidelines in order to produce optimised single-layer PRS designs. Different element geometries and lattices are investigated and the advantages and disadvantages of each are discussed.

It is well known that, before resonance, the reflection coefficient magnitude of a single layer array of conducting elements (or apertures in a conducting screen) increases (decreases) with frequency. For a conducting element array the phase of the reflection coefficient is negative and decreases with frequency. At resonance (total reflection) its value becomes $-\pi$. In the case of an aperture array, the reflection phase is positive and, too, decreases with frequency until resonance (total transmission), where it becomes zero. According to the analysis in section 2.3, for a wideband antenna the optimum PRS would require its reflection coefficient to remain constant in magnitude but the phase to linearly increase with frequency, with a gradient of $4\pi L_r / c$, [11].

Several element geometries have been investigated, such as dipoles, crossed dipoles, tripoles, patches and square loops. In order to meet the said targets, an optimisation process has been carried out by adjusting the geometry of the arrays. The response of the PRSs has been computed using the plane wave Floquet modal analysis. Only normal incidence is considered, since the optimisation was carried out with regard to the antenna performance at boresight. The incident field is polarised vertically, i.e. along the y-axis.

Linear dipoles are the elements with the most simple geometry and they are relatively straightforward to compute. Since their electrical width is very small, one may use one-dimensional entire domain bases to expand the unknown current. The basis functions used here are sinusoidal [7, 8] and in the vertical y-direction, which is the direction of the incident field. They are chosen such that they are zero ended in the y-direction on the dipoles.

$$h_{ny}^{c} = \sqrt{\frac{1}{NR}} \cos\left(\frac{n\pi y}{L}\right), \qquad n = 1,3,\ldots$$

$$h_{ny}^{s} = \sqrt{\frac{1}{NR}} \sin\left(\frac{n\pi y}{L}\right), \qquad n = 2,4,\ldots \tag{3.7}$$

where $NR = WL/2$ is the normalisation factor. Substituting Eqn. (3.7) into Eqn. (2.42) yields the Floquet transform of the basis functions:

$$\underline{\tilde{h}}_{ny}^{c} = \tilde{h}_{ny}^{c} \hat{y}$$

$$\underline{\tilde{h}}_{ny}^{s} = \tilde{h}_{ny}^{s} \hat{y}$$

where

$$\tilde{h}_{ny}^{c} = \tilde{m}_x (\tilde{p}_{ny} + \tilde{q}_{ny})$$

$$\tilde{h}_{ny}^{s} = \tilde{m}_x j(-\tilde{p}_{ny} + \tilde{q}_{ny}) \tag{3.8}$$

$$\tilde{m}_x = \sqrt{NR} \frac{\sin(k_x W/2)}{k_x W/2}$$

and $\tilde{p}_{ny}$, $\tilde{q}_{ny}$ are given in (3.6).

Dipoles can also be the constituents of more complex element geometries, Fig. 1.1. The square loop is formed by superposition of four linear dipoles spaced (horizontally and vertically) from the origin of the unit cell. Cross dipoles are formed by superposition of two dipoles, one in the horizontal and one in the vertical direction. Tripoles, finally, consist of three dipoles separated angularly by 120° and connected together at the dipole edges. The basis functions used to compute tripole, cross-dipole and square loop responses are the same ones used with dipoles. The Floquet transforms in the case of the square loops are shifted in both x and y directions by $e^{\pm jk_x|L-W|/2}$ and $e^{\pm jk_y|L-W|/2}$ respectively. In the case of the tripoles the transforms take into account the rotation of the dipoles. These transforms can be found in [7].

A thorough investigation has been carried out on the effect of the element geometry as well the lattice periodicities on the array response. In order to optimise the PRS, a parametric study has been carried out by changing the dimensions of different elements as well as the lattice geometries. The objective is a slow variation of the reflection/transmission response with frequency both in magnitude and phase. A phase increasing with frequency, which is the optimal case, could not be achieved with a single layer array. This is a general conclusion, valid for all of the possible element geometries that have been researched thus far. Upon scrutiny, it was found that dipoles and square patches could exhibit a wider area of partial reflection with a slow variation with frequency. This is achieved with close packing of the elements in the array. In addition, dipoles can be further packed together in one direction thus producing slower variation with frequency as well as avoiding grating lobes that will appear in the radiation patterns of the antenna. Using cross-dipoles, tripoles and square-loops this slow variation was not found, even if the elements were packed closely together.

A comparison of different element responses is shown in Fig. 3.8. The dipoles, square patches and square loops were very closely spaced. Cross dipoles cannot be very closely packed due to their geometry. Tripoles have been arranged in a triangular lattice in order to decrease the spacing as much as possible. The dimensions of the different element unit cells are as follows: Tripoles: $L = 5$ mm, $W = 0.5$ mm, $D_u = D_v = 6$ mm, triangular lattice with $\alpha = 60^0$ and $\alpha_l = 0^0$; Square loops: $L = 4.5$ mm, $W = 0.5$ mm, $D = 5$ mm, square lattice; Dipoles: $L = 14$ mm, $W = 0.5$ mm, $D_x = 1$ mm, $D_y = 14.5$ mm, rectangular lattice; Square patches: $L = 12.5$, $D = 13$ mm, square lattice. Five basis functions have been used for the dipoles along with 13×13 Floquet modes, five bases on each dipole in the square loop along with 17×17 Floquet modes and three basis functions on each of the tripole arms with 13×13 Floquet modes. The square patch was simulated according to section 3.2.1. The arrays in the test were all free-standing. A good relative convergence was achieved for all of the above elements.

According to Eqn. (2.17) for a high gain antenna performance, high reflection values are required, which corresponds to low transmission coefficient values (less than –5 dB). The response of the dipole array, for low transmission values, is closer to the optimum conditions for high-gain and wide bandwidth antenna performance. Therefore, dipoles were chosen to be the preferred element for the PRS in this study.

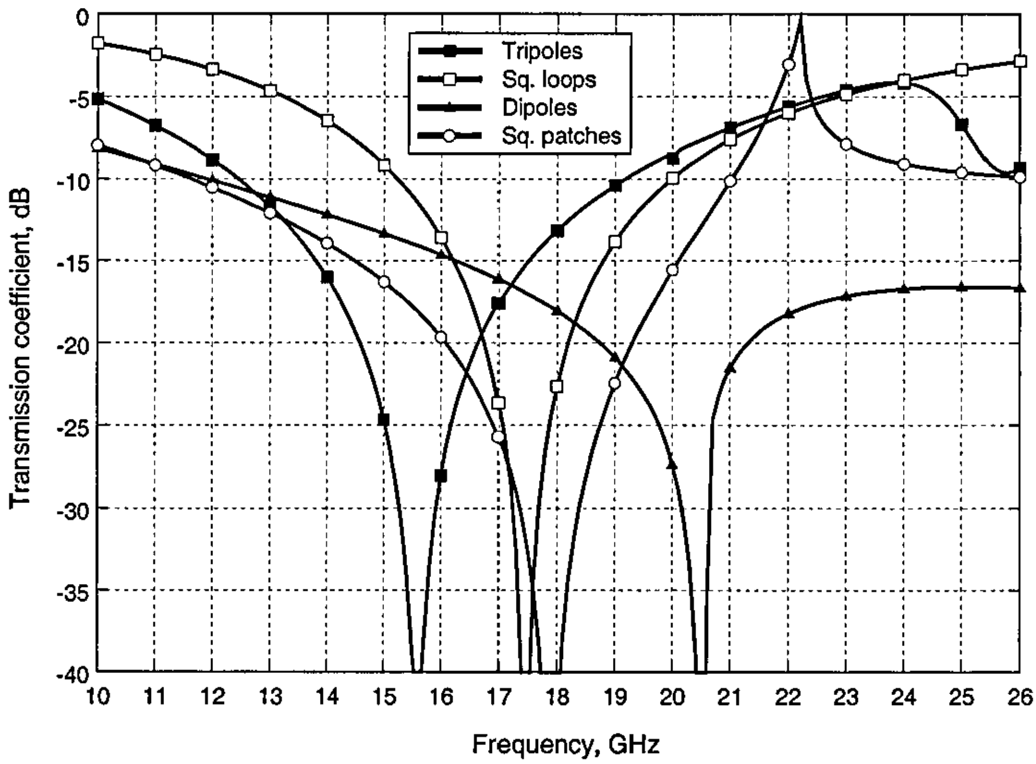

Figure 3.8 Transmission response of several closely spaced conducting elements (free-standing), see Fig. 1.1.

For a design frequency near 15 GHz the following dipole and unit cell dimensions were used: L = 14 mm, W = 0.5 mm, D_y = 14.5 mm, and D_x = 1 mm. The measured transmission coefficient of the dipole PRS (D1), was obtained from a 20×20 cm^2 sheet surrounded by absorbing materiel. The measured and simulation results are shown in Fig. 3.9. The dipoles were made of copper printed on a 32μm thick polyester substrate of dielectric constant 3. They were mounted on a flat polystyrene foamboard ($\varepsilon_r \approx 1.05$) of thickness about 1cm. A more rigid expanded frame was attached to the foamboard to keep it flat.

In order to demonstrate the difference with a non optimised PRS, with regard to the frequency variation, we show the simulated transmission coefficient of a free standing dipole PRS of a larger periodicity (D2). The dipole dimensions are $L = 11$ mm, $W = 0.5$ mm and the periodicity is $D_y = 14$ mm, and $D_x = 6$ mm. Fig. 3.10 shows the reflection coefficient (magnitude and phase) of both PRSs. It can be seen that D2-PRS exhibits a greater variation of the spectral transmission/reflection response near the antenna design frequency (depicted within circles), when compared to the optimised D1-PRS. The optimum phase calculated from Eqn. (2.22) is also shown in Fig. 3.10. The reflection magnitude of the optimised PRS is nearly constant with frequency near 15GHz. The reflection phase, although not the optimum, is closer to the desired one as compared to the reflection phase of D2. It is worth noting that there is a region of constant amplitude and phase increase at 24 GHz. This is in the grating lobe region and was discarded due to low reflectivity (low gain) and complexities that may arise in the radiation patterns of the antenna.

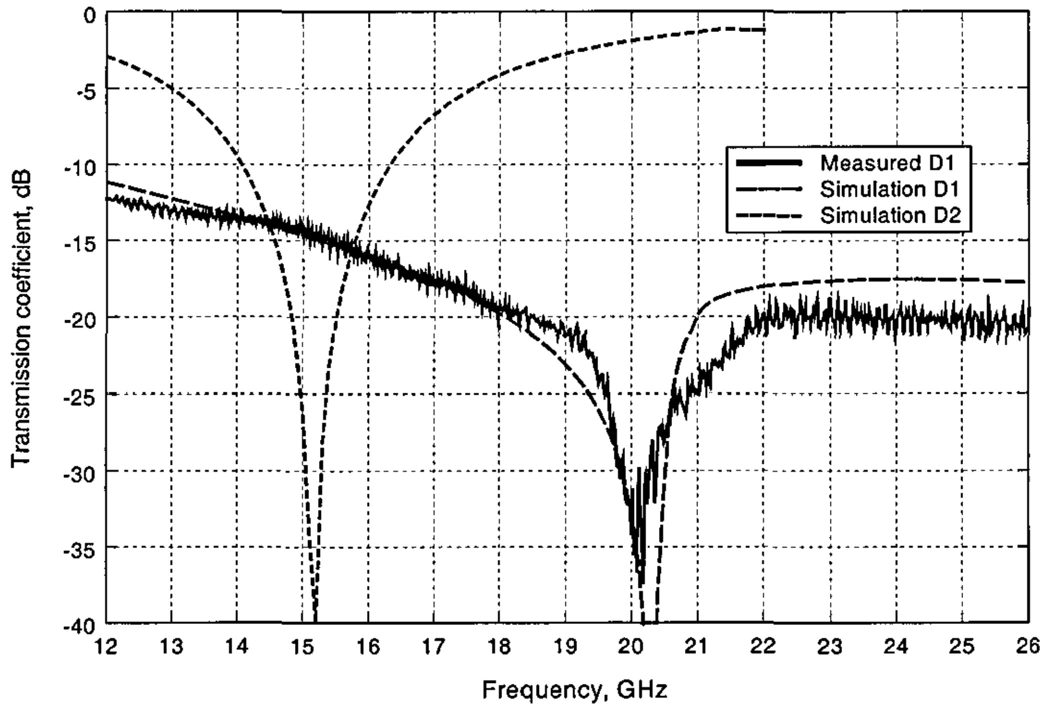

Figure 3.9 Transmission coefficient of dipole PRSs

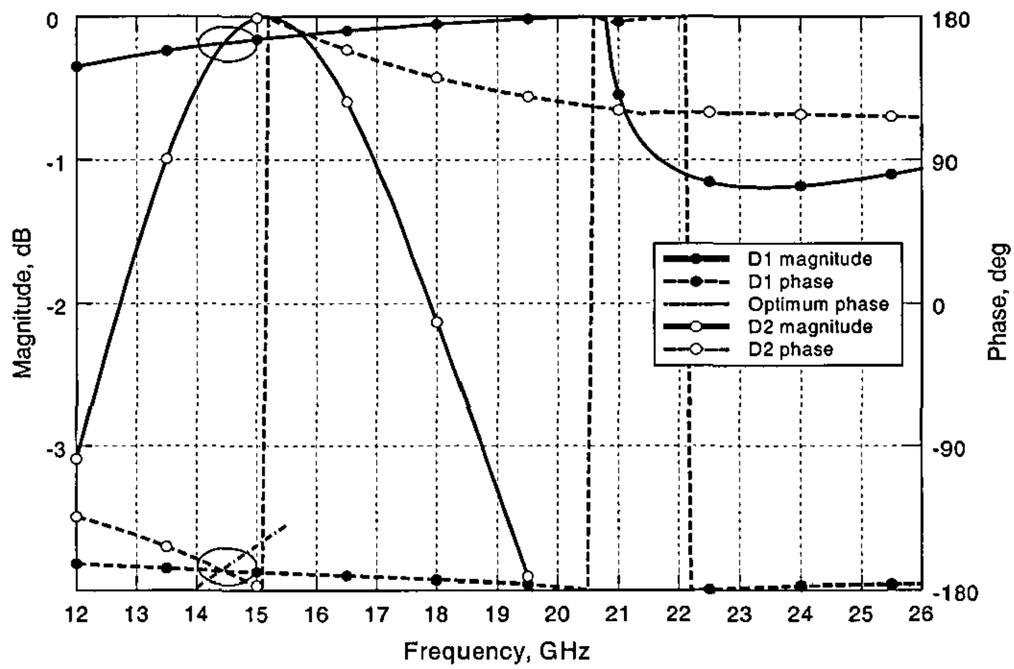

Figure 3.10 Simulated reflection coefficient of dipole PRSs and optimum phase

3.4 Antenna Performance

A planar leaky-wave antenna is formed in accordance to the configuration shown in Fig. 2.1, in chapter 2. An exploded view of the antenna is shown in Fig. 3.11. The antenna performance using both dipole PRSs is presented here. Gain and bandwidth comparisons are made using the approximate ray analysis as well as full wave simulation methods. Measurements of the antenna formed with the optimised PRS are presented. An experimental investigation has also been carried out with regard to the optimum aperture size for maximum antenna efficiency.

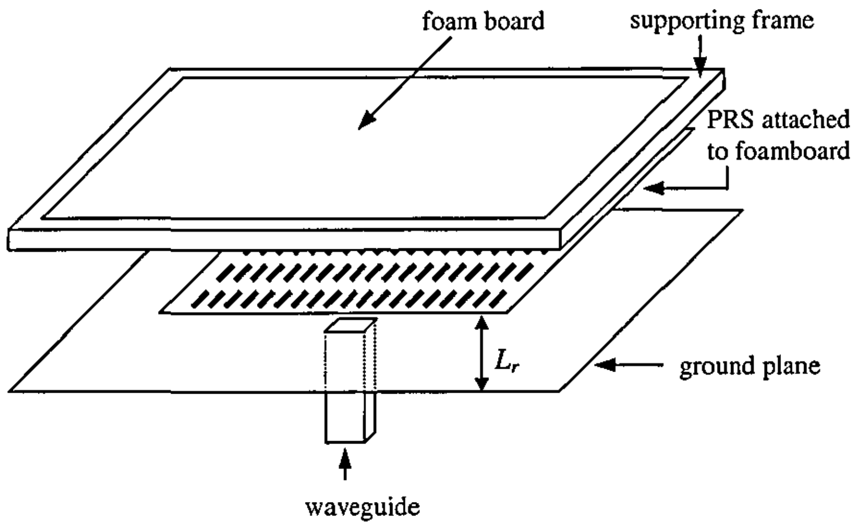

Figure 3.11 Exploded view of the planar leaky-wave antenna

3.4.1 Simulations

In the first stage, the ray analysis is implemented, assuming that the array and the antenna are of infinite extent. At 14.45GHz the magnitude of the reflection coefficient for both PRSs (D1 and D2) is R = 0.979. The phase values at this frequency are also the same, hence the resonant distance is L_r = 10.76 mm (according to Eqn. 2.13), for both PRSs. The overall gain is shown in Fig. 3.12. This gain is the sum of the relative gain estimated from Eqn. (2.12) and the measured gain of the grounded waveguide. The same figure also shows the gain estimation for a frequency independent surface (fictitious), which has the same reflection coefficient values as the ones of the dipole PRSs at 14.45 GHz. It can be seen that the bandwidth of the optimised D1-PRS is wider than the one of D2-PRS and closer to the one obtained from a frequency independent surface. The latter is indicative to the improvement of the antenna performance that can be attained.

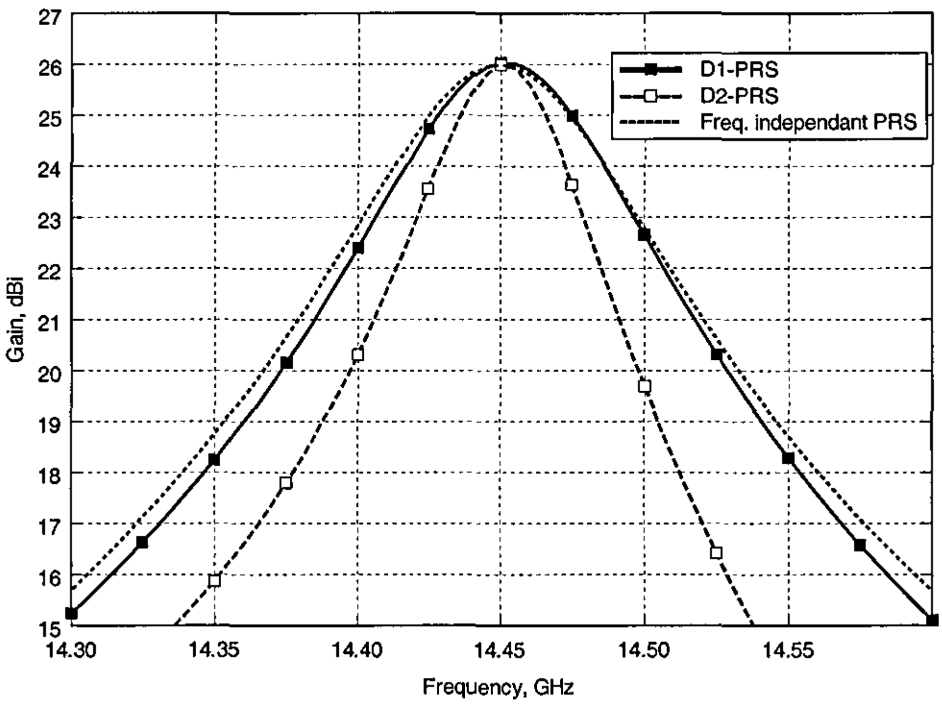

Figure 3.12 Gain of antenna estimated from ray analysis (Eqn. 2.12)

A more rigorous analysis of the antenna, which takes into account the finite size of the PRS, has been carried out in Ensemble. The size of the PRS, is now restricted to 10×10 cm^2, due to computational recourse limitations. However, the ground plane is still considered to be of infinite size. In order to include the waveguide in Ensemble, a plane wave incidence was used to simulate a rectangular aperture (15.8×7.9 mm^2) in the infinite ground plane. Although infinitesimal thickness was considered, the field in the aperture was similar to that of a grounded open-ended waveguide. Both D1 and D2 PRSs had a size of 10×10 cm^2 and consisted of 7 rows of dipoles in the y direction. The adaptive meshing technique, available in the package, was used to achieve convergence. The simulation on a 1.2 GHz Athlon PC required 10 hours (280 Mb of memory) and 2.5 hours (155 Mb) for D1-PRS and D2-PRS respectively. The maximum gain obtained with D1-PRS at the resonant distance was 24 dBi, Fig. 3.13, and at a slightly higher frequency (f = 14.6 GHz) than the one predicted (14.45 GHz) from the approximate analysis. D2-PRS gave a gain of 22.6 dBi at the same frequency at a slightly smaller resonant distance (10.7 mm). The 3 dB bandwidth of the optimised PRS was nearly double (1.3%) that of D2. Decreasing the resonant distance for D2-PRS, the maximum gain increases and appears at a higher frequency (e.g. 23 dB at 14.75 GHz for L_r = 10.5 mm), but at the expense of the bandwidth decrease. This trend can also be predicted from the approximate ray theory. However, the gain does not reach that of the optimised D1-PRS. In contrast, small changes of the resonant distance have little effect on the gain and bandwidth of D1. This can be explained by the small dependancy of its reflection characteristics with frequency.

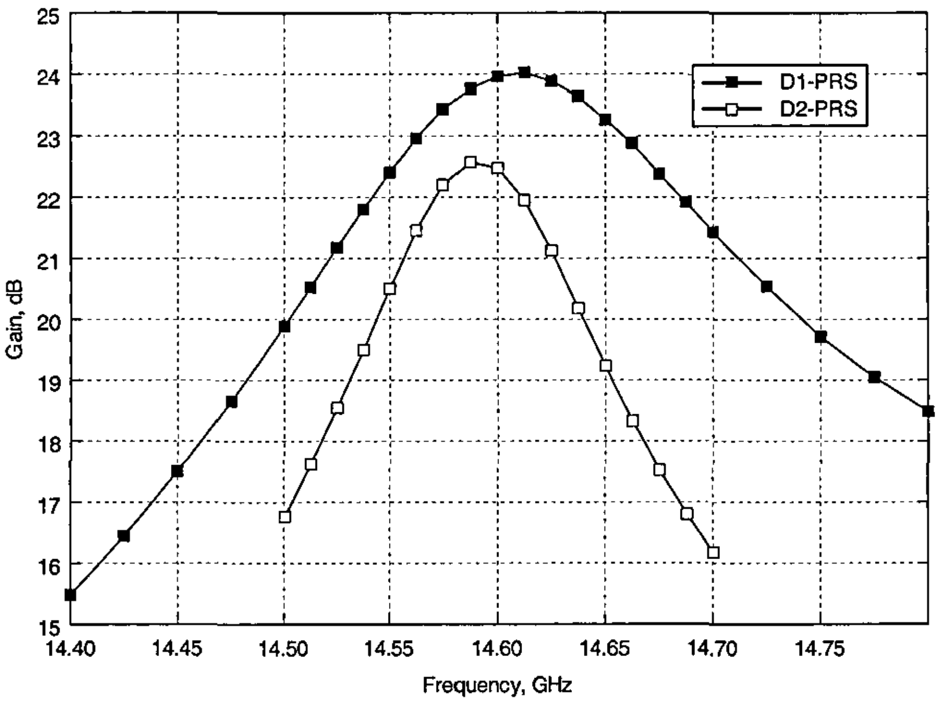

Figure 3.13 Gain of antenna with $10 \times 10\,\mathrm{cm}^2$ D1 and D2 PRSs, using ENSEMBLE

3.4.2 Antenna with 10×10 cm^2 optimised PRS

A dipole PRS of size 10×10 cm^2 was placed at a resonant distance of about 11 mm over the primary antenna, which consisted of an open-ended J-band waveguide in a 30×30 cm^2 ground plane (Fig. 3.11). Four plastic screws were used to support the frame of the PRS over the ground plane. It should be noted that the accuracy of measurement of the resonant distance is restricted to ±0.5 mm, due to the non perfect flatness of the foamboard boards as well as alignment errors. This would result in a frequency deviation of more than 0.5 GHz, as it can be estimated from Eqn. (2.13) by simple differentiation.

For comparison with the measurements, as well as Ensemble, we have also used a parallelised 3-D FDTD package (LC). For the latter, due to memory restrictions, the size of the ground plane was reduced to 20×20 cm^2 with a thickness of 1mm. The size of the computational space was $21.5\times21.5\times3.35$ cm^3. A uniform lattice composed of $430\times430\times67$ cubic cells of size 0.5mm ($\approx\lambda_0/40$) was used. This resolution allows the modelling of the PRS geometry with 0.5 mm dipole widths. The waveguide inner aperture area was 16×8 mm^2. The waveguide was excited by a Gaussian current source spaced at $\lambda_0/4$ from the back short. The resonant distance was fixed at 11 mm and the PRS screen was modelled using infinitesimal thickness. An eight-layer second order Berenger's PML absorbing boundary condition was used on all sides of the lattice spaced 15 cells from the closest surface of the antenna. 20,000 time steps were required to reach convergence. The simulation required 1.37 Gb of memory and it took 20 hours on an 8-processor Cray J90.

Figure 3.14 shows the measured and simulated results of the antenna gain against frequency. The maximum gain is 21.9 dBi at 14.275 GHz. The 3 dB bandwidth is 1.2% and the antenna efficiency is 54 % . The return loss is better than 30 dB near the resonant frequency. The FDTD simulation produced a gain close to the measured one. Ensemble produced a higher gain, and there was also a small frequency deviation of the gain maximum. This can be partly explained by the plane wave model approximation for the simulation of the field in the waveguide aperture, and also by the infinite ground plane used in the model.

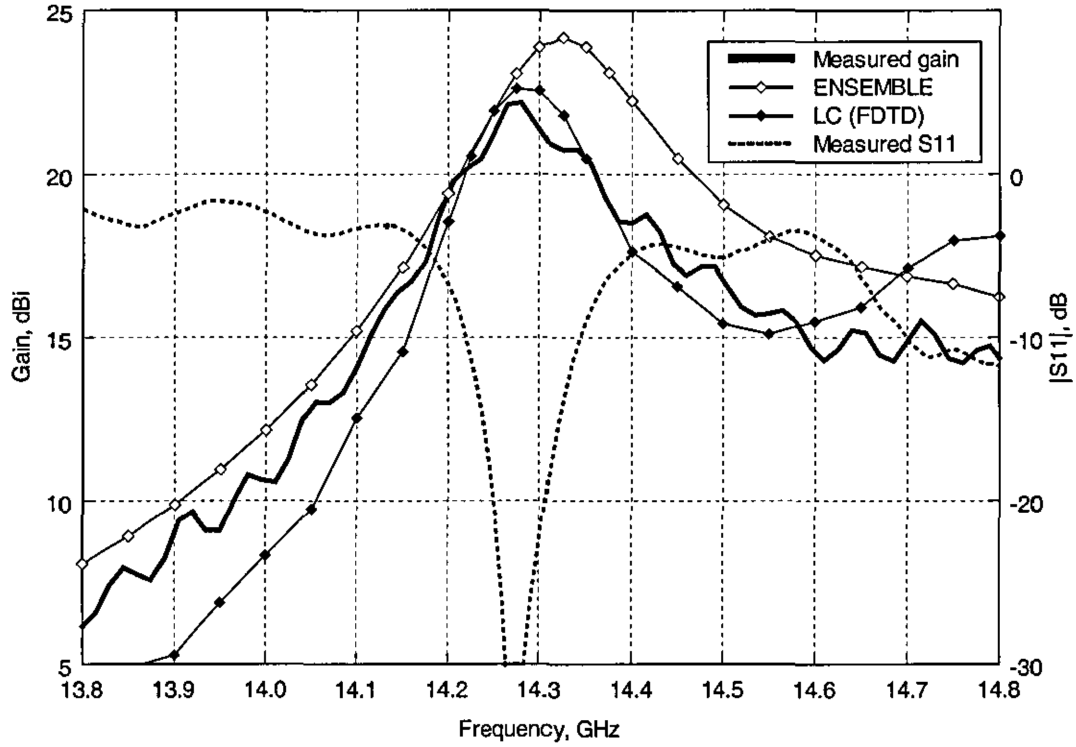

Figure 3.14 Gain and S_{11} of antenna with $10\times10\,cm^2$ optimised PRS

Currents and radiation patterns

Using Ensemble, the total current (magnitude of current vector) on the dipoles of the PRS at 14.32 GHz and well before that (14 GHz) was obtained and it is shown in Fig. 3.15. As expected, the average current on the PRS is maximum at the resonant frequency (14.32 GHz), where the energy spreads and hence, a larger area of the PRS is excited. It can be seen that the currents form rows along x and maxima occur not on the central row but on the adjacent ones. At the end of each row the current diminishes. The edge effects are better demonstrated in Fig. 3.16, which shows the near field distribution (total field) at resonance. The image depicts an area of 16×16 cm^2 at 0.1mm in front of the PRS which is shown as a dotted-line box. High fields appear just outside the PRS's vertical edges.

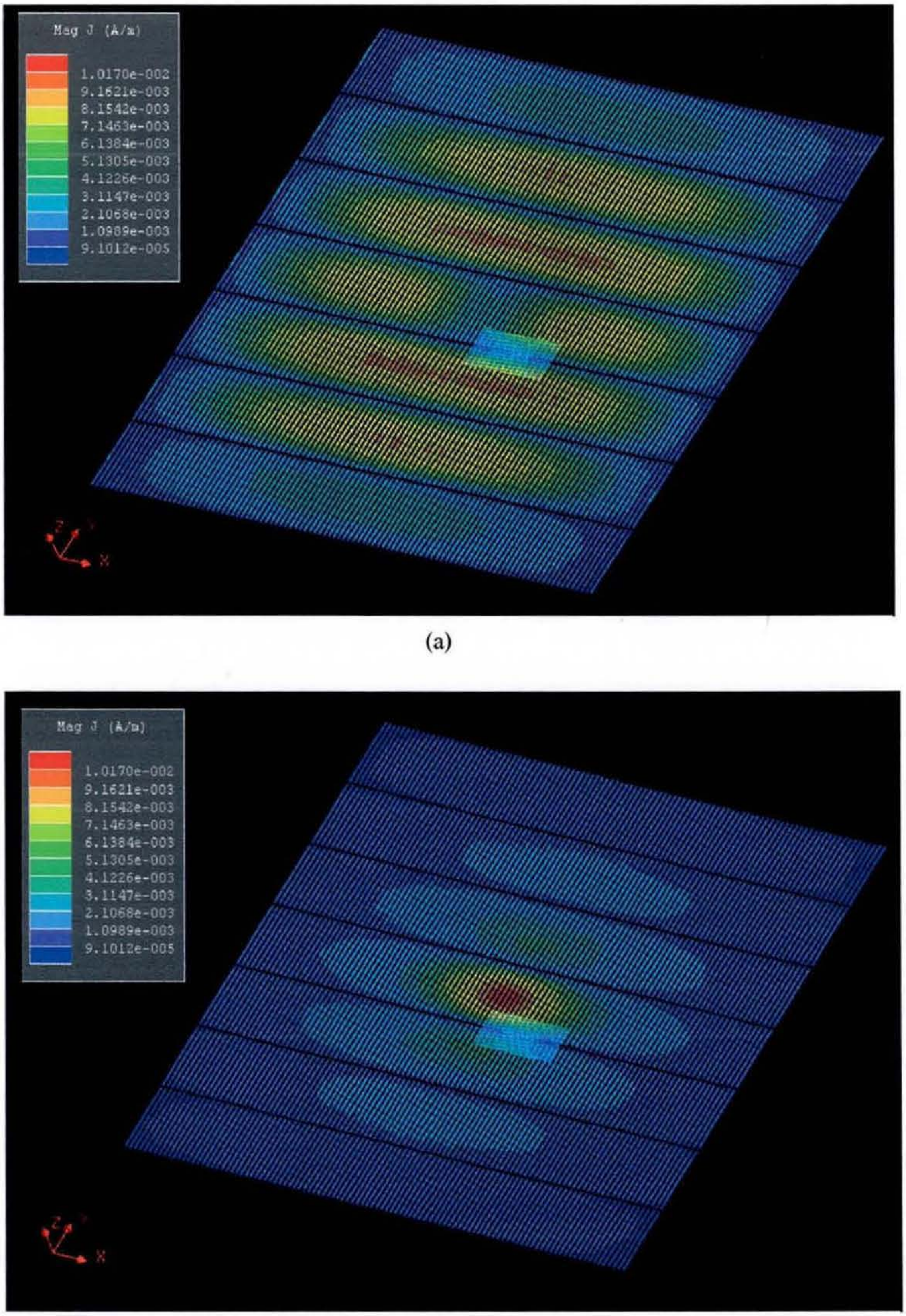

(a)

(b)

Figure 3.15 Total current density on optimised PRS dipoles: (a) at resonant frequency; (b) at 14 GHz

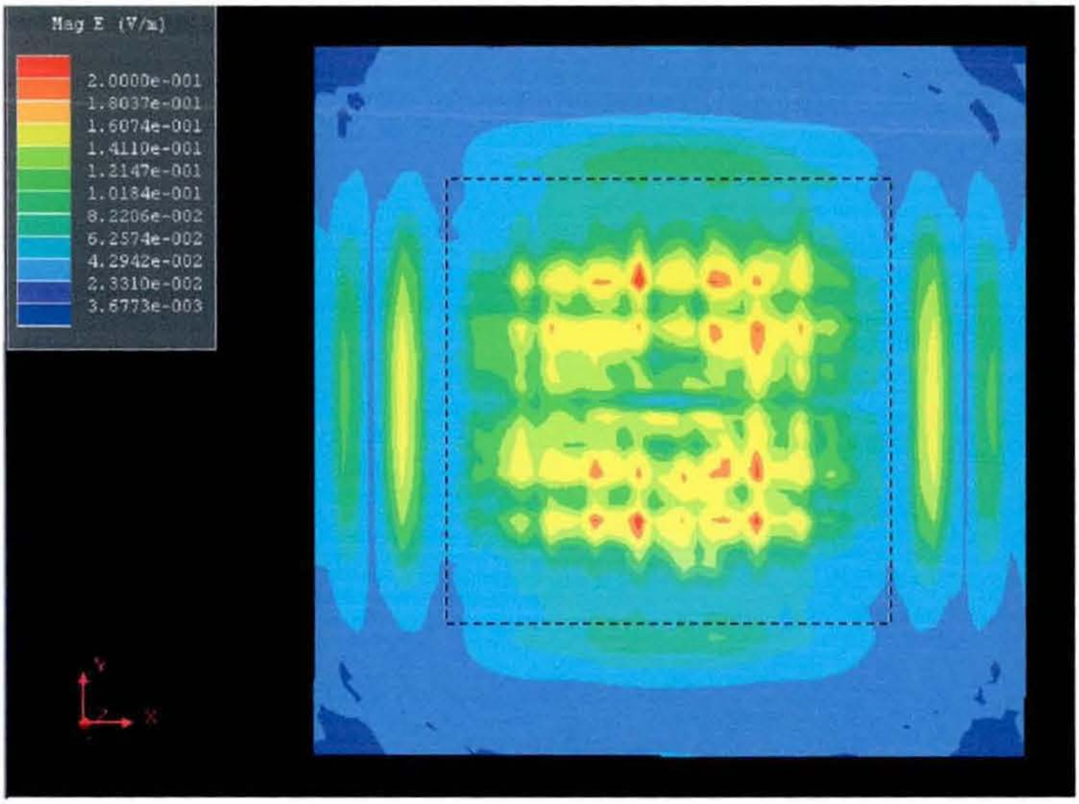

Figure 3.16 Near field distribution of antenna with optimised PRS

The radiation patterns are shown in Fig. 3.17. The sidelobe level remains below –15 dB in H-plane and below –19 dB in E-plane. The higher sidelobes in H-plane can be explained by the diffraction effects due to the small PRS size (see near fields in Fig. 3.16). Both simulations are in good agreement with measurements. Ensemble gives lower sidelobes because of the infinite ground plane. FDTD results have a little higher sidelobes and slightly narrower beam. Cross polarisation levels were below -30 dB in both planes.

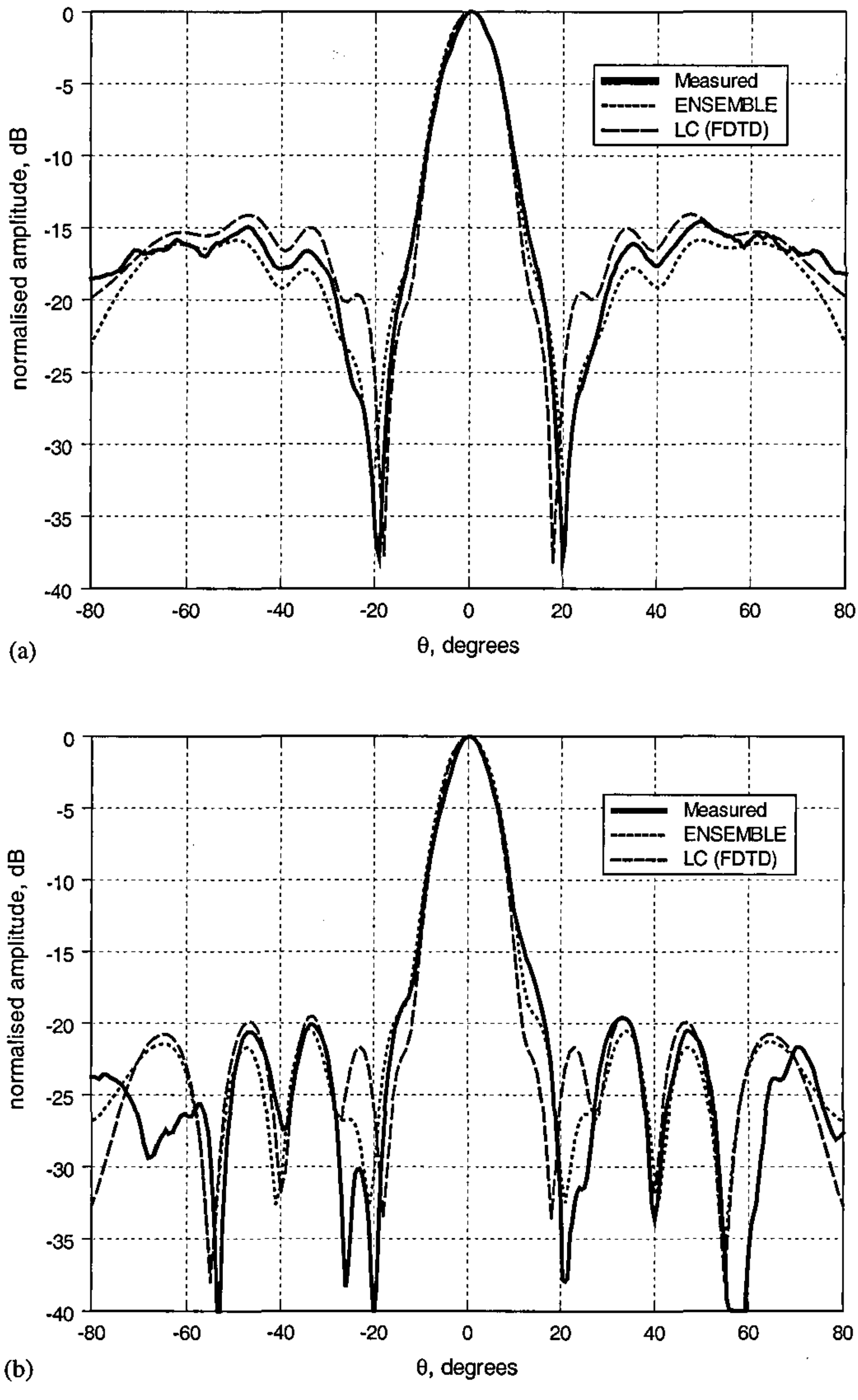

Figure 3.17 Simulated and measured radiation patterns of antenna with $10\times10\,\text{cm}^2$ optimised PRS at resonant frequency: (a) H-plane; (b) E-plane

3.4.3 Antenna with 20×20 cm^2 optimised PRS

A 20×20 cm^2 optimised dipole PRS has also been used to form the antenna. The PRS was placed at a resonant distance of about 10.8 mm over the ground plane. The measured gain and return loss, are shown in Fig. 3.18. Due to the large PRS size, the ray analysis can be used to predict approximately the antenna gain and radiation patterns. Full wave simulations for this size would be very computationally demanding. The maximum gain obtained is 22.5 dBi at 14.45 GHz. The efficiency of the antenna is relatively low, 15.5%. The radiation patterns, at the resonant frequency (14.45 GHz), exhibit a quite low sidelobe level (SLL), shown in Fig. 3.19. Low SLL of -30 dB was obtained in H-plane and less than –17 dB in the E-plane. The approximate analysis predicts well the main lobe in the patterns. It also predicts with satisfactory agreement the first and last sidelobes in the E-plane, which are due to the grating response of the array (grating lobes). However, further sidelobes with lower values in both planes have not been predicted. These are mainly caused by diffraction effects, which are not taken into account in the ray analysis and are not significant due to the large size of the PRS.

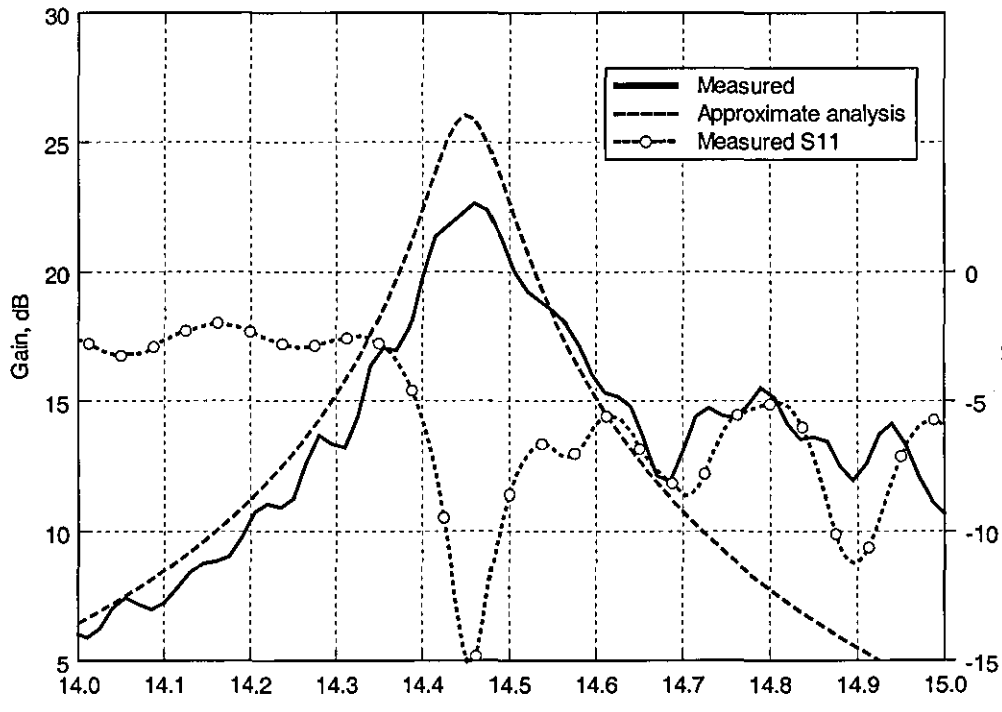

Figure 3.18 Gain and S_{11} of antenna with $20\times20\,cm^2$ optimised PRS

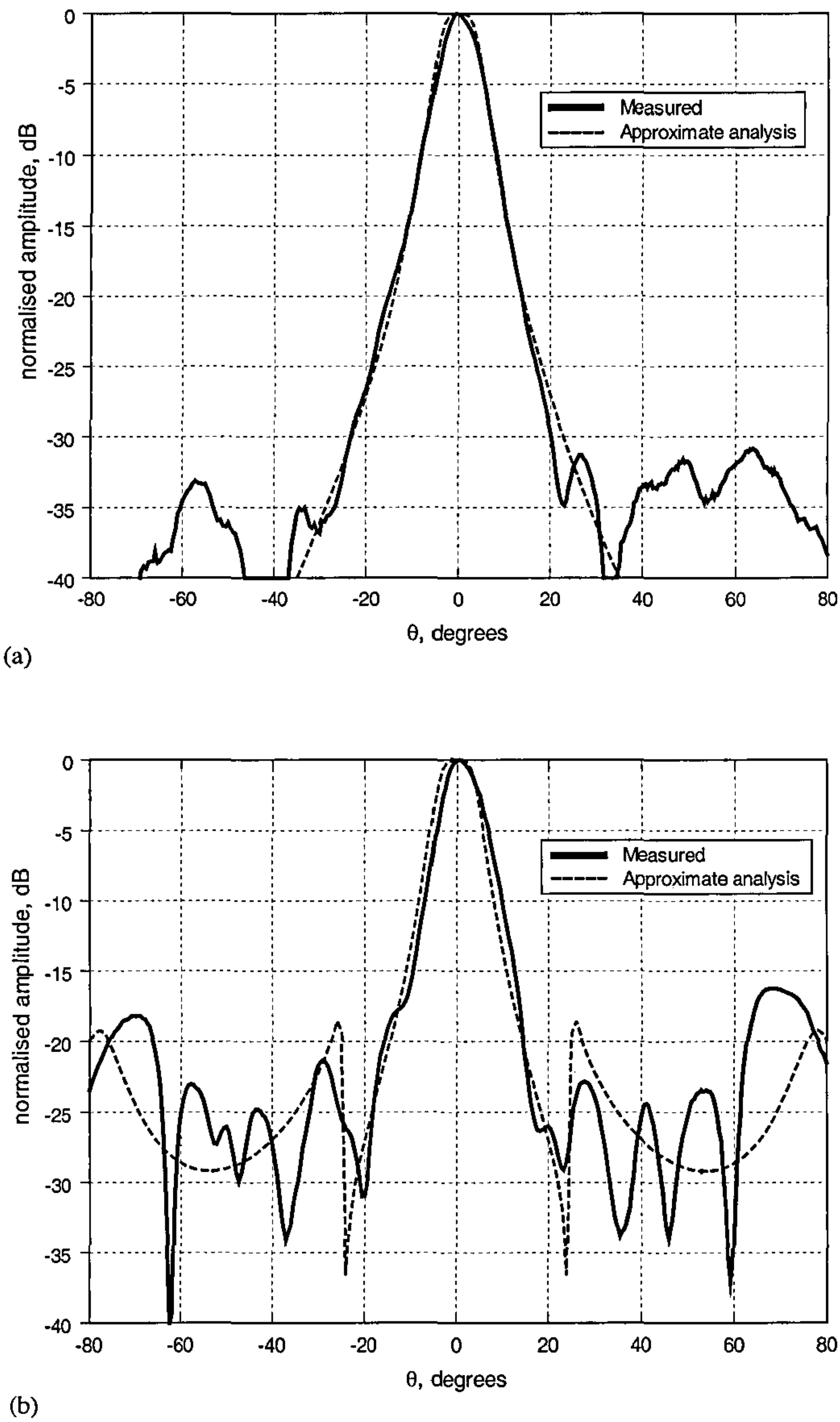

Figure 3.19 Radiation patterns of antenna with $20\times20\,\mathrm{cm}^2$ optimised PRS: (a) H-plane; (b) E-plane

3.4.4 Efficiency test

The effect of the size of the optimised PRS on the antenna efficiency has been investigated experimentally. The overall gain was measured for different PRS sizes and the antenna efficiency was calculated from, [12]:

$$G_{meas} = (\frac{4\pi A}{\lambda_0^2})e, \qquad e = e_{ap}e_m \tag{3.9}$$

where e_{ap} is the aperture efficiency, e_m the mismatch efficiency and A the aperture size.

The 20×20 cm^2 optimised PRS was initially used. As the PRS was cut into smaller square sheets, the overall gain decreased slightly, resulting in an increase of the efficiency of the antenna. This shows that very little energy reaches the ends of large size PRSs. Maximum efficiency was obtained for the 10×10 cm^2 PRS. For PRSs of side smaller than 8.6 cm the gain dropped several dBs, giving lower efficiency values. Measurements below 4 cm have diffraction difficulties and the PRS has little effect. Fig. 3.20 shows the antenna efficiency for different PRS sizes. The resonant frequency in each measurement shifted between 14.2 GHz and 14.5 GHz. The error bars indicate the inaccuracies due to the surface flatness and the allignment errors of the PRS.

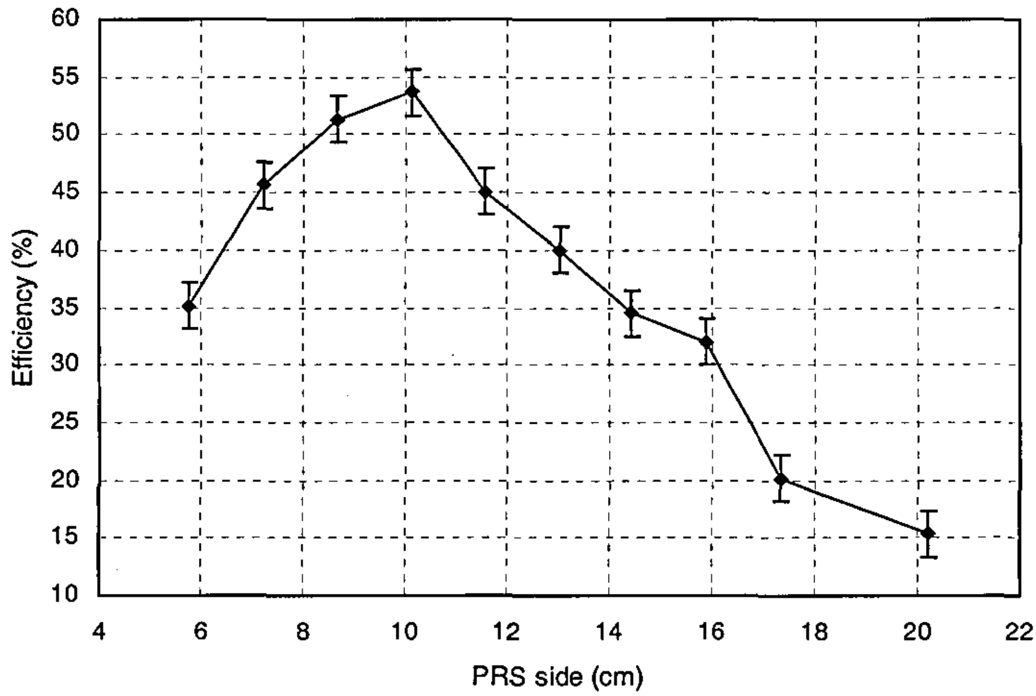

Figure 3.20 Effect of PRS size on antenna efficiency

3.5 Conclusions

An investigation into the beamforming effect of single layer PRS arrays in a leaky-wave antenna configuration has been presented in this chapter. A theoretical model of the antenna has been implemented, based on ray optics and a modal calculation of the PRS frequency and angular reflection response. The model predicted the gain and radiation patterns of leaky-wave antennas with large size ($\approx 10\lambda$) PRSs with a satisfactory accuracy. Subsequently, the phase and magnitude of the reflection coefficient of the PRS have been studied with regard to the effect on the antenna gain and bandwidth and the PRS has been optimised to a certain extent. The optimisation was verified for small PRS size using full-wave simulations of the antenna, whereby the edge effects were taken into account. For this purpose Ensemble has been used and the results were in a satisfactory agreement with measurements. It also provided the surface currents and near field of the antenna. Better simulation results were obtained with a 3D-FDTD simulation of the antenna in LC. However, the package was not fully developed and further results such as currents and fields could not be obtained. A high gain of 22 dBi has been obtained with a 10×10 cm^2 optimised dipole PRS. This was also found to be the optimum PRS size for maximum antenna efficiency, after an experimental study.

References

[1] TRENTINI, G. V. : 'Partially reflecting sheet arrays', *IRE Trans. Antennas Propag.*, vol. **AP-4**, 1956, pp. 666-671

[2] JAMES, J. R., KINANY, S.J.A., PEEL, P.D., and ANDRASIC, G.: 'Leaky-wave multiple dichroic beamformers," *Electron. Lett.*, 1989, **25**, pp. 1209-1211

[3] LEE, S. W., ZARRILLO, G. and LAW, C. K. : 'Simple formulas for transmission through periodic metal grids or plates', *IEEE Trans. Antennas Propagat.*, vol. AP-30, 1982, pp. 904-909.

[4] COX, G.J., FERESIDIS, A. and VARDAXOGLOU, J.C. : 'Leaky Wave Action of Planar and Cylindrical FSS', Proc. PREP 2000, 2nd Conference on Postgraduate Research in Electronics, Photonics and Related Fields, IEE, University of Nottingham, April 2000, pp. 273-278.

[5] FERESIDIS, A. and VARDAXOGLOU, J.C.: 'Flat plate millimetre wave antenna based on partially reflective FSS', Proc. IEE 11th International Conference on Antennas and Propag., ICAP, April 2001, Manchester, UK, pp. 33-36

[6] CHADRAN, S. and VARDAXOGLOU, J. C. : 'Performance of two single-layer frequency-selective surfaces as spatial filters', *Microwave Opt. Technol. Lett.*, vol. 6, pp. 339-342, May 1993.

[7] VARDAXOGLOU, J. C. : 'Frequency Selective Surfaces: Analysis and Design', Research Studies Press, Somerset, England, 1997

[8] MITTRA, R., CHAN, C. H. and CWIK, T. : 'Techniques for analyzing frequency selective surfaces – A review', *Proc. IEEE*, vol. 76, no 12, 1988, pp. 1593-1615

[9] ABRAMOWITZ, S. and STEGUN, A. : 'Handbook of mathematical functions', Dover Publications Inc., New York, 1965.

[10] COLIN, M. : 'The beamforming action of planar periodic arrays', M.Phil. thesis, Loughborough University, April 1991

[11] FERESIDIS, A. P. and VARDAXOGLOU, J. C. : 'High gain planar antenna using optimised partially reflective surfaces', *IEE Proc., Microw., Antennas & Propag.*, vol. 148, No. 6, Dec. 2001, pp. 345-350

[12] BALANIS, C. A. : 'Antenna theory : analysis and design', John Wiley & Sons Inc., New York, 1982

Chapter 4

Double Layer PRSs

4.1 Introduction

In this section double layer arrays are investigated for their use as PRSs in the leaky-wave antenna design. The high-gain and wideband leaky-wave antenna requirements presented in Chapter 2 are used as objectives in the design of double layer PRSs. A parametric study is carried out in section 4.2, using a plane wave modal analysis, in order to study the variation of magnitude and phase of the reflection coefficient of double layer dipole arrays. The study leads to the identification of a characteristic response of double layer arrays, which is very similar to the optimum PRS features for high gain and wide-band antenna performance. In particular, a reflection phase response increasing with frequency is obtained by using arrays with different element dimensions separated by about half wavelength.

In section 4.3 an optimised double layer dipole PRS design is produced and is used to form a leaky-wave antenna, yielding high gain and broad bandwidth. In the following sections, a slot feed is designed in order to improve the return loss of the antenna. A double layer square patch array is produced in a rigid structure and it is used to produce a broadband leaky-wave antenna prototype which includes the new feeder. The antenna in its entirety has been simulated using 3D time domain codes. LC has been used for a simulation of the antenna with the double layer dipole array and it was executed on a Cray machine. In the design of the feeder as well as the antenna with the double layer square patch PRS, a newly obtained package, Microstripes, has been used. Microstripes provided more advanced modelling capabilities, such as non-uniform meshes, symmetry conditions (electric and magnetic walls) and automatic return loss calculation. All these features resulted in a significant reduction in computer memory requirements. Furthermore the code was executed on a PC, which was more easily accessible than the Cray computer.

4.2 Optimisation of Double Layer PRS for Gain and Bandwidth

As discussed in the previous chapter a "conventional" single layer planar array under plane wave illumination cannot exhibit a reflection response such that the reflection phase values would increase with frequency (before the grating lobes region). This is an important requirement for a wideband leaky-wave antenna performance, which is often required in modern communication systems. Double layer arrays are investigated in this section for further bandwidth enhancement of planar leaky wave antennas. The reflection magnitude and more critically, the reflection phase variation (with frequency) of double layer dipole arrays are studied. A parametric study is carried out by changing the element dimensions and the separation distance of the two layers. In the course of the study it has been discovered that a double layer structure could be used in such a way that an extra resonance would appear in the array response and the reflection phase would increase almost linearly with frequency in a certain frequency range. As it is shown in section 4.2.2, in order to achieve that, the two arrays must exhibit different reflectivity values and the separation distance should be about half wavelength.

4.2.1 Array interference null

In a double layer array structure, apart from the individual array resonances, additional resonances are produced by the interference of the two surfaces. These resonances are more evident when the array separation is in the range of half a wavelength. They appear as nulls (sharp notches with a minimum value of zero) in the reflection response of the array or sharp peaks (with a maximum value of one) in the transmission response. In the bibliography they are referred to as "array interference nulls" [1]. The two arrays, separated by about half wavelength, form a resonant cavity, similar to the resonant optical cavity (used for example in Fabry-Perot interferometers), [2], and in the same way that the array forms a resonant cavity with the ground plane in the leaky-wave antenna configuration (see sections 2.2 and 2.3).

The spectral position and reflection values of the array interference nulls in double layer structures, can be estimated using the resonant cavity (or Fabry-Perot) approach, and simple formulas can be derived and used to predict approximately the array response. These formulas are produced by considering uniform plane waves in the area between the two layers and describe the dominant mode coupling between the two arrays. Following a ray tracing approach, an approximate formula for the transmission coefficient of a double layer structure under plane wave illumination can be derived ([2], pp.129-130 and section 2.3). The arrays are assumed to be free-standing and separated by an air gap of distance S. The maximum value of the power transmission coefficient occurs when the cavity is in resonance and is given by:

$$T^{p}_{\max} = \frac{(1-R_1)^2(1-R_2)^2}{\left(1-R_1 R_2\right)^2} \tag{4.1}$$

where R is the voltage reflection coefficient. Another useful equation derived in [2] is the one giving the Q of the cavity, which is a measure of the sharpness of the cavity resonance:

$$Q = \frac{2\pi S}{\lambda}\frac{\sqrt{R_1 R_2}}{1-R_1 R_2} \tag{4.2}$$

If the two surfaces are identical such that $R_1 = R_2 = R$, then $T^p_{\max} = 1$, as obtained from Eqn. (4.1). Otherwise, the more R_1 differs from R_2 the smaller the transmission coefficient becomes. In addition, as seen from Eqn. (4.2), the higher the reflection value R of the surfaces, the sharper is the resonance. The formulas derived above are only approximate and have been used in order to obtain an insight into the resonant cavity nature of double layer structures. Initial estimates of the maximum transmission (minimum reflection) and the sharpness of the array interference null have been obtained.

The plane wave modal analysis based on Floquet theorem is used to compute accurately the transmission/reflection response of double layer arrays [3]. The trends predicted in Eqns. (4.1) and (4.2) are verified as it is shown later on. Furthermore, using the modal analysis, the phase response of the double-layer array can be computed and examined.

We consider the unit cell geometry of the optimised dipole array of section 3.3. Dielectric substrate is taken as air. A double layer structure is formed by placing two identical arrays in parallel to each other (Fig. 2.9), with separation distance, S, in the range of half wavelength for a design frequency near 15 GHz. Five sinusoidal basis functions (see section 3.3) have been used to expand the current on the unit dipole of each array, i.e. ten basis functions in total. Good relative convergence has been achieved with 289 Floquet modes. The transmission and reflection coefficients are shown in Fig. 4.1, for different separation distances S. The main resonance of the array, due to the dipoles, is just above 20 GHz, as in the single-layer dipole array. This resonance remains at the same frequency and is not affected by the separation distance. Grating lobes appear at frequencies above the resonance because of the array periodicity in the y-axis. The array interference nulls appear at around 4 GHz and 15 GHz. Their position in the frequency spectrum is determined by the separation distance. In fact, the separation distance is not exactly equal to half wavelength, but it differs because of the additional phase shifts introduced by the individual arrays.

The effect of the separation distance on the shape of the null (or the peak in transmission) is better shown in the transmission response, Fig. 4.1(a). The maximum value of the peak is one, as expected from Eqn. (4.1). As S increases, the peak moves towards lower frequencies (higher wavelength). Furthermore, the peak becomes less sharp, as expected from Eqn. (4.2) due to the lower reflectivity values of the individual dipole array in lower frequencies (refer to Figs. 3.8 and 3.9, section 3.3).

The specific array geometry has been chosen because of its high reflectivity values as well as the slow variation of its reflection/transmission response with frequency. The high reflectivity will provide a sharp reflection null (or transmission peak) whereas lower reflectivity screens would yield lower reflection values on either side of the null and wide transmission peaks, as the one at 4 GHz in Fig. 4.1. The slow variation with frequency is needed in order to allow for a degree of freedom in the design of the peak, by changing the separation distance and thus moving the peak in frequency.

An important feature in the double layer array response, is the phase of the reflection coefficient. This is the feature where the optimisation of the PRS array will be focused on. The reflection phase of the double-layer dipole array is shown in Fig. 4.2 in a [-180, 180] degrees range. As expected, the phase values cross $\pm\pi$ at the main resonance as well as at the extra resonances due to array interference.

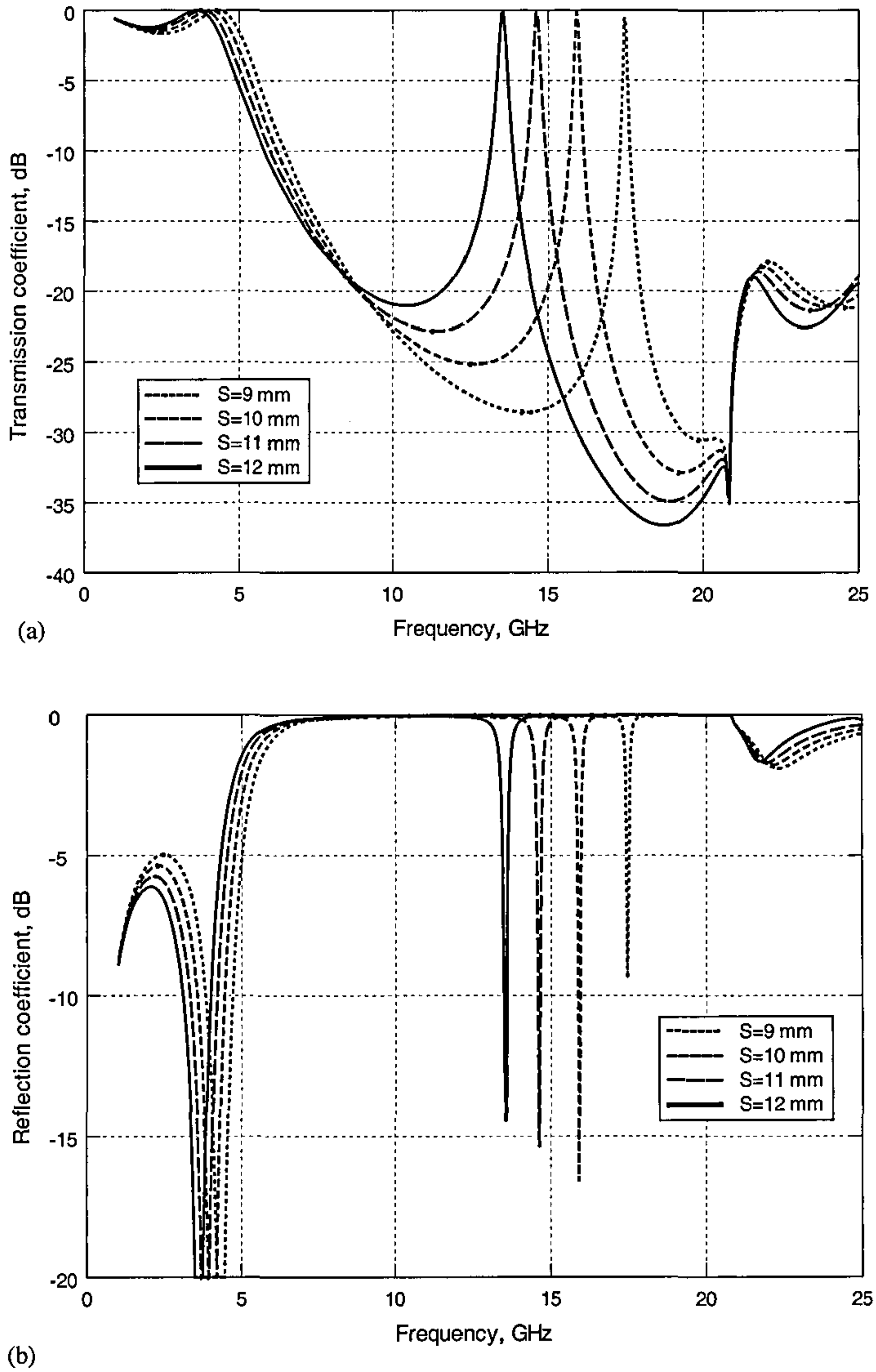

Figure 4.1 Effect of separation distance on the response of double-layer dipole array.

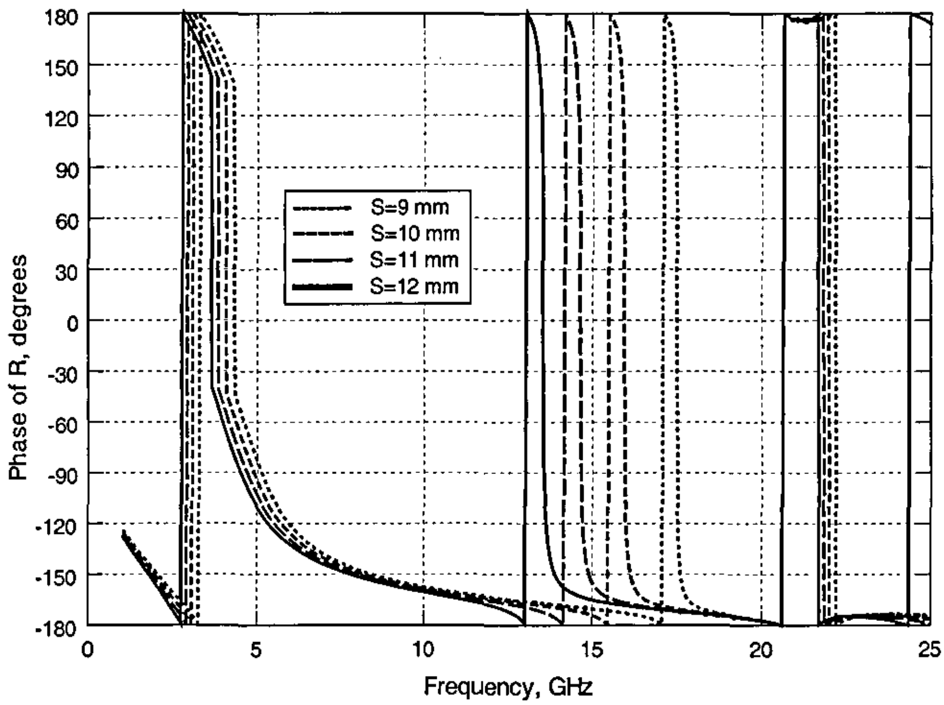

Figure 4.2 Effect of separation distance on phase of reflection coefficient of double-layer array

4.2.2 Phase Optimisation

According to Eqn. (4.1), if an array of lower reflectivity is used as the second layer in the double layer structure of section 4.2.1, it would result in lower values of maximum transmission in the array interference null. This means that the maximum of the peak in the transmission response would be less than one, and correspondingly the minimum reflection values in the null would be larger than zero. Moreover, the peak would be smoother and wider in frequency, according to Eqn. (4.2).

Using the plane wave modal analysis, the effect of the reflectivity of the second layer to the double layer array response (magnitude and phase) has been studied rigorously. The double layer dipole array has been used with a separation distance S=12mm between the two layers. A parametric study has been carried out by changing the length, L_2, of the unit dipole in the second layer, thus changing the reflectivity of the layer. Smaller dipole length, L, in the single layer array, with the same periodicity, results in higher transmission values as shown in Fig. 4.3 (i.e. lower reflection values). The double layer array response for different dipole length in the second layer, L_2, is shown in Fig. 4.4 (transmission coefficient) and Fig.

4.5 (reflection coefficient). For shorter second layer dipole (i.e. lower second layer reflectivity) the null (or transmission peak) becomes smoother and wider. With L_2 decreasing, the maximum transmission value within the peak decreases and correspondingly the minimum reflection value in the null increases. In addition, the array interference null moves towards higher frequencies. The resonance becomes less evident because of the small reflectivity values of the second layer. Thus, one could conclude that a type of semi-resonant effect takes place in the cavity formed by the two layers (semi-resonant cavity).

An investigation on the phase response of the double layer array during the parametric study has revealed a special characteristic, which can be extremely useful for bandwidth enhancement of the leaky-wave antenna structure studied in this thesis. It was discovered that a reflection response with the phase increasing with frequency can be achieved for certain values of L_2. The reflection phase of the double layer dipole array for different values of L_2 is shown in Fig. 4.6. When the second layer is identical ($L_2 = 14\,\text{mm}$) or similar ($L_2 = 12\,\text{mm}$) to the first one the reflection phase crosses the $\pm 180^\circ$ value due to the resonant effect between the two layers. For smaller L_2 (9mm) the resonant effect is weak (semi-resonant cavity) and the reflection phase does not cross the $\pm 180^\circ$ value. As soon as the array interference null starts appearing in the frequency response, the phase starts increasing almost linearly with frequency. After the null, it returns to the normal values of the array phase response. However, this phenomenon happens only for a small range of values of L_2. For smaller dipole length ($L_2 = 7\,\text{mm}$) the second layer is not very reflective and there is almost no resonance, thus the phase values are similar to those of the first layer.

The specific reflection phase response produced for $L_2 = 9\,\text{mm}$, is close to the optimum phase response, presented in section 2.3, for a wideband leaky-wave antenna performance. Moreover, the values of the reflection coefficient magnitude (Fig. 4.5) in the array interference null are quite high, which is needed for a high gain antenna performance. The variation of the magnitude values with frequency is quite small and does not affect the antenna performance significantly. In fact, the reflection magnitude varies between –1.3 dB and -0.9 dB in the frequency range of phase increase. This corresponds to an antenna gain variation of 1.6 dB, as calculated from Eqn. (2.17), assuming that the phase condition holds.

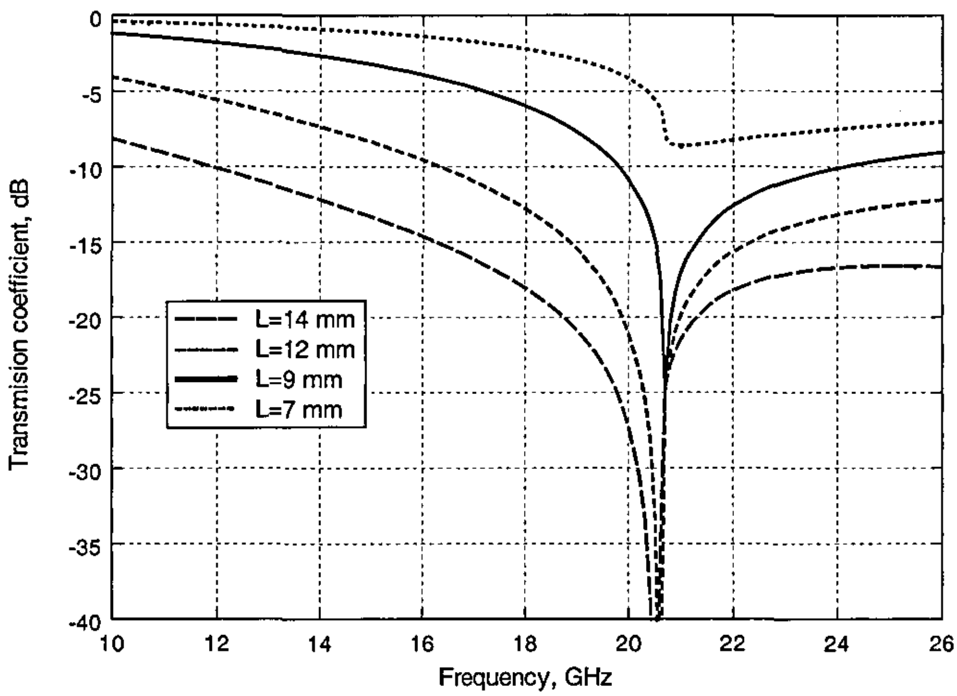

Figure 4.3 Effect of dipole length, L, on transmission response of single layer dipole array.

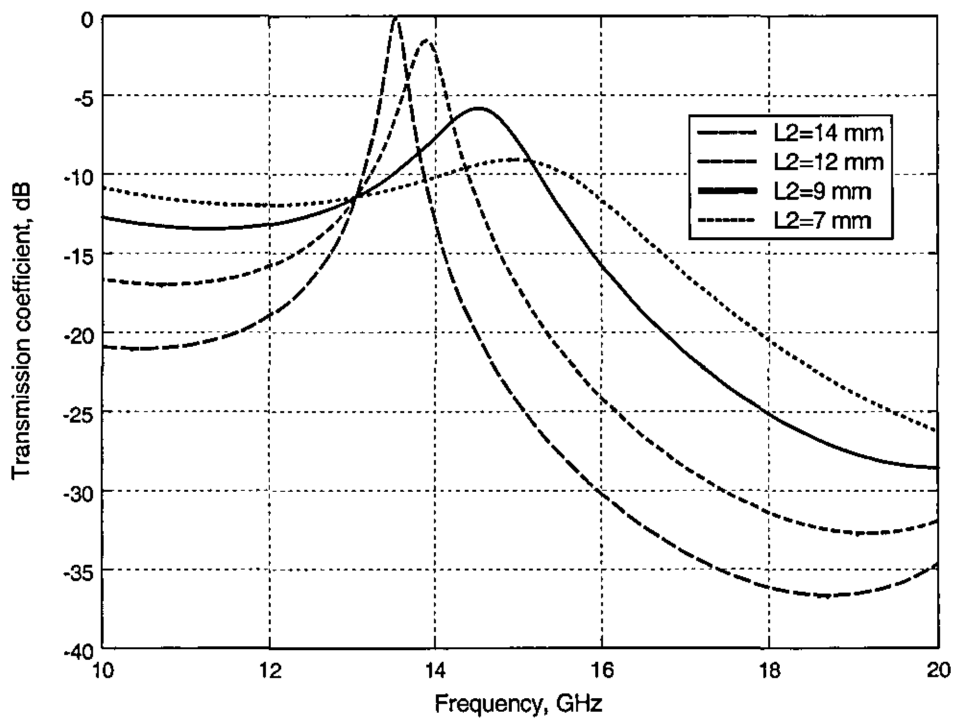

Figure 4.4 Effect of dipole length, L_2, of second layer on transmission response of double layer dipole array

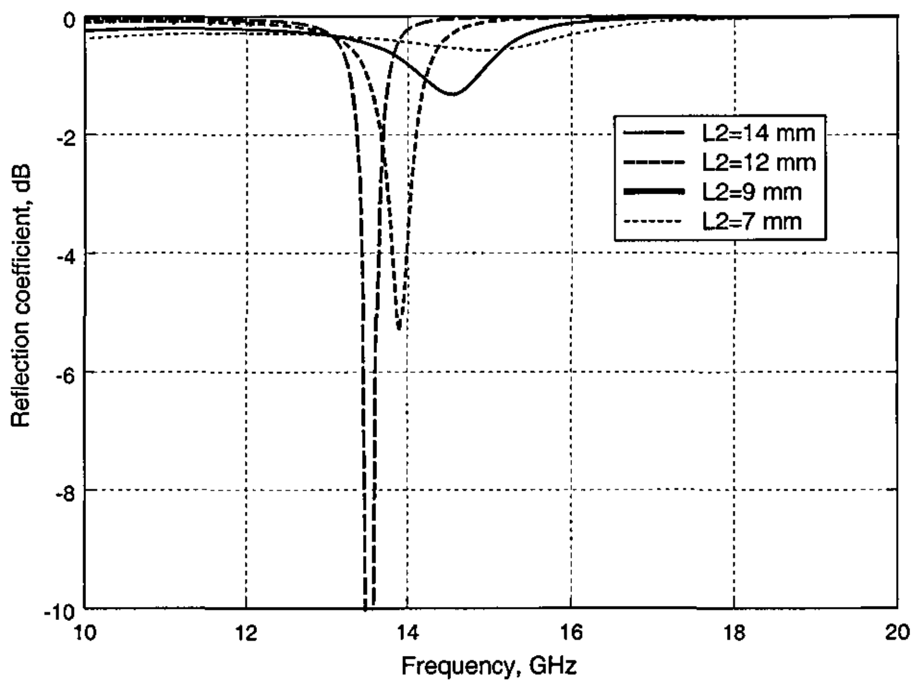

Figure 4.5 Effect of second layer dipole length, L_2, on reflection response of double layer dipole array

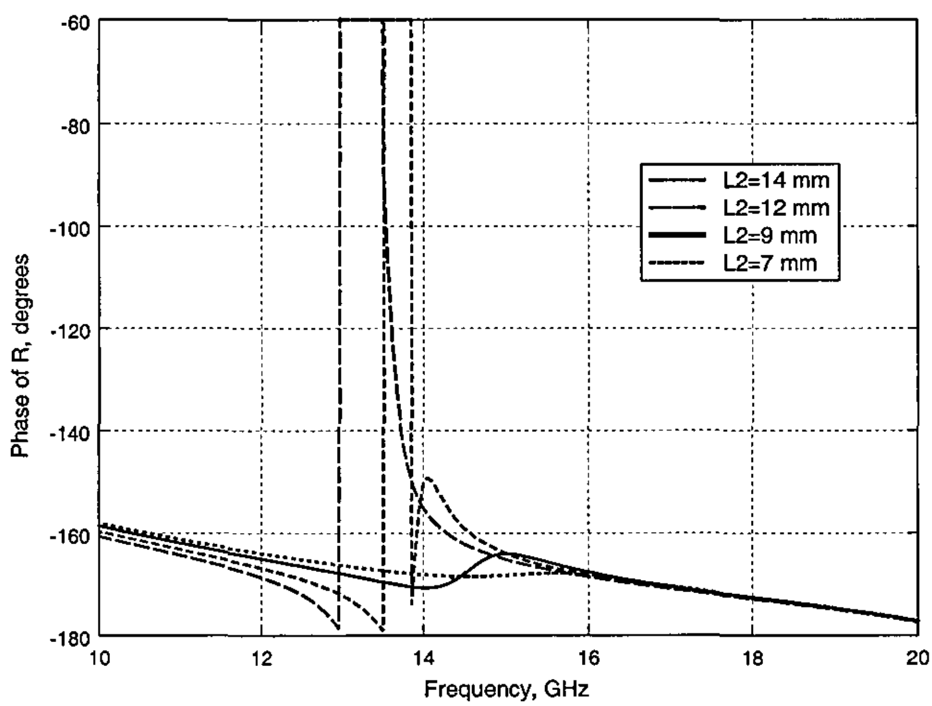

Figure 4.6 Effect of second layer dipole length, L_2, on phase of reflection coefficient of double layer dipole array

4.3 Antenna with Double Layer Dipole PRS

4.3.1 Optimised double layer dipole PRS

The optimised double-layer dipole array has been manufactured, [4]. The dipoles of each layer were etched on 32 μm thin polyester substrates of dielectric constant 3. The arrays have the same periodicity (D_y = 14.5 mm, D_x = 1 mm) but different dipole lengths (L_1 = 14 mm, L_2 = 9 mm, W = 0.5 mm), as shown in Fig. 4.7. The two layers were mounted on either side of a flat polystyrene foamboard ($\varepsilon_r \approx 1.05$), Fig. 4.7. The transmission coefficient of the double-layer array has been measured using 24×24 cm^2 screens. Simulation results of the array response including the dielectric layers have been obtained for a separation distance (i.e. foamboard thickness) of S = 12.6 mm and are in good agreement with measurements, Fig. 4.8. The semi-resonant effect due to array interference appears at about 13.5 GHz. In the reflection response, Fig. 4.8(b), the phase increase around 13.5GHz is evident. The optimum phase calculated from Eqn. (2.22) has also been plotted for comparison.

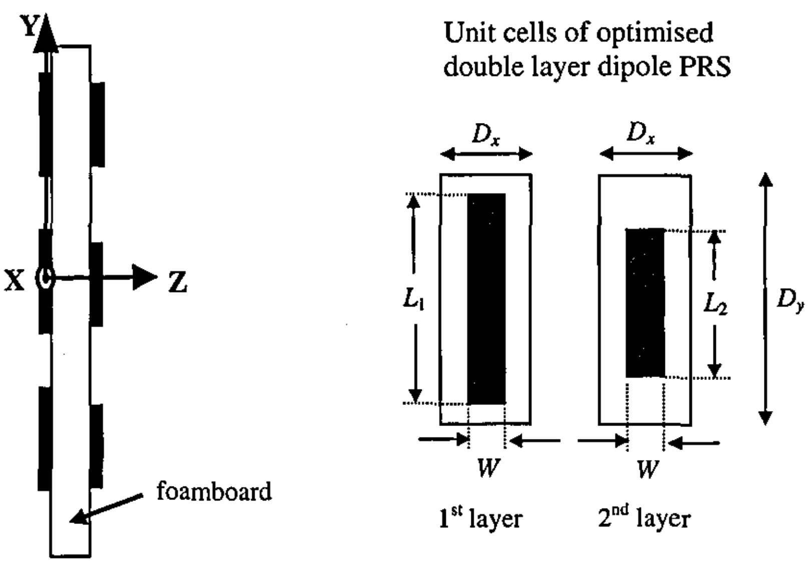

Figure 4.7 Cross section of double-layer PRS and geometry of unit cells

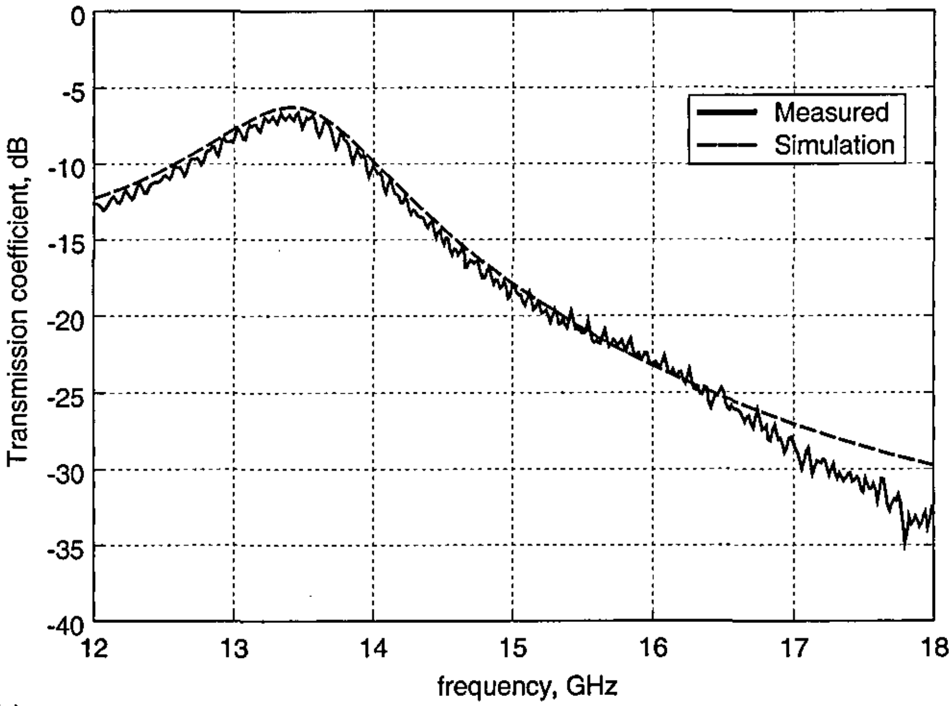

(a)

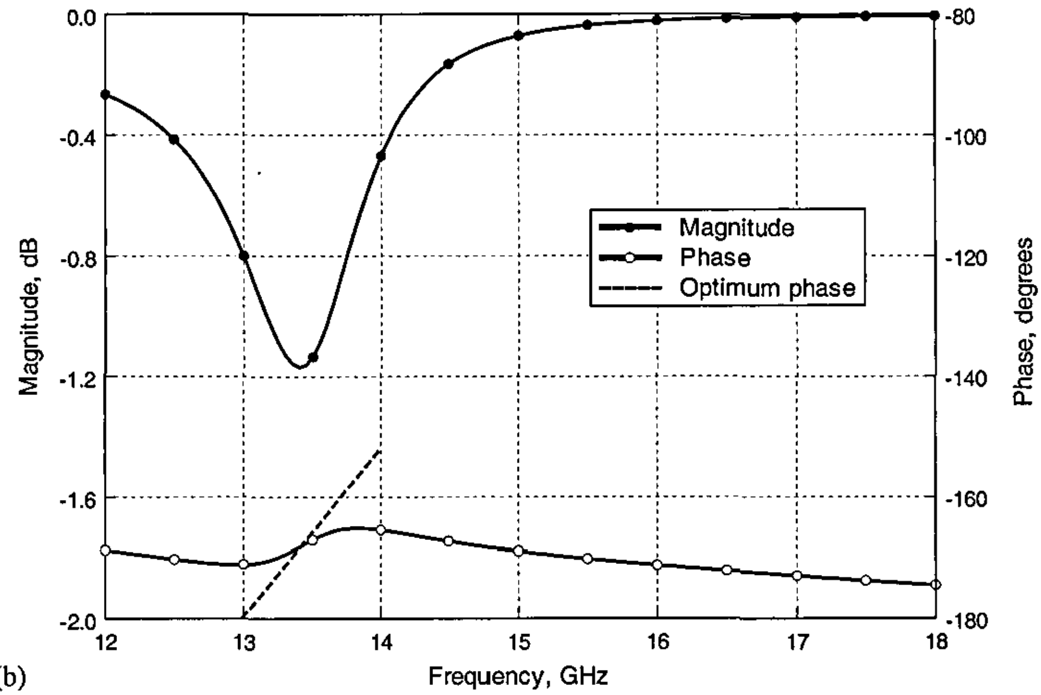

(b)

Figure 4.8 (a) Transmission coefficient (measured and simulated) and (b) simulated reflection coefficient of double layer dipole PRS

4.3.2 Optimum aperture size

The antenna has been formed using the optimised double-layer dipole PRS, Fig. 4.9. An open-ended J-band waveguide of inner dimensions 15.8×7.9 mm^2 was mounted in a 30×30 cm^2 ground plane to form the primary antenna. The frequency band between 13 and 14 GHz where the reflection phase increases is used as the design frequency of the antenna. Using Eqn. (2.12) an initial estimate of the antenna gain can be obtained, Fig. 4.10. The resonant distance as calculated by Eqn. (2.13) for a centre frequency of 13.4 GHz is 11.55 mm. As shown in Fig. 4.10, a more broadband performance is now expected, as compared to the single layer case. In the same figure, the gain of a frequency independent PRS (fictitious), which has the same reflection coefficient values as the double layer PRS at 13.4 GHz, is shown for comparison. As discussed in section 3.3, this fictitious surface represents the maximum possible bandwidth that can be attained with a single layer PRS, for a specific gain (see also Fig. 3.12). The characteristic reflection phase and magnitude response of the double-layer PRS design is expected to give a flat plateau of maximum gain values in a wide range of frequencies around the central one and, hence, considerably improved 1 dB and 3 dB bandwidths.

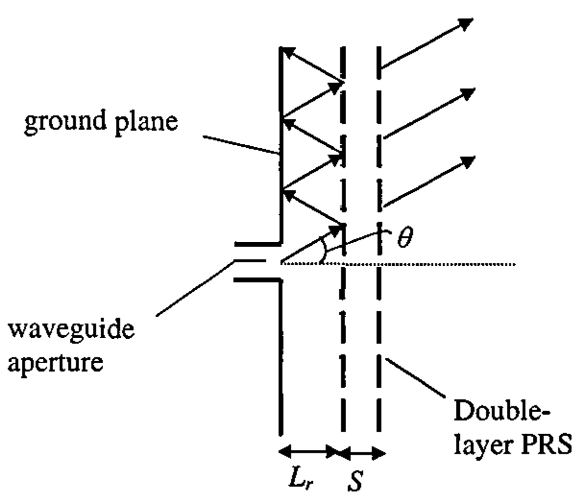

Figure 4.9 Schematic diagram of planar leaky-wave antenna with double-layer PRS

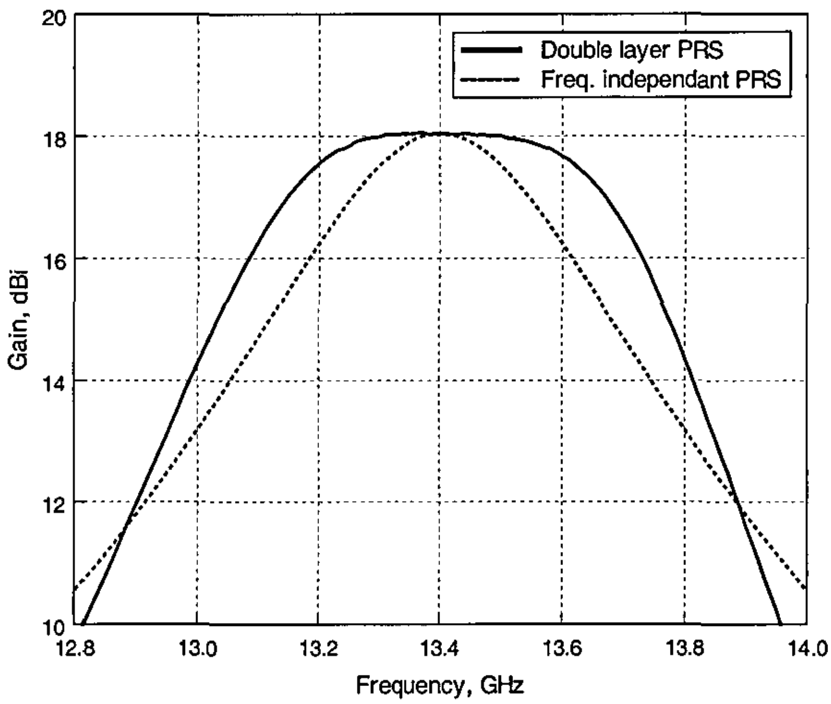

Figure. 4.10 Estimated gain (Eqn. 2.12) of antenna with double layer dipole PRS

In the measurements, the double layer dipole PRS was placed at a distance of about 11.5 mm over the ground plane. The PRS board was supported by four plastic screws attached to the ground plane. The limitations in the accuracy of the measurements are the same as those discussed in section 3.4.2. An experimental investigation into the effect of the size of the PRS on the antenna gain and bandwidth has been carried out. The antenna gain has been measured for different PRS sizes (Fig. 4.11) and the antenna efficiency has been calculated from Eqn. (3.9) for the centre frequency (Fig. 4.12). Error bars in both figures indicate the limitations in the accuracy of the gain measurements due to misplacement of the PRSs and the flatness of the foam boards.

A 24×24 cm^2 PRS size was initially used with an antenna gain of 14 dBi, quite lower than the one predicted from the approximate ray analysis. This gain discrepancy, apart from the approximate nature of the ray analysis, can also be attributed to the poor matching of the antenna. In particular, the measured return loss reached values as high as –3 dB in the operating frequency band. As the PRS was cut into sizes smaller than 15×15 cm^2 (square sheets) the gain increased, reaching a maximum value of 19 dBi for a 7.2×7.2 cm^2 PRS. For sizes smaller than 3×3 cm^2 the PRS has little effect and the antenna gain and efficiency finally resort to that of an open-ended grounded waveguide.

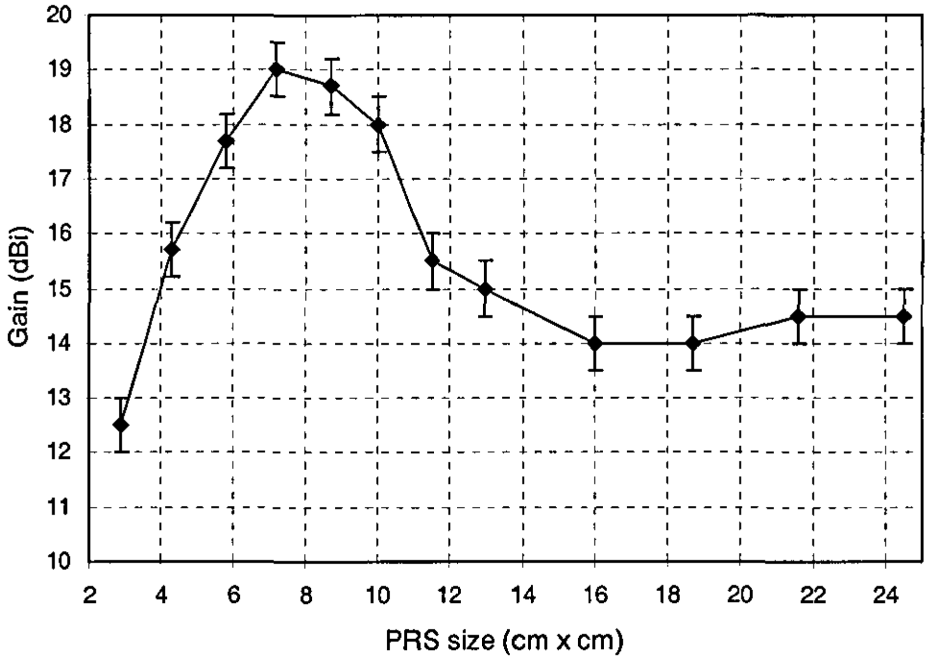

Figure 4.11 Effect of PRS size on antenna gain

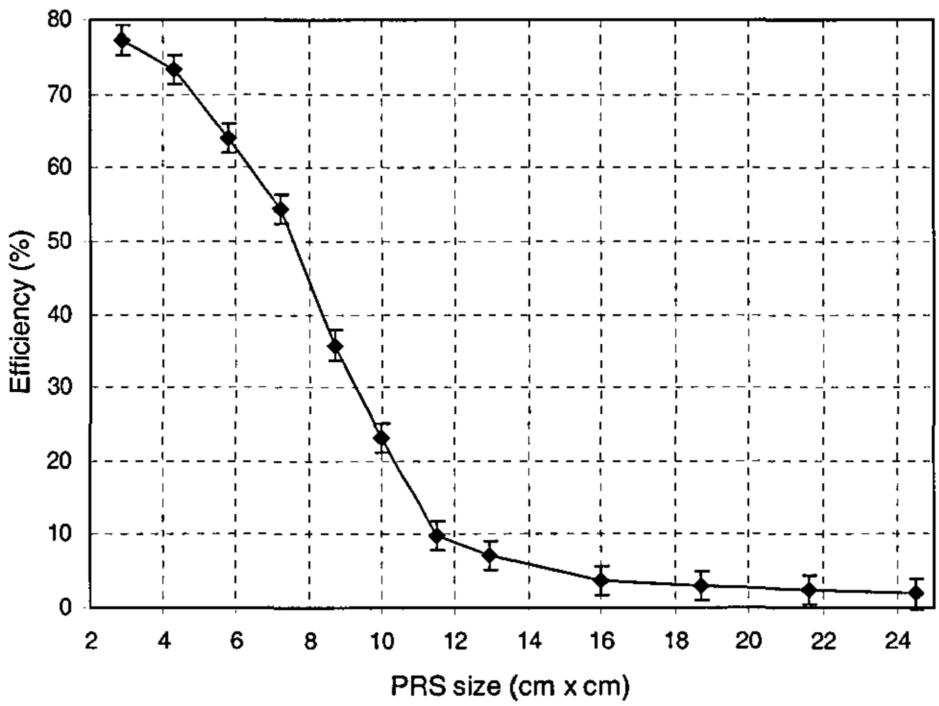

Figure 4.12 Effect of PRS size on antenna efficiency

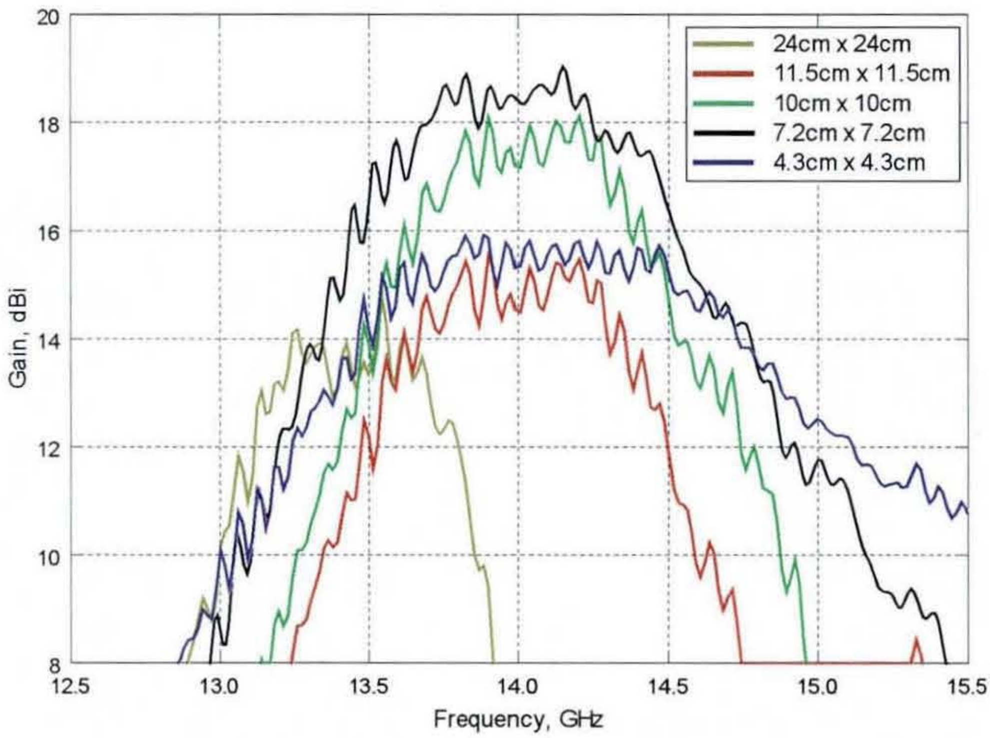

Figure 4.13 Measured gain of antenna with double-layer dipole PRSs of different size

Fig. 4.13 shows the measured antenna gain with frequency, for some of the PRS sizes used in the parametric study. As shown in the figure, the bandwidth of the antenna increases with decreasing size of PRS. An initial 3 dB fractional bandwidth of about 5.5% is obtained for the 24×24 cm^2 PRS, which increases to 7% for the optimum (with respect to maximum gain) PRS size (7.2×7.2 cm^2). The bandwidth increases further for smaller PRS sizes (but the gain drops several dBs) tending towards the wide band performance of an open-ended grounded waveguide.

The above study has shown that 7.2×7.2 cm^2 is the optimum PRS size for a maximum gain as well as broadband antenna performance. Smaller PRS size can yield wider bandwidth and could be used for applications where high gain is less crucial compared to bandwidth. It is quite interesting to note that maximum gain occurs for a particular PRS size, in this case for PRS of side $\approx 3\lambda_0$. At first glance this seems surprising since one might expect the gain to increase with aperture size. The higher gain of antenna with smaller PRSs could be attributed to constructive interference of the leaky and diffracted rays from the PRS edges as well as more uniform distribution of the field for the particular aperture size.

4.3.3 Antenna performance

The performance of the leaky-wave antenna (Fig. 4.9) formed with the 7.2×7.2 cm^2 double layer dipole PRS is presented here. The resonant distance is 11.5 mm. A 3D FDTD model of the antenna has been realised in LC. The size of the ground plane in the model was restricted to 15×15 cm^2, due to memory limitations. In addition, due to the small size of the PRS compared to the ground plane, a larger ground plane was not expected to alter the results significantly, since the fields would be very low at its edges. A uniform lattice composed of $340\times 340\times 100$ cubic cells of size 0.5mm ($\approx \lambda_0/40$) was used. A Gaussian current source was used as excitation in the waveguide, spaced at $\lambda_0/4$ from the back short. The boundary conditions on all sides were PMLs (eight layers), spaced 20 cells from the closest surface of the antenna. The simulation required 1.2 Gb of memory and took less than 20 hours running on an 8-processor Cray J90 for 20,000 time steps.

The measured gain in addition to the simulation results are shown in Fig. 4.14. The centre operating frequency is 14GHz. The 3 dB fractional bandwidth is over 7% and the maximum gain 19dBi. It should be noted that a broad 1 dB bandwidth of 5% has also been obtained. The overall antenna efficiency is 56 %. FDTD results give a good prediction of the antenna performance. It must be noted that the initial estimations obtained from the approximate analysis (Fig. 4.10) were confirmed.

The return loss of the antenna is as high as -3 dB in the lower part of the operating frequency band and drops to -10 dB only at the upper end of the band, Fig. 4.14. This could be expected, since the feeder (open-ended grounded waveguide) in the antenna was not optimised for the specific frequency range. An optimisation of the impedance of the feeder would be required in order to improve the antenna matching.

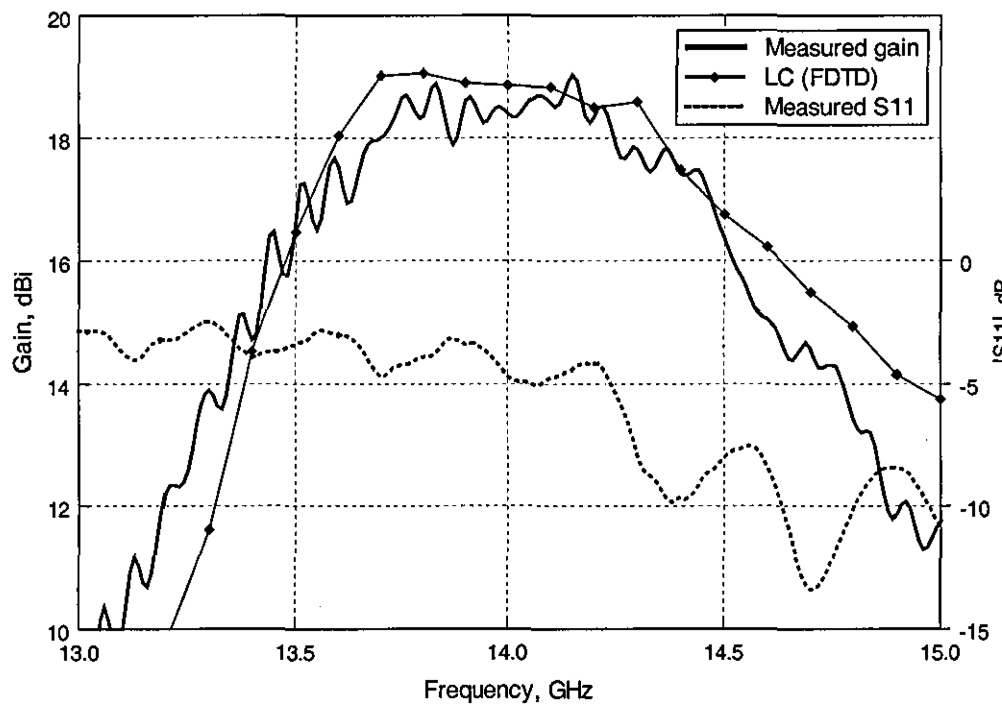

Figure 4.14 Gain of antenna with 7.2×7.2 cm^2 double layer dipole PRS

The H-plane radiation patterns of the antenna are shown in Fig. 4.15 for the centre frequency (14 GHz) and for the edges of the operating frequency band (13.5 GHz and 14.5 GHz). Fig. 4.16 shows the corresponding E-plane patterns. A good agreement between simulation results and measurements is observed. The sidelobe level (SLL) remains lower than –12 dB in the H-plane and –15 dB in the E-plane at the centre frequency. At lower frequencies SLL is even lower and the main beam is slightly wider. At higher frequencies SLL increases to –10 dB and the main beam exhibits some distortion.

The small shift from the boresight in the patterns is due to alignment errors such as a slight misplacement of the PRSs. Cross polarisation level has been measured and is below 30 dB throughout the frequency range studied here.

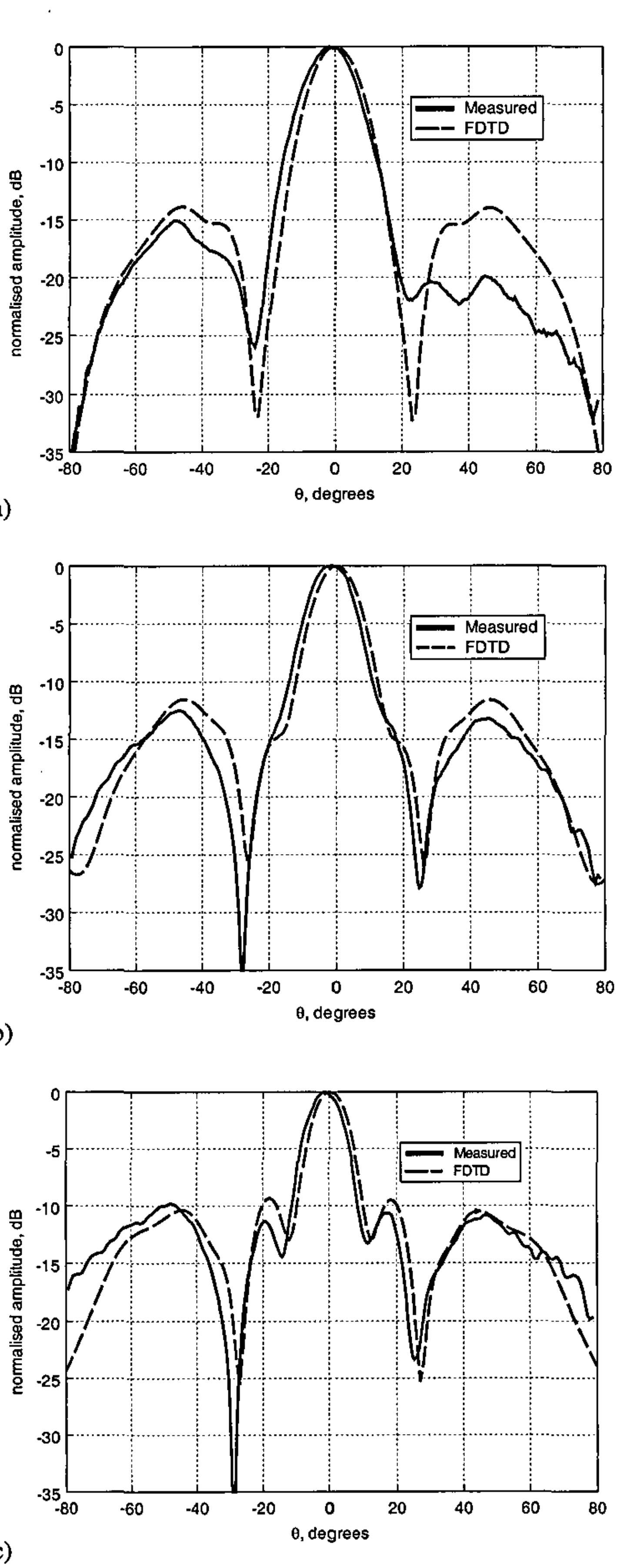

(a) (b) (c)

Figure 4.15 H-plane radiation patterns of antenna at: (a) 13.5 GHz; (b) 14 GHz; (c) 14.5 GHz

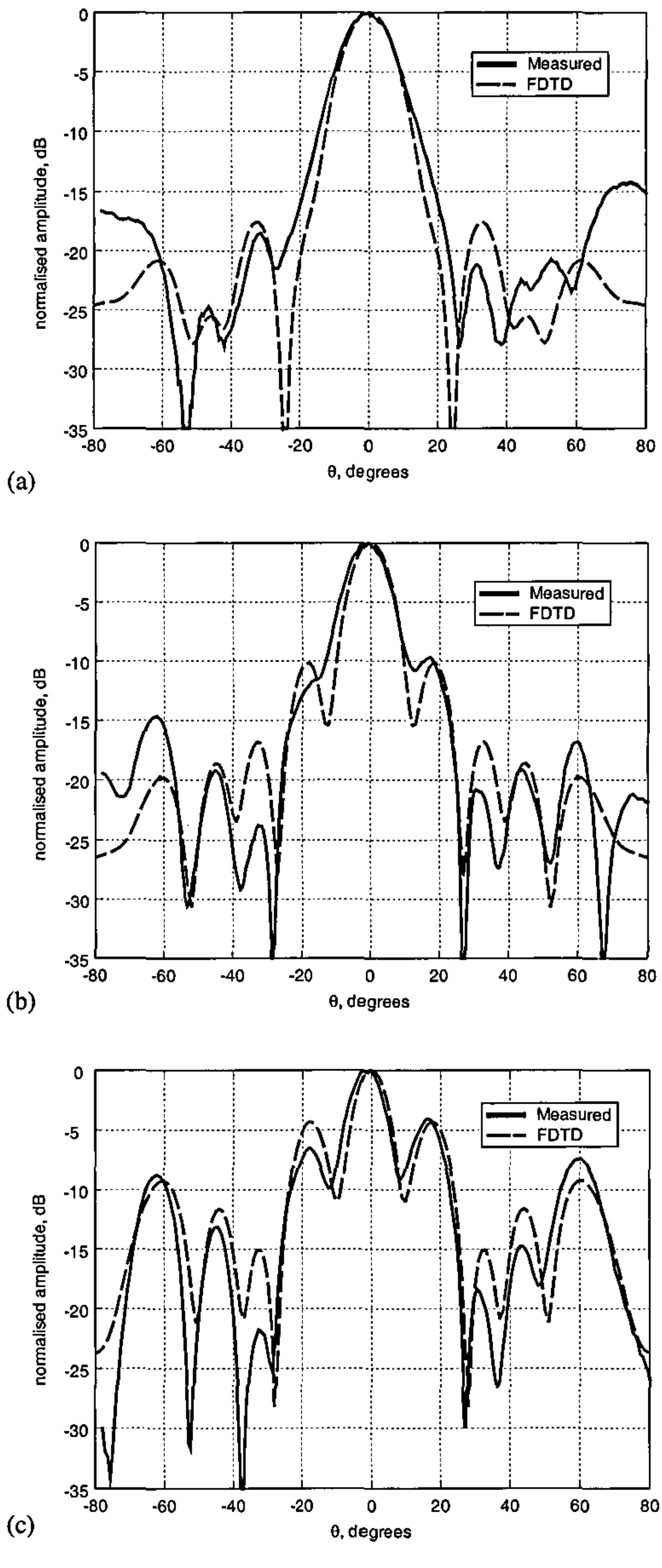

Figure 4.16 E-plane radiation patterns of antenna at: (a) 13.5 GHz; (b) 14 GHz; (c) 14.4 GHz

4.4 Slot Feed Design

A new feeding structure has been designed in order to improve the matching of the antenna. In order to match the impedance of the resonant cavity formed by the ground plane and the PRS to the waveguide, a resonant slot has been used to replace the waveguide aperture in the ground plane. The slot acts as a shunt inductance [5, 6]. The slot thickness was the same as the thickness of the ground plane (1mm). The size of the ground plane has been reduced to 15×15 cm^2. The slot is fed by the J-band rectangular waveguide. It has been designed to resonate at the expected resonant frequency of the antenna, i.e. about 14 GHz and also to have enough bandwidth for its use as a feeder in the leaky-wave antenna configuration.

For the design of the waveguide-fed slot, the structure has been modelled in Microstripes. 3D simulations of the waveguide-fed slot in the ground plane have been carried out. The package provided features as symmetry conditions, non-uniform meshing and automatic return loss calculation, which resulted in a significant reduction of the computational size of the model. Thus, the simulation could be carried out, within a reasonable time, on a PC.

A slot of 10mm length and 2mm width was found to have a quite low return loss as well as a reasonably good bandwidth. The structure was modelled using non-uniform meshing with cell sizes of no larger than $\lambda/30$ (for 14 GHz). Higher resolution has been used at the area within and near the slot, where the fields are higher. In particular, the smallest cell size was 0.5 mm. A TE_{10} mode excitation was used in the waveguide. The waveguide-ports option in Microstripes allows for an automatic waveguide mode excitation, provided that the inner surface of the guide as well as the cutoff frequency is given. The symmetry of the structure as well as of the excitation in both horizontal (x) and vertical (y) axes was exploited in order to reduce the computational requirements. The electric field is polarised in the vertical direction, thus a magnetic wall was placed along the y-axis and an electric wall along the x-axis, both cutting the structure in the middle. Consequently, only a quarter of the initial model was used in the TLM simulation. PML absorbing boundary conditions (8 layers) were used on all other sides, spaced at least 20 cells from the closest surface of the antenna. The simulation required 300 Mb (2.5 million cells) and took 10 hours on a 1.2 GHz Athlon PC for 12,500 time steps.

The waveguide-fed slot has been manufactured and measured. Fig. 4.17 shows a photograph of the structure. Measurements were in satisfactory agreement with simulation predictions (Fig. 4.18). The ripple in the measured response is due to standing waves in the waveguide and the effect of the coax-to-waveguide transition. A minimum S_{11} of –25 dB was obtained at about 14 GHz. The –10dB S_{11} bandwidth was over 1.5 GHz, which corresponds to more than 10% fractional bandwidth. Narrower slots resulted in lower return loss but also narrower bandwidths, which would not be suitable for a broadband leaky-wave antenna performance. A larger slot width would increase the -10dB bandwidth but the S_{11} would have higher values at the central frequencies, thus deteriorating the resonant response.

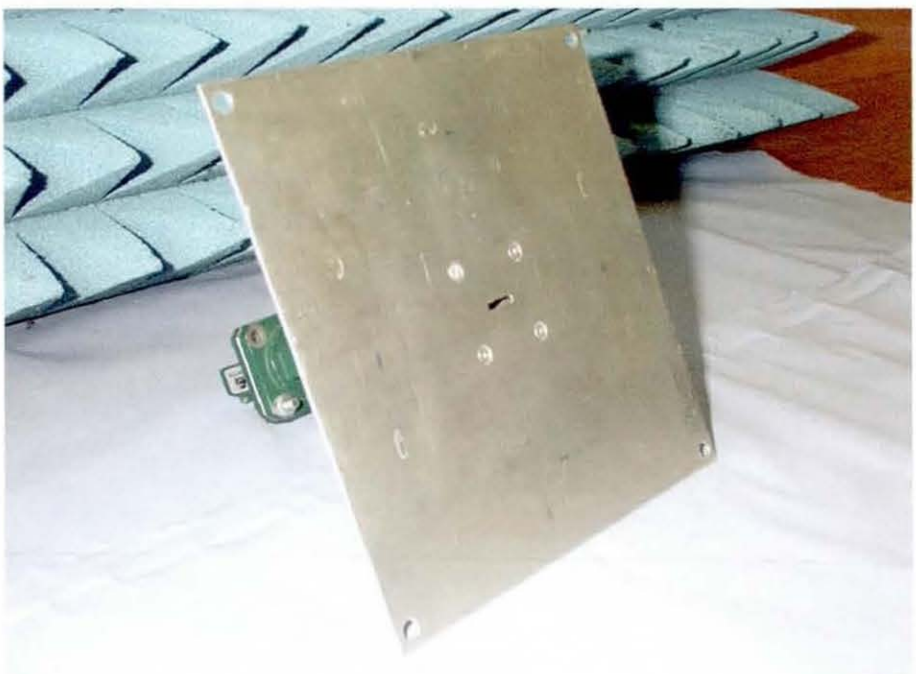

Figure 4.17 Waveguide-fed slot in 15 $\times$ 15 cm^2 ground plane of thickness 1mm.

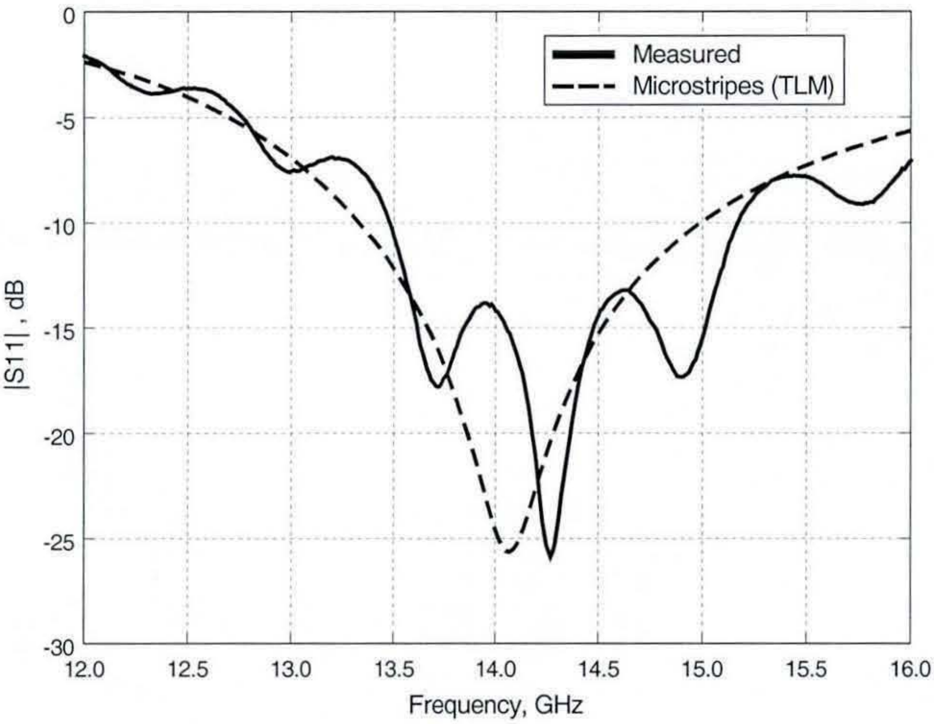

Figure 4.18 Return loss (S11) of waveguide-fed slot in 15 × 15 cm^2 ground plane

4.5 Antenna with Double Layer Square Patch PRS and Slot Feed

The antenna has been formed using a double layer square patch array. The square patch element is symmetrical in both *x* and *y* axes and thus it can be used for dual polarisation designs. The array has been printed on a thicker dielectric substrate, as compared to the dipole PRS, in order to produce a more rigid prototype structure. In addition, the slot feed has been used resulting in an improvement of the antenna matching. A broadband antenna performance with high antenna efficiency and relatively high-gain has been obtained.

4.5.1 Optimised double layer square patch PRS

A design procedure similar to that of section 4.2 has been carried out, in order to produce a double layer square patch array design with reflection characteristics close to the optimum PRS response for high gain and wideband leaky-wave antenna performance. The PRS array has been printed on a rigid dielectric substrate (TLX8, produced by Taconic) of 1.5 mm thickness and relative permittivity 2.55. The loss tangent is 0.002 for frequencies near 14 GHz.

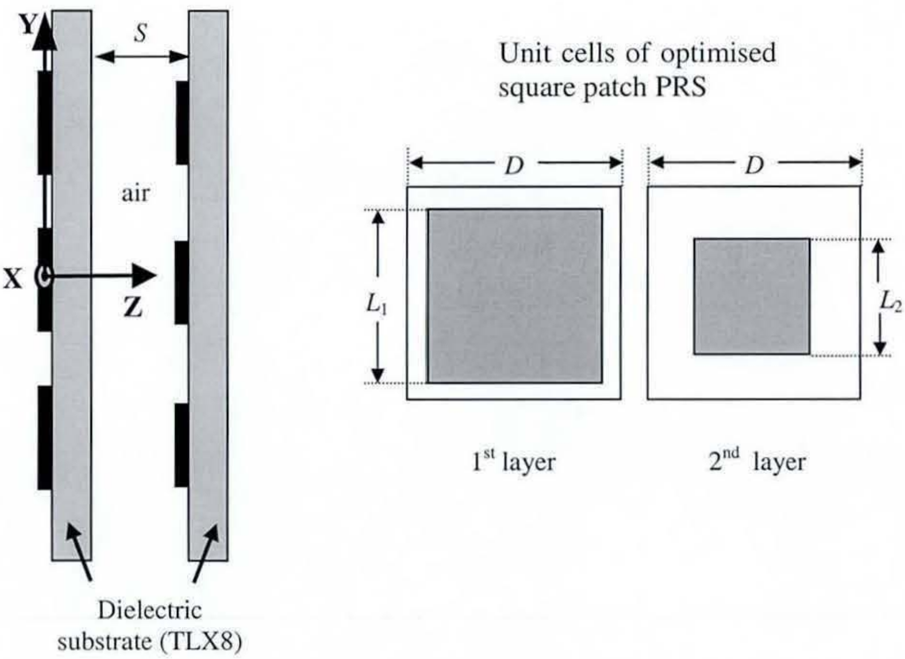

Figure 4.19 Cross section of double-layer square patch PRS and geometry of unit cells

The Floquet plane wave modal analysis has been used to simulate the (infinite) array response, taking into account the dielectric layers. Each of the two square patch arrays was designed to have similar reflectivity to the corresponding one in the double layer dipole array design. The patches in the first array are closely spaced together resulting in high reflectivity values and a slow variation of the transmission/reflection response with frequency. The second layer patch size is smaller in order to exhibit lower reflectivity and thus produce a semi-resonant effect as discussed in section 4.2.2. After a parametric study the following unit cell dimensions were used: D = 11 mm, L_1 = 10 mm (1st layer), L_2 = 6 mm (2nd layer). The separation distance of the two PRSs was S = 11 mm. The PRSs are separated by air and as it will be discussed in the next section, are attached to each other and to the ground plane by the use of plastic spacers placed in the four corners of the dielectric boards.

The simulated reflection coefficient (magnitude and phase) of the optimised double layer square patch array is shown in Fig. 4.20. The minimum reflection value appears at 13.7 GHz and is a little lower than the one obtained from the double layer dipole PRS. The phase increases with frequency in the range between 13.2 GHz and 14.2 GHz and is close to the optimum PRS phase response, which is also plotted for comparison.

An estimation of the gain of the leaky-wave antenna formed with the double layer square patch PRS is obtained from Eqn. (2.12) and it is shown in Fig. 4.21. The resonant distance L_r, calculated from Eqn. (2.13) for the centre frequency of 13.7 GHz, is 11.33 mm. A broadband antenna performance is expected. The bandwidth is now larger as compared to the double-layer dipole PRS design but the gain is expected to be lower.

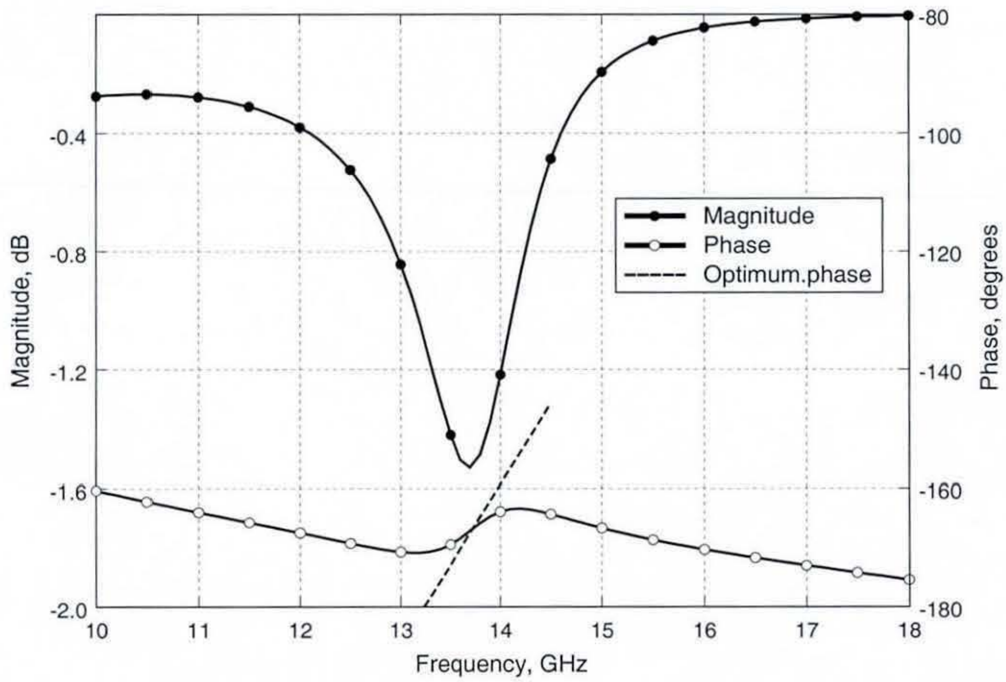

Figure 4.20 Reflection coefficient (magnitude and phase) of double layer square patch PRS

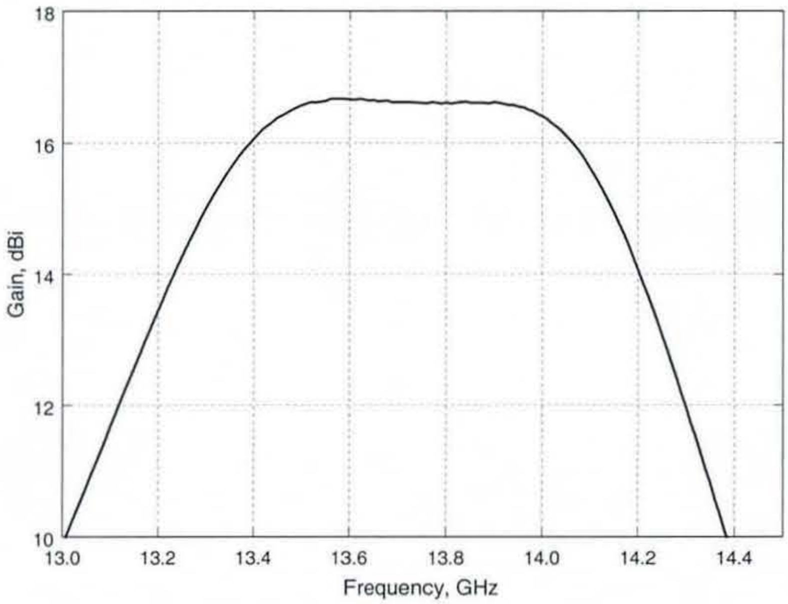

Figure 4.21 Estimated gain of antenna with double layer square patch PRS

4.5.2 Effect of PRS size

The leaky-wave antenna has been formed using the optimised double-layer square patch PRS. The waveguide-fed slot has been used as feeder. The square patch arrays were fabricated in four different sizes: 12×12 cm^2, 9.8×9.8 cm^2 , 7.6×7.6 cm^2 and 5.4×5.4 cm^2, all printed on 15×15 cm^2 dielectric (TLX8) boards of 1.5 mm thickness, as discussed in the previous section. The PRS boards were attached to the ground plane using four plastic screws, one at each corner. Plastic spacers were also used to keep the boards parallel and at the specified distances above the ground plane. The length of the plastic spacers used in the antenna prototype had a tolerance of about ± 0.05 mm.

A sketch of the antenna is depicted in Figure 4.22, showing the thick waveguide-fed slot, the spacers and the position of the PRSs. A photograph of the antenna prototype is also shown in Fig. 4.23. The PRS boards were separated by spacers of 11 mm length. The resonant distance of the first PRS from the ground plane was set using spacers of 11.3 mm length. The tolerance in the distances was ± 0.05 mm, due to the tolerance of the spacers.

The antenna gain has been measured for each of the double-layer PRS sizes, as shown in Fig. 4.24. Higher maximum gain has been obtained for the smaller size PRSs. A maximum gain of 18.8 dBi was obtained with the 7.6×7.6 cm^2 double layer PRS. However, the gain values fluctuate with frequency by more than 2 dB and the gain is lower at the centre frequency. For the 5.4×5.4 cm^2 PRS the gain values are more uniform and the maximum gain obtained is 17.5 dBi. Furthermore, the antenna efficiency is higher, reaching a maximum value of 76% at 13.5 GHz. Larger PRS sizes gave lower gain as well as higher fluctuation of the gain values.

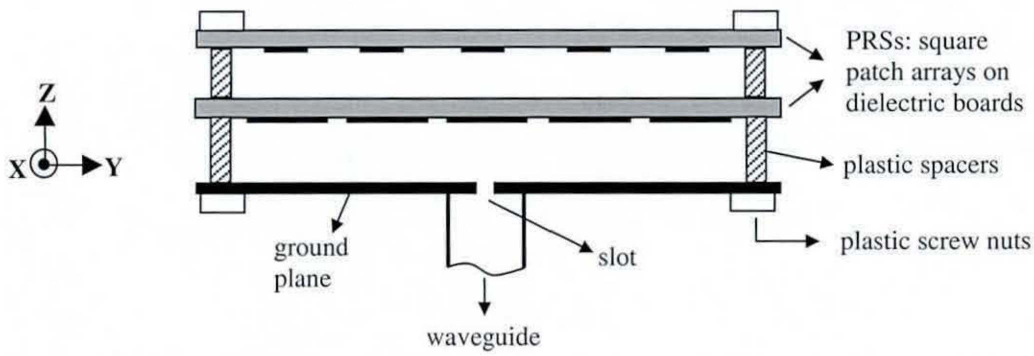

Figure 4.22 Schematic diagram of planar slot-fed leaky-wave antenna with double layer PRS printed on dielectric boards

The antenna 3 dB bandwidth is relatively wide and increases with decreasing PRS size. The widest bandwidth is obtained for the smaller (5.4×5.4 cm^2) PRS, which also has the most uniform gain performance.

When compared to the gain of the waveguide-fed antenna with the double layer dipole PRS of section 4.3 the following observations can be made. Similar trends in the antenna gain and bandwidth are noticed with decreasing size of the double layer PRS. The maximum antenna gain is obtained for similar PRS size in both cases. This was expected, since the dipole and square patch PRSs were designed to have similar reflections characteristics. However, in the latter case the gain values are less uniform with frequency, particularly for the larger PRS sizes. This could be attributed to the slightly lower reflectivity values of the double layer square patch PRSs (compare Figs 4.20 and 4.8), which resulted in lower gain, particularly in the centre frequency where the reflection values were even lower. On the other hand, the 3 dB bandwidth is now higher.

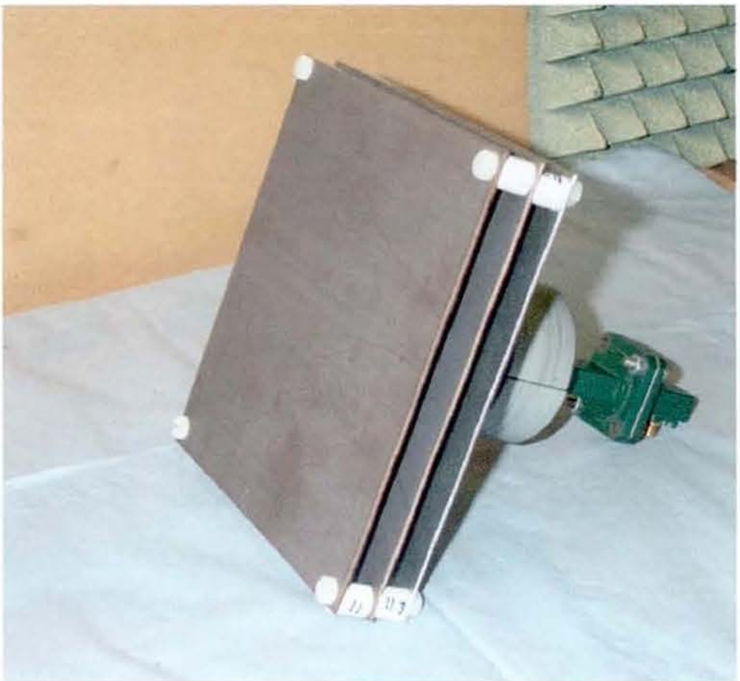

Figure 4.23 Photograph of the antenna prototype

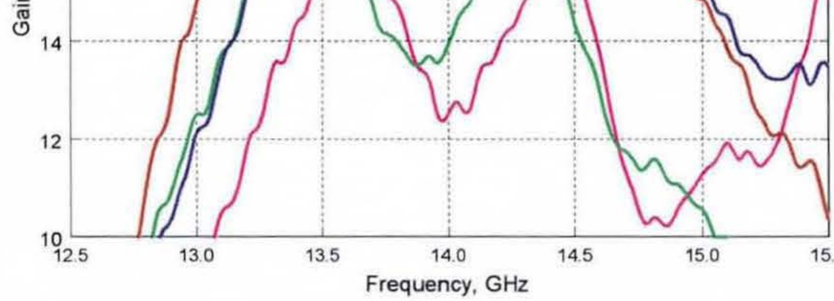

Figure 4.24 Measured gain of antenna with double-layer square patch PRSs of different size

4.5.3 Antenna performance

The performance of the slot-fed leaky-wave antenna with the 5.4×5.4 cm^2 double layer square patch PRS is presented here. Simulation predictions are also presented and compared with measurements. A photograph of the PRS boards used in the antenna prototype is shown in Fig. 4.25.

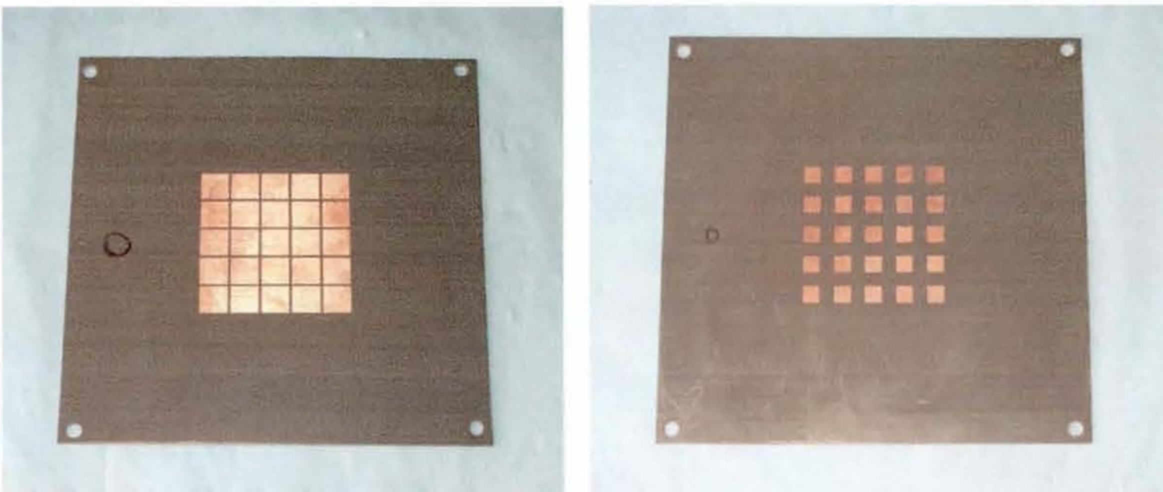

Figure 4.25 Square patch PRS arrays (5.4×5.4 cm^2) printed on 15×15cm^2 dielectric (TLX8) boards

The antenna has been modelled in Microstripes and simulations of its performance have been carried out prior to the manufacturing procedure. The waveguide-fed slot model described in section 4.4 has been used and the PRS arrays have been modelled with the appropriate dimensions and distances. A resolution of 0.5 mm allowed a satisfactory modelling of the square patch array dimensions (D = 11 mm, L_1 = 10 mm, L_2 = 6 mm). For the modelling of the resonant distance (11.3 mm), cells of slightly smaller size in the z-direction were used. Because of the symmetry of the structure magnetic and electric walls were used (as in section 4.4). In order to use the magnetic and electric walls we assumed that the electric field on either sides of the PRS patches is purely vertically polarised, as in the waveguide. This is actually true as seen in the low measured cross-polarisation values, which are discussed later on. The model consisted of 3.5 million cells and the simulation required 450 Mb of memory. It converged well within 14 hours on an Ahtlon 1.2 GHz PC for 12,500 time steps.

The measured and simulated antenna gain and return loss (or S_{11}) are shown in Figures 4.26 and 4.27 respectively. The maximum gain is 17.5 dBi at 13.5 GHz, corresponding to a high antenna efficiency of $e = 76\%$. At the centre frequency (14 GHz) the gain drops to 16 dBi ($e = 50\%$), but it increases again until 17 dBi ($e = 60\%$) at 14.6 GHz. The simulation prediction is in satisfactory agreement throughout most of the operating frequency band, apart from the upper end. The measured gain is slightly lower as compared to the predicted one and the bandwidth is wider. This might occur due to limitations in the accuracy of the spacing of the PRSs as well as small manufacturing tolerance errors. In particular, a slightly larger spacing of the PRSs than the one used in the simulation model (11 mm), would result in lower reflection values of the double layer array as indicated in section 4.2.2. This would result in a decrease in the leaky-wave antenna gain which is followed by a wider bandwidth. The 3dB fractional bandwidth, as obtained from the measured results, is more than 13 %.

The measured return loss is lower than –8 dB throughout the operating band (as defined by the 3 dB gain bandwidth). Some higher values appear around 14.3 GHz. The improvement of the antenna matching as compared to the waveguide-aperture-fed antenna structure (section 4.3) is significant. The simulation results are also in satisfactory agreement with measurements.

The measured and simulated radiation patterns are shown in Fig. 4.28 (*H*-plane) and Fig. 4.29 (*E*-plane), for a number of frequencies in the operating band. Based on the consideration of the antenna patterns (for SLL<-10dB) the bandwidth is about 10 %. In the *H*-plane the sidelobe level (SLL) is less than –15 dB at lower frequencies and it increases with frequency, reaching values of more than –10 dB at the upper end of the band. In contrast, in the *E*-plane the SLL is higher in lower frequencies (-10 dB) and drops as frequency increases. The main lobe in the *E*-plane is distorted at the upper end of the operating band. Cross-polarisation levels were low (<-25 dB) throughout the operating frequency band. The simulation predictions were confirmed and the simulation results are in satisfactory agreement with measurements. The wider main lobe and higher SLL of the simulated patterns at 15.1 GHz, as compared to the measured ones, are an indication of the lower gain obtained in the simulation for frequencies at the upper end of the operating band.

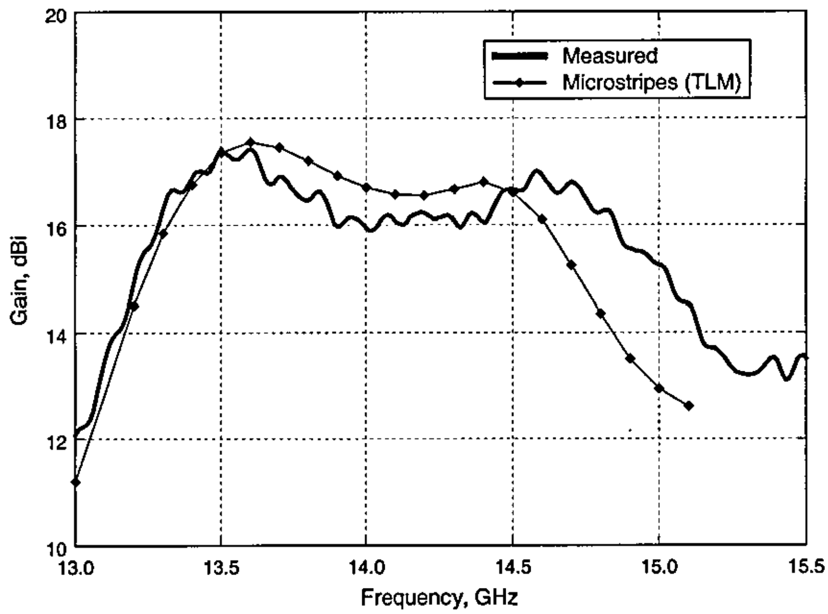

Figure 4.26 Gain of slot-fed antenna with 5.4×5.4 cm^2 double layer square patch PRS

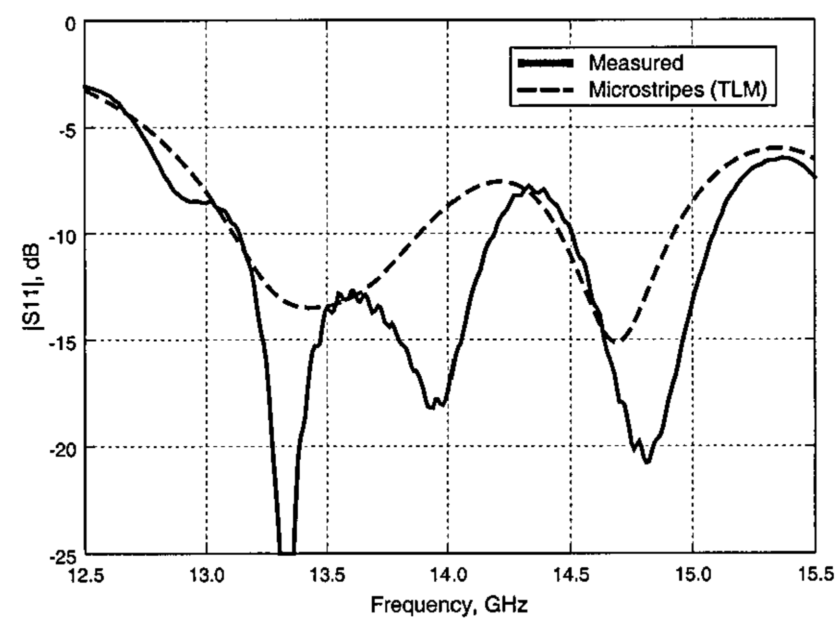

Figure 4.27 Return loss slot-fed antenna with 5.4×5.4 cm^2 double layer square patch PRS

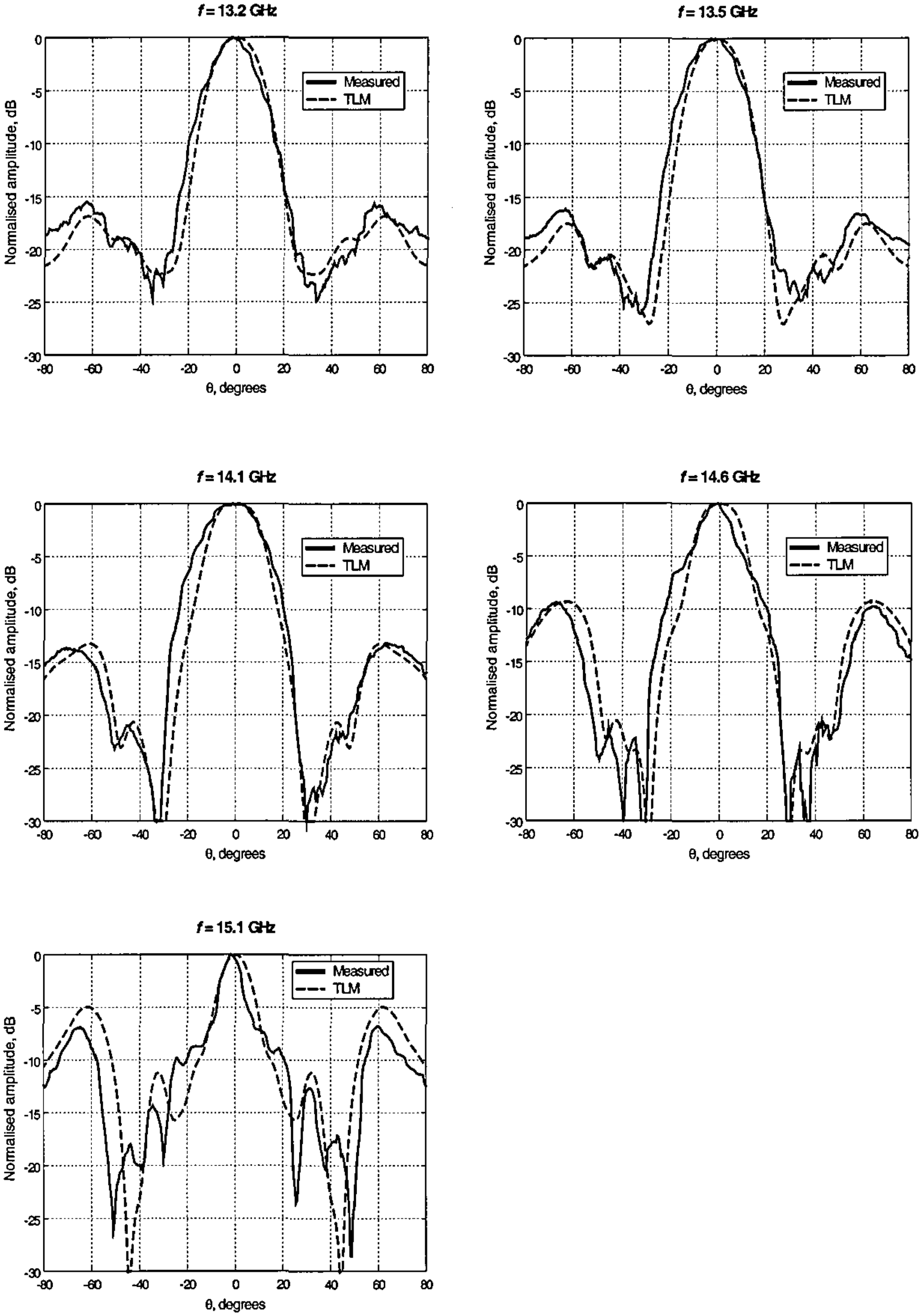

Figure 4.28 H-plane radiation patterns (measured and simulated) of antenna at several frequencies

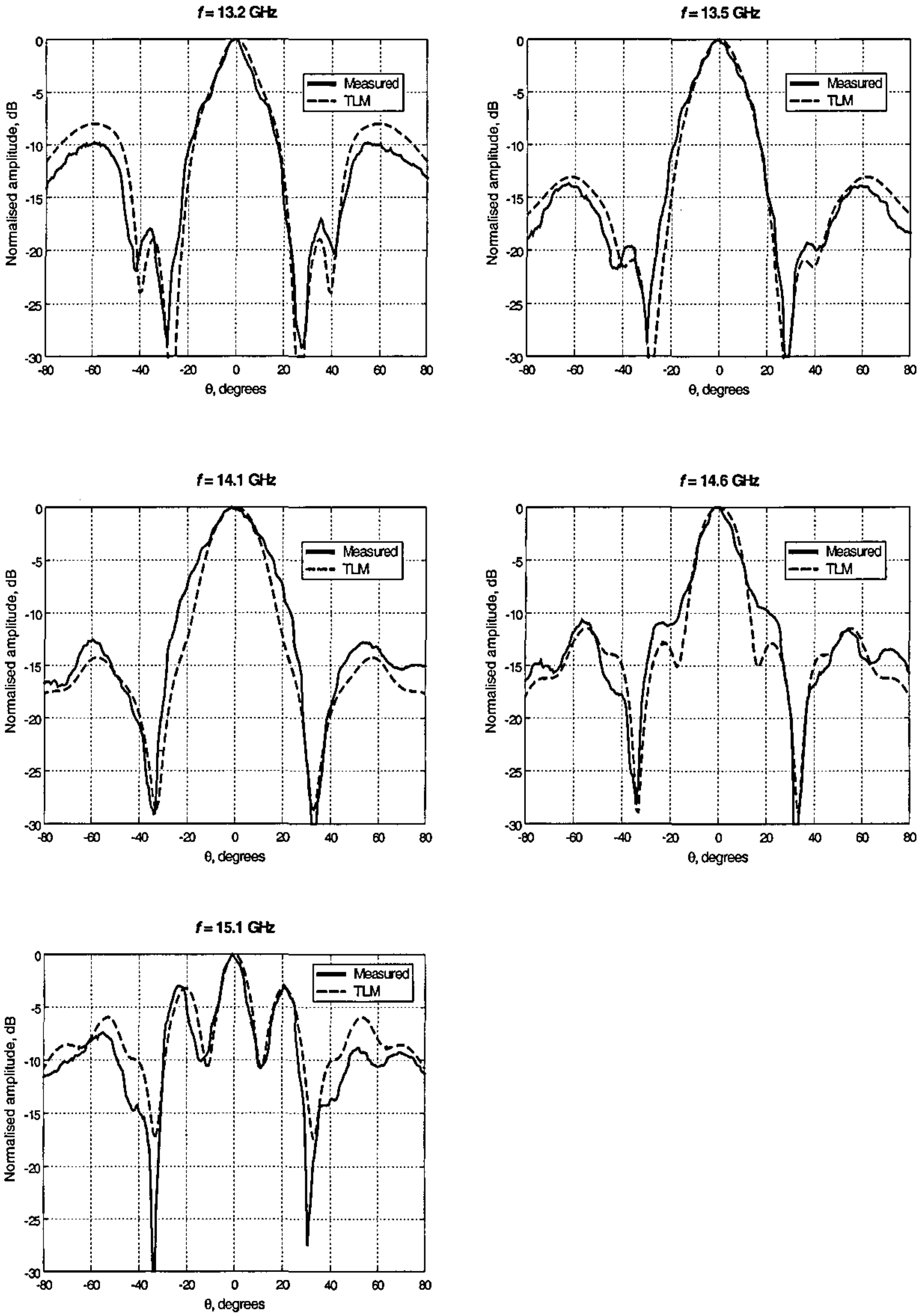

Figure 4.29 E-plane radiation patterns (measured and simulated) of antenna at several frequencies

The total surface current (magnitude of current vector) on the square patches of both arrays of the double layer PRS have been obtained in Microstripes. Fig. 4.30 shows the currents on the square patch array of the first layer for several frequencies and Fig. 4.31 shows the corresponding currents on the patches of the second layer. Since only a quarter of the antenna structure was used in the simulation (due to the symmetry conditions) the figures show the currents on a quarter of the square patch arrays. The currents on the rest of the patches are symmetrical with respect to both x and y - axes.

At lower frequencies the currents on the central patches of both arrays are high but little energy reaches the ends of the arrays. As the frequency increases more area of the arrays is excited. In particular, on the second layer array at the centre frequency (14 GHz) the currents are quite high on almost all patches. For frequencies near the upper end of the band, the currents increase on the edge patches but decrease considerably on the middle ones, resulting in a gain reduction as well as a distortion of the main lobe by the appearance of additional sidelobes in the radiation patterns (Figs 4.28, 4.29).

The near field distribution (magnitude of electric field vector) is shown for a surface of 15.6×15.6 cm^2 at a distance of 1 mm over the front end of the antenna. The field is shown at the centre frequency (14.1 GHz) as well as at the edges of the operating frequency band. The size of the square patch array of the first layer (5.4×5.4 cm^2) is depicted with a dashed line. At the centre frequency the fields over the PRS are high and have a quite uniform distribution. The diffracted fields can be seen on either side of the PRS in both *H* and *E* planes. At 13.2 GHz the field over the PRS is less uniform and concentrated at the centre. The diffracted fields are quite high in the *E*-plane, which explains the high sidelobes in the *E*-plane radiation patterns at this frequency. Finally, at 15.1 GHz the fields are lower and less uniform. The non-uniform field distribution is due to the non-uniform surface currents on the second array and it is the reason for the distorted main lobe in the radiation pattern, particularly in the *E*-plane. The diffracted fields are a bit higher in the *H*-plane, which also explains the higher sidelobes at this plane in large angles.

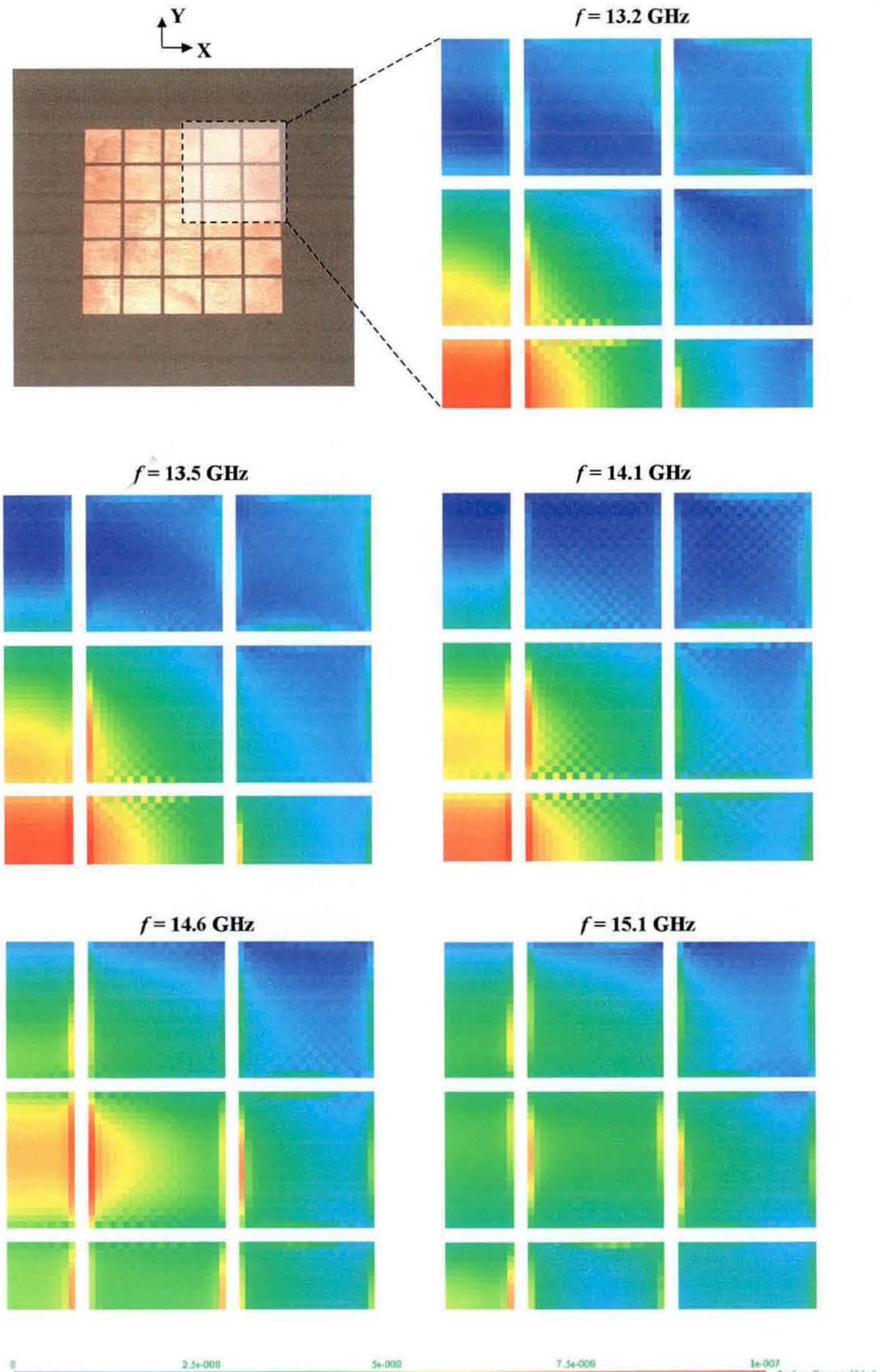

Figure 4.30 Total surface current density (magnitude) on square patches of first layer

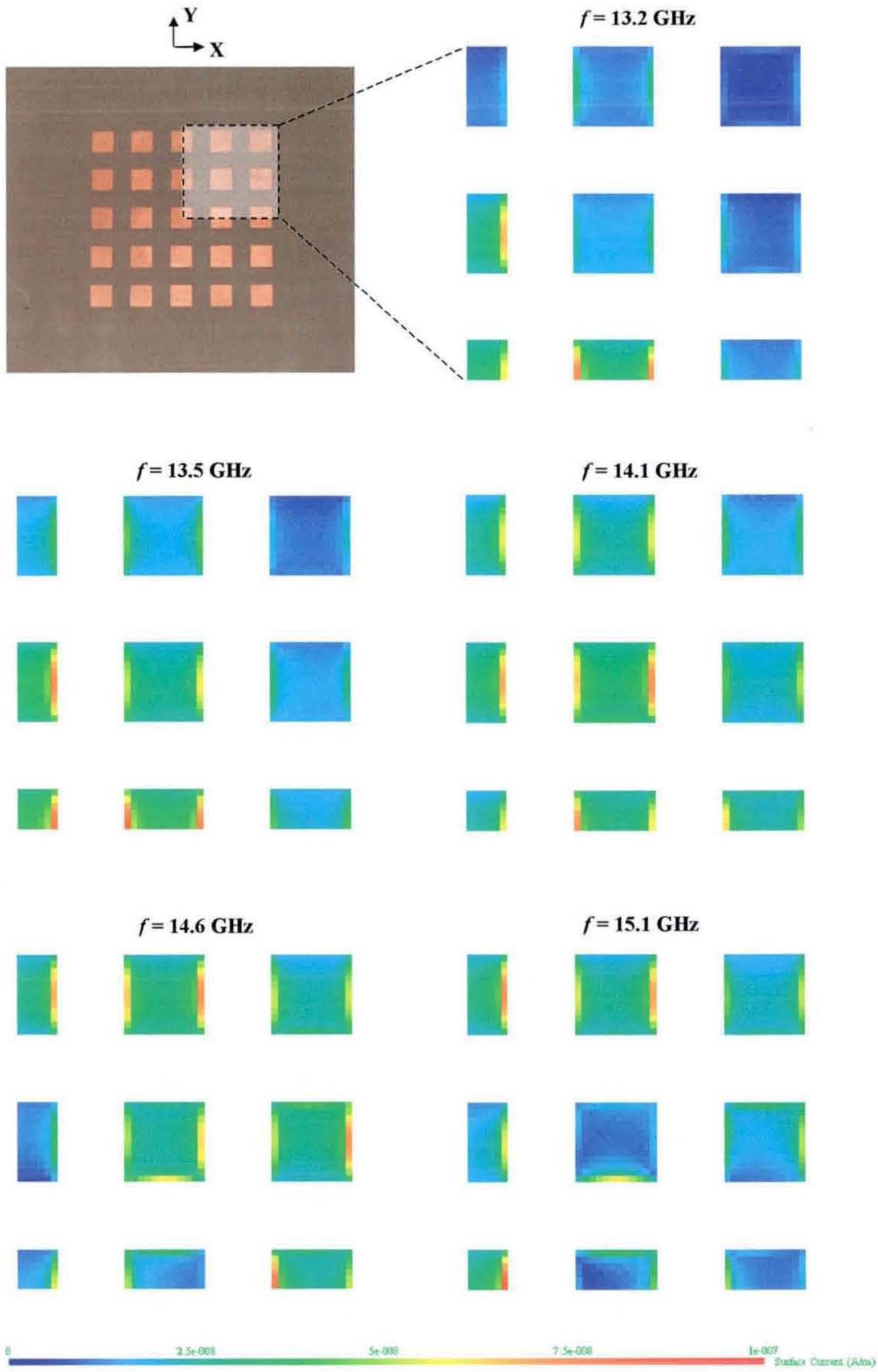

Figure 4.31 Total surface current density (magnitude) on square patches of second layer

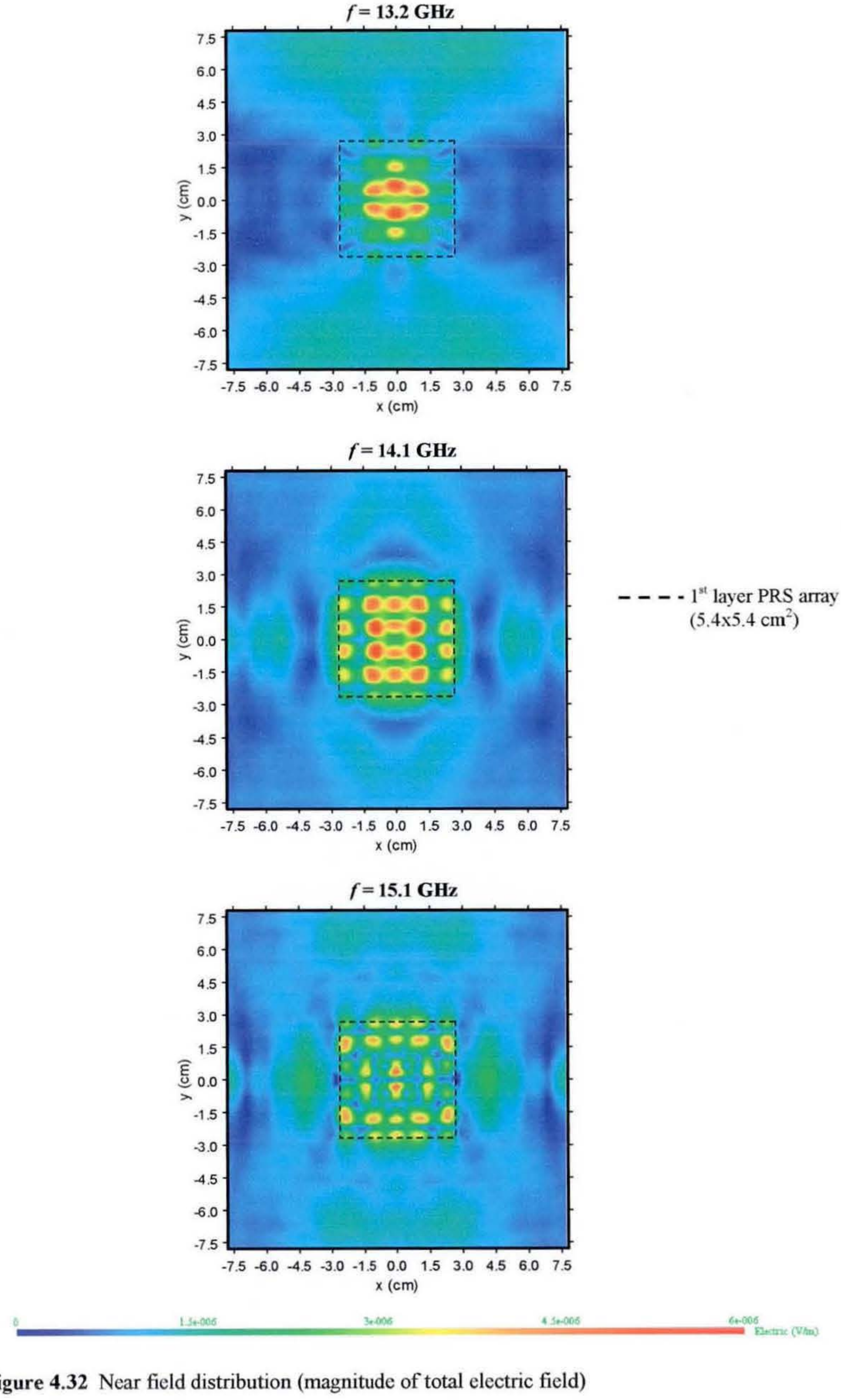

Figure 4.32 Near field distribution (magnitude of total electric field)

4.6 Conclusions

The performance of double layer arrays in a leaky-wave antenna configuration has been investigated. A novel double layer PRS design has been discovered, whereby the phase of the PRS reflection coefficient (under plane-wave illumination) increases with frequency in a certain frequency range. This was achieved by using optimised double layer arrays with different element dimension in each layer and separation distance of about half wavelength. The characteristic phase response resulted in a significant bandwidth enhancement of the leaky-wave antenna.

A double layer dipole PRS has been used to form a leaky-wave antenna, fed by a waveguide aperture in a ground plane. High gain (19dBi) and broad bandwidth (7%) has been achieved for the optimum aperture size. The maximum antenna efficiency was 56%. However, the matching of the antenna was poor. The antenna has been simulated in its entirety using LC and the results were in good agreement with measurements. The antenna matching has been improved with the use of a waveguide-fed slot as feeder. From this stage onwards, Microstripes has been used for 3D simulations of the antenna. A double layer square patch PRS has been designed and has been used to form a slot-fed leaky-wave antenna prototype. A maximum antenna gain of 17.5 dBi has been obtained with a broad bandwidth of more than 10%. High antenna efficiency (76%) and good return loss has been achieved. Simulation results were in satisfactory agreement with measurements and, furthermore, provided a valuable insight into the surface currents and near fields of the antenna.

References

[1] MUNK, B. A. : 'Frequency Selective Surfaces: Theory and Design', John Wiley & Sons Inc., New York, 2000 (pp. 279-314)

[2] VERDEYEN, J. T. : 'Laser electronics', Prentice Hall Inc., 1989

[3] VARDAXOGLOU, J. C. : 'Frequency Selective Surfaces: Analysis and Design', Research Studies Press, Somerset, England, 1997

[4] FERESIDIS, A. P. and VARDAXOGLOU, J. C. : 'Double layer partially reflective surfaces for high gain planar antennas', Proc. IEEE International Conference on Electromagnetics in Advanced Applications (ICEAA), Torino, Italy, September 2001, pp. 243-246

[5] POZAR, D. M. : 'Microwave Engineering', John Wiley, New York, 1998

[6] COLLIN, R. E. : 'Foundations for Microwave Engineering', McGraw-Hill, New York, 1992

Chapter 5

Cavity and Multiple Feed Antenna Designs

5.1 Introduction

Designs of the broadband planar leaky-wave antenna with two new feeding techniques are presented in this chapter. The first design is based on metallic cavity walls placed around the PRS and attached to the ground plane. The antenna design presented in section 4.5 is used as the basis of the design. It has been shown in section 4.5 that when high diffracted fields appear in the *H*- or *E*-plane, the corresponding radiation patterns suffer from high SLL values. The role of the cavity walls would be to reduce diffracted fields around the edges of finite size PRSs and stop the energy spreading away from the antenna radiating aperture. This would increase the antenna gain and efficiency. An investigation is carried out with regard to the effect of the size and length of the cavity to the antenna performance. The study is carried out in Microstripes. An open-cavity-fed antenna has been manufactured and measured.

The second design is based on a multiple feed strategy. The illumination of the PRSs in the antenna design of section 4.5 could be improved by the use of more than one feeding slots. A 2×2 array of slots is used as a feeder. The antenna performance is studied using simulation results obtained in Microstripes for different slot array periodicity. Although a large slot array periodicity would result in the appearance of grating lobes in the radiation patterns, this is not expected to be the case in the leaky-wave antenna configuration. This is because, due to the spacing of the PRS from the ground plane (about half wavelength), Huygens principle could apply approximately and thus the PRS array could be considered as the radiation source of the antenna instead of the primary slot array. Following this idea, an investigation is carried out into the effect of the slot array periodicity on the antenna radiation patterns.

5.2 Cavity-Fed Antenna

The diffraction effects due to the finite size of PRSs in the leaky-wave antenna have been discussed in section 4.5 for the double layer square patch PRS (5.4×5.4 cm^2). The relatively high values of the diffracted fields may deteriorate the antenna performance. In particular, it has been shown that when high diffracted fields appear in *H*- or *E*-plane the corresponding radiation patterns suffer from high SLL values. A way to reduce the diffraction fields and stop the energy spreading away from the PRSs is to form an open cavity by placing metallic walls around the PRSs and attached to the ground plane. A schematic diagram of the cross section of the proposed structure is shown in Fig. 5.1, where the cavity extents only until the first layer. The cavity keeps the energy near the radiating aperture of the antenna, thus improving its aperture efficiency and gain performance. However, additional modes may appear in the cavity due to its large size (over-moded cavity), which would affect the illumination of the PRSs.

A study has been carried out on the effect of the cavity size on the antenna performance. The double layer square patch PRS design, presented in section 4.5, has been used. The study was based on simulation results obtained in Microstripes. The cavity size in the *xy* plane as well as its length, *h*, were investigated for their effect on the antenna performance.

After the simulations, an open-cavity-fed antenna was manufactured. The measured results verified the simulation predictions.

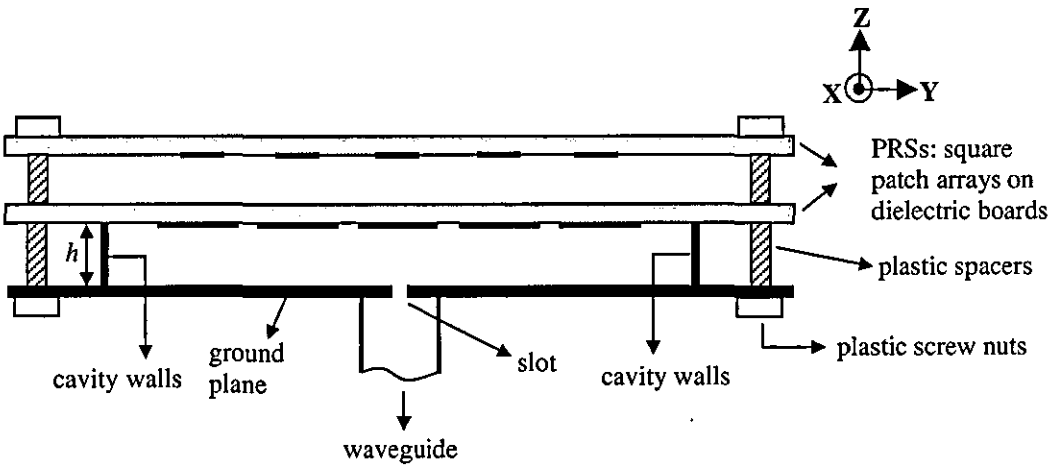

Figure 5.1 Schematic diagram of leaky-wave antenna with open cavity feed and double layer PRS.

5.2.1 Simulations

The open cavity has been included in the Microstripes model of the antenna presented in section 4.5. The thickness of the cavity walls was 1mm. In order to reduce the computational requirements the part of the ground plane and the dielectric boards extending outside the size of the cavity has not been taken into account. A number of simulations have been carried out to investigate the effects of the size and length of the cavity on the antenna performance.

The cavity was initially modelled with dimensions 5.8×5.8 cm^2, i.e. it was closely spaced around the square patch array. The simulation required 140 Mb of memory and took 3.7 hours for 12,500 time steps on a 1.2 GHz Athlon PC. In addition, the antenna has been simulated with a larger size cavity of 8×8 cm^2. The memory requirements of this model were 200 Mb and it took 5 hours to run for 12,500 time steps. In both cases, the cavity was modelled to extend only until the first PRS array (h = 11.4 mm). The value of h is slightly larger than the resonant distance used in section 4.5, because it was found that for this distance, the gain was a little more uniform with frequency. Fig. 5.2 shows the simulated gain of the antenna against frequency for both cavity sizes. The small size cavity deteriorates the broadband antenna performance, showed in Fig. 4.26. In contrast, the 8×8 cm^2 cavity gives a broad bandwidth as well as higher gain.

Using the 8×8 cm^2 open cavity in the antenna model, the effect of the cavity length on the antenna performance was investigated. Fig. 5.3 shows the simulated gain of the antenna with the cavity extending to the first and to the second PRS layer with length h = 11.4 mm and h = 23.9 mm respectively. The gain obtained with the short cavity is about 1 dB higher than that obtained with the longer cavity, throughout the whole of the operating frequency range.

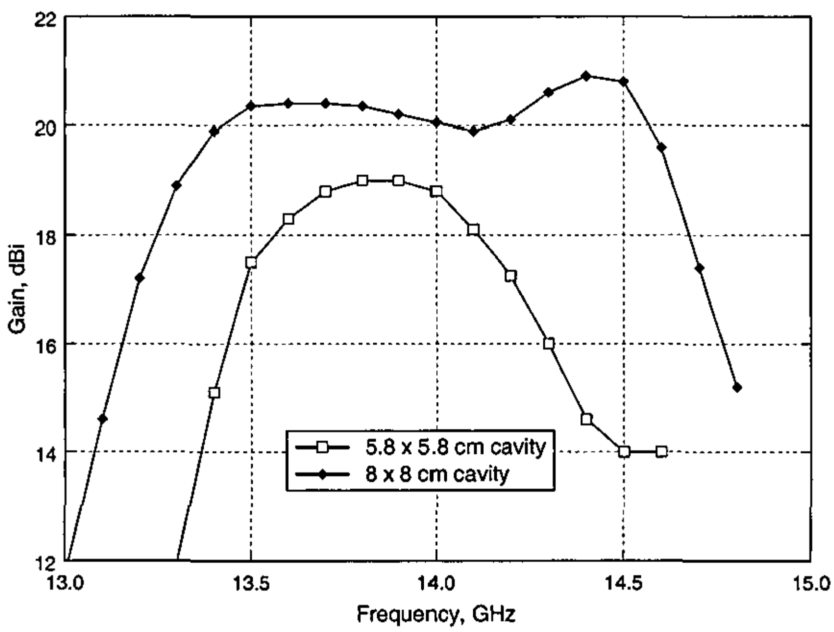

Figure 5.2 Gain of antenna with different cavity dimensions (h = 11.4 mm).

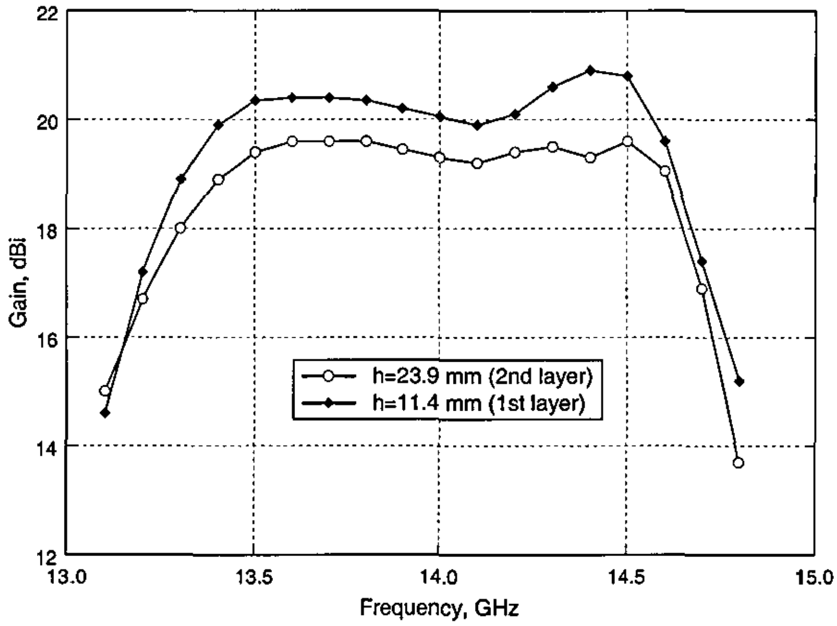

Figure 5.3 Gain of antenna with 8×8 cm^2 cavity of different lengths (h).

5.2.2 Antenna performance

A metallic frame has been manufactured in order to form the 8×8 cm^2 open cavity structure as discussed in the previous section. Due to manufacturing tolerance errors, the size of the frame (cavity) was actually 8.1×7.9 cm^2 (x×y). Its length was 11.4 mm with a tolerance of $\pm$0.05 mm. The frame was placed between the ground plane and the first PRS layer of the antenna shown in the photograph in Fig. 4.23 in order to form the open-cavity-fed antenna structure. It was centred to the feeding slot and attached to the ground plane using copper tape glued on the external part of the frame. The largest dimension (8.1 cm) was along the x-axis (H-plane) and the shortest (7.9 cm) along y-axis (E-plane). A cross sectional view of the antenna is shown in Fig. 5.1.

The antenna gain was measured and is shown in Fig. 5.4. In the same figure the simulated gain of the antenna with the actual cavity dimensions is shown. A maximum gain of 20 dBi has been obtained. A gain increase of 2.5 dB (at 13.5 GHz) to 3.5 dB (at centre frequency, 14 GHz) has been achieved, as compared to the gain of the antenna without the cavity (see section 4.5). Furthermore, the gain of the cavity-fed antenna is more uniform with frequency. The antenna is quite broadband with a 3 dB fractional bandwidth of more than 11%. The measured and simulated return loss is shown in Fig. 5.5. There are not significant differences in the return loss compared to that of the antenna without the cavity. Simulation results of both gain and return loss are in good agreement with measurements. Some discrepancies could be attributed to manufacturing tolerance errors (cavity frame, slot, spacing of the PRSs).

The overall antenna efficiency can be calculated by Eqn. (3.9). However, if the size of the larger PRS array (5.4×5.4 cm^2) was taken as the antenna radiating aperture, then efficiency values larger than 100% would be obtained. In reality, the radiating aperture should be taken equal to the size of the open cavity (8.1×7.9 cm^2) due to the high fields at the area between the cavity walls and the PRS edges. The field distributions are shown later on. Thus, the maximum antenna efficiency is 60% at 13.5 GHz, it drops to 50% at the centre frequency (14 GHz) and increases again to 54% at 14.5 GHz.

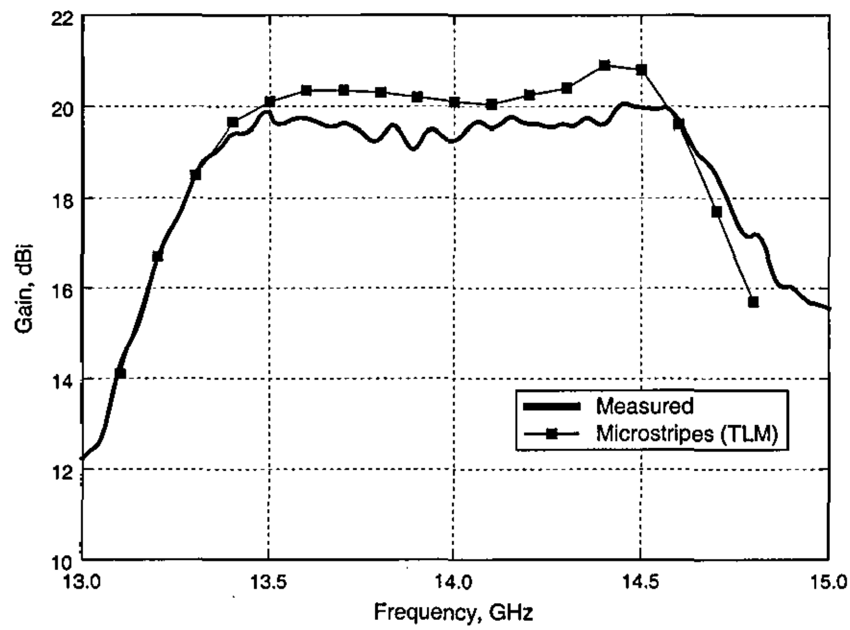

Figure 5.4 Gain of open-cavity-fed antenna with double layer square patch PRS.

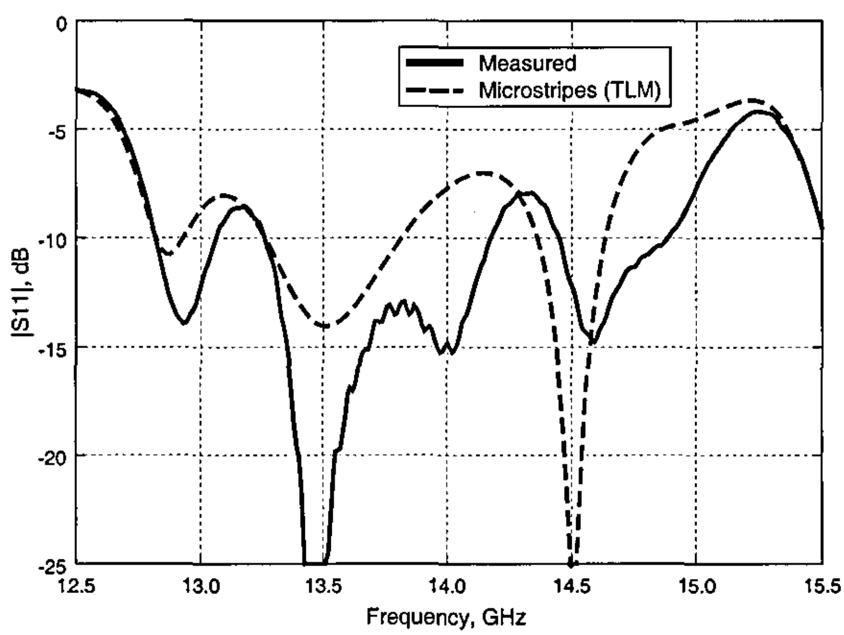

Figure 5.5 Return loss of open-cavity-fed antenna with double layer square patch PRS

The radiation patterns of the antenna with the open cavity have been measured at several frequencies throughout the operating frequency band and they are shown in Fig. 5.6 (*H*-plane) and Fig. 5.7 (*E*-plane). In general, lower SLL has been achieved, as compared to the patterns of the antenna without the cavity. In addition, the sidelobes now appear in lower angles, between 20 and 30 degrees. The improved SLL performance as well as the high gain is due to the concentration of the diffracted fields near the PRS arrays.

The near field distribution (magnitude of total electric field) has been obtained in Microstripes. Fig. 5.8 shows the field distribution for a surface of 15×15 cm^2 at a distance of 1 mm over the front end of the antenna. The field is shown at the centre frequency (14 GHz) as well as at the edges of the operating frequency band. The size of the square patch array in the first layer is depicted with a dashed line. A comparison with Fig. 4.32 (section 4.5.3) reveals the improvements achieved with the use of the open cavity. The diffracted fields are lower, particularly at the centre frequency, where most of the energy is concentrated within the antenna radiating aperture. As a result, the field over the PRSs is higher.

In addition to the near field, the field over the first PRS (at the upper surface of the dielectric board) is shown in Fig. 5.9, at centre frequency (14 GHz). For comparison, the corresponding field distribution at centre frequency (14.1 GHz) of the antenna without the cavity is also shown in the same figure. The effect of the cavity is evident. The cavity walls keep the field near the PRS edges, whereas without the cavity it would spread away from the PRS. As a result the field diffracted from the PRS, in the cavity-fed antenna, is concentrated inside the cavity walls (near the PRS) and has higher maximum values. This is the reason why the effective radiating aperture of the antenna should be considered to be equal to the size of the cavity and not the PRS alone.

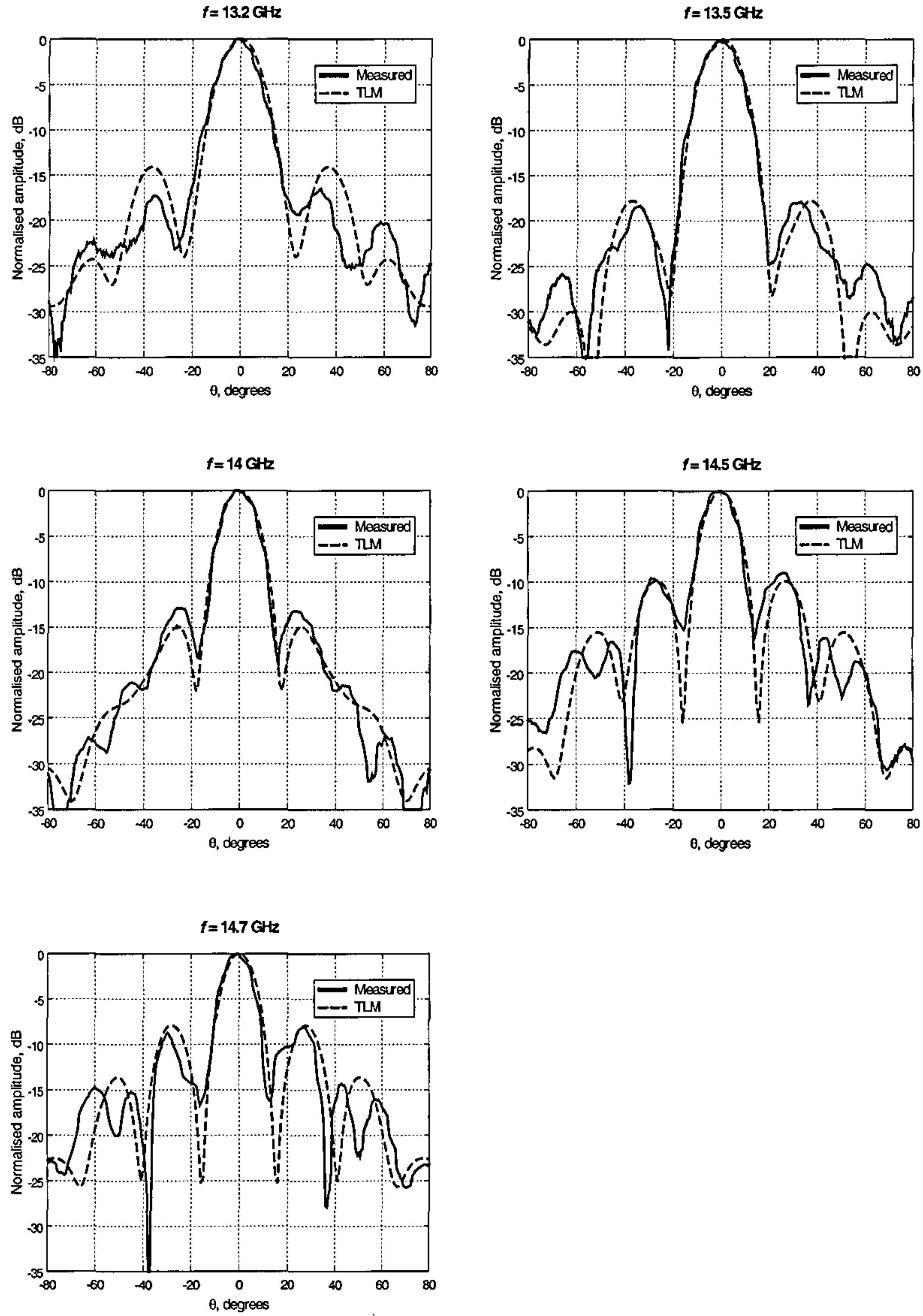

Figure 5.6 H-plane radiation patterns of antenna at several frequencies

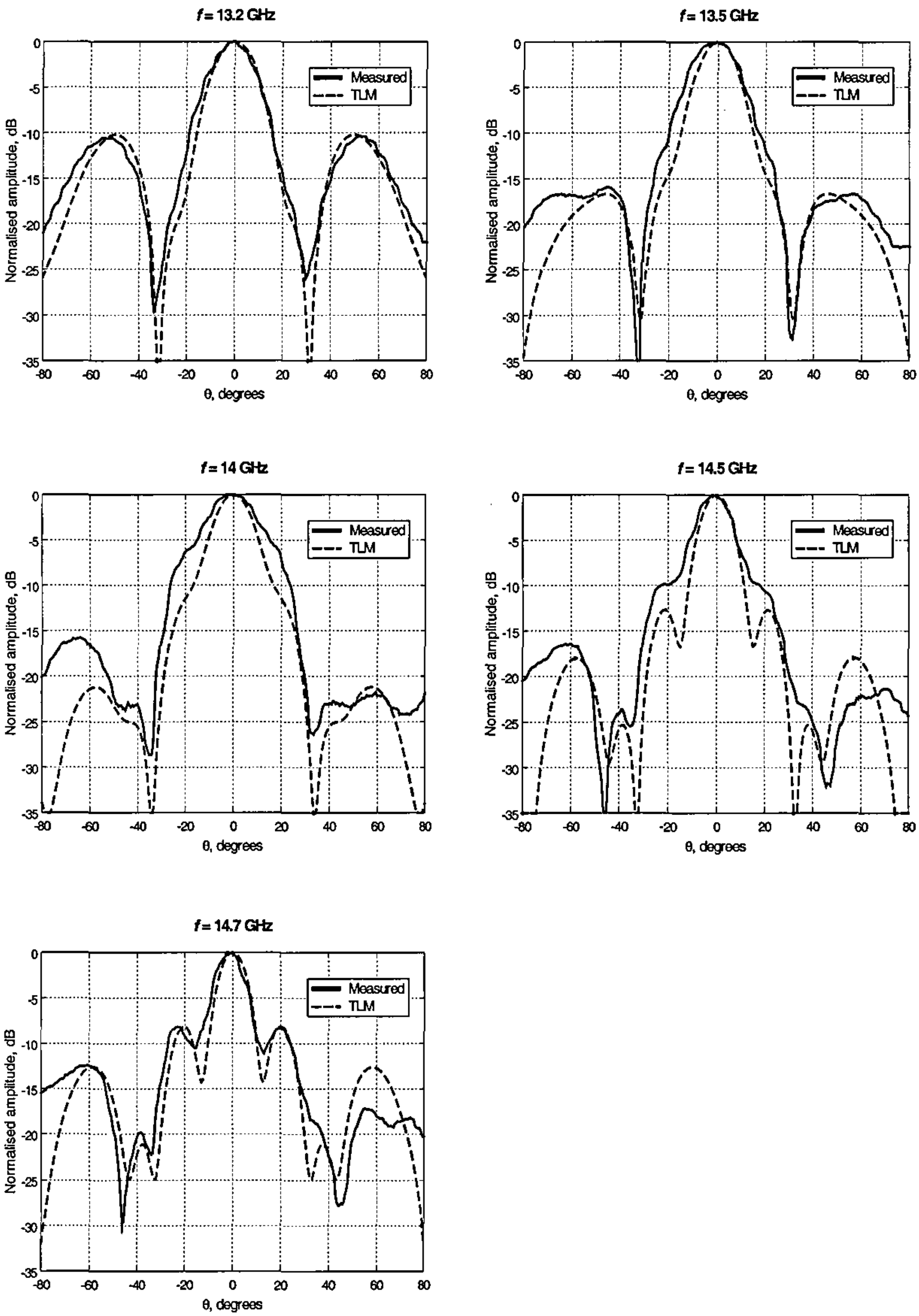

Figure 5.7 E-plane radiation patterns of antenna at several frequencies

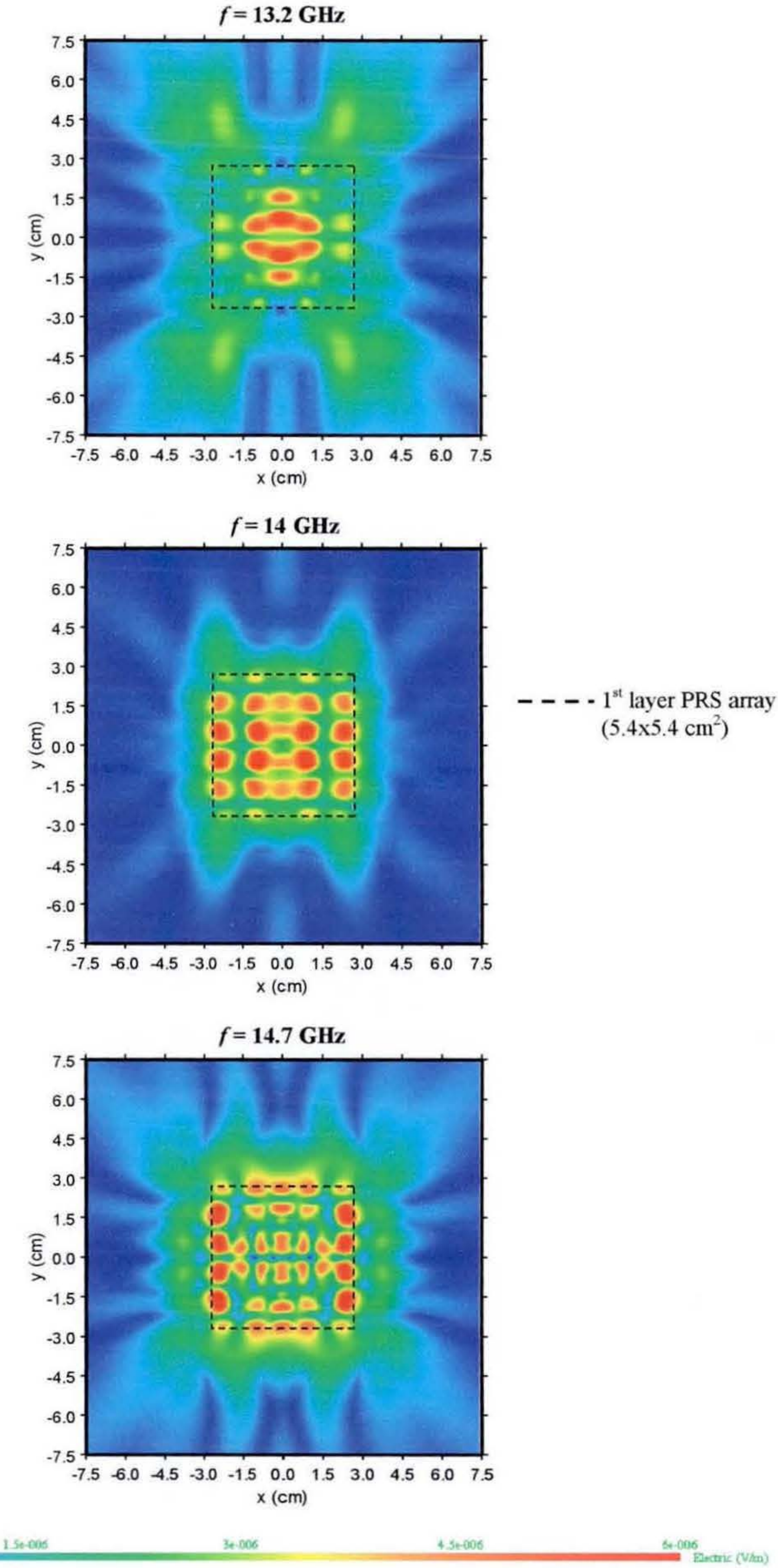

Figure 5.8 Near field distribution (magnitude of total electric field)

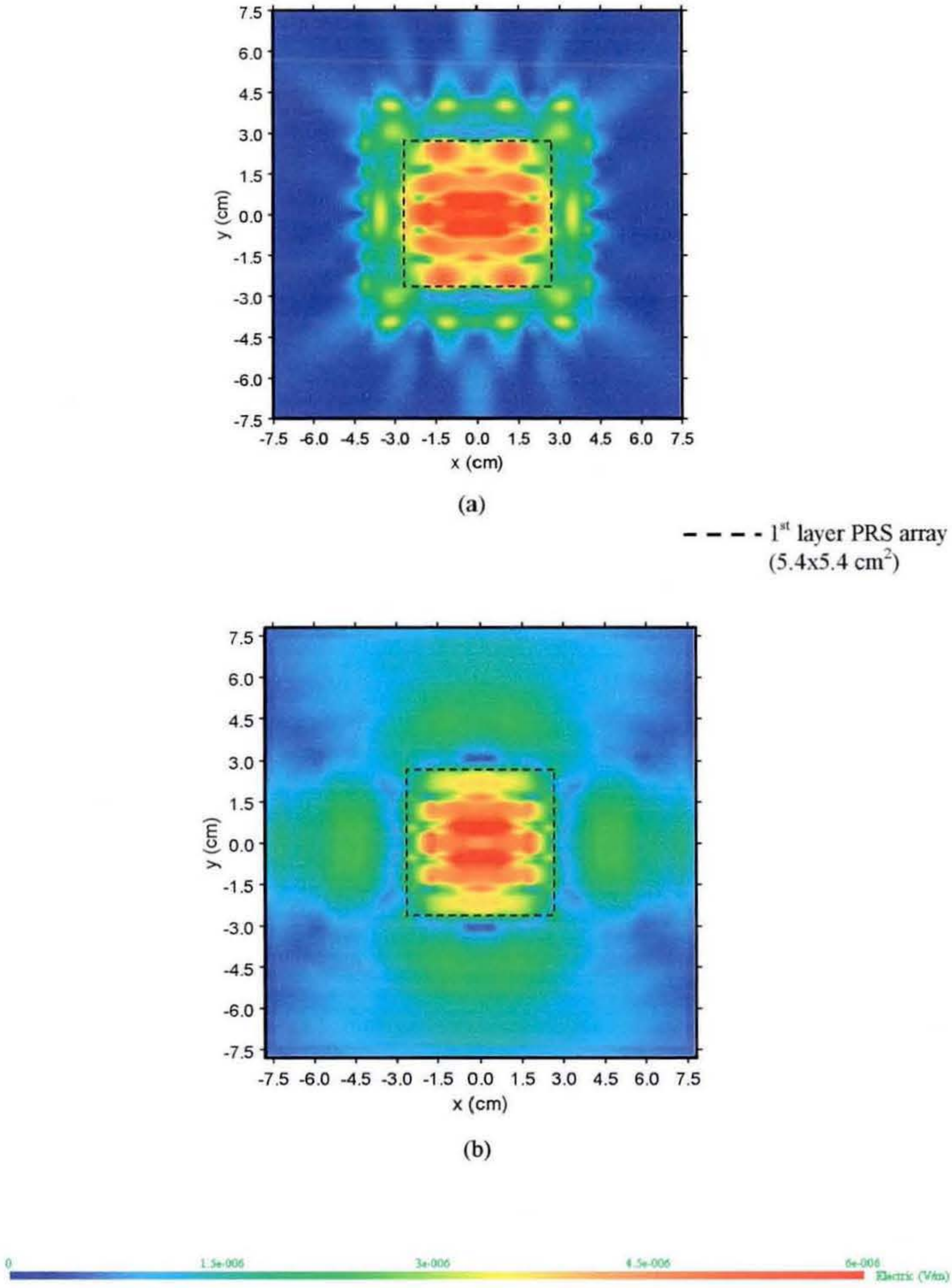

Figure 5.9 Magnitude of electric field over first PRS array at centre frequency, for the antenna: (a) with open cavity, (b) without open cavity

5.3 Multiple Feed Structure

A uniform illumination of a larger area of the PRS arrays in the leaky-wave antenna configuration would result in higher antenna gain and better aperture efficiency. The illumination of the PRSs can be improved by the use of a multiple feed structure. The presence of more than one feeders (e.g. slots as in the design of section 4.5) would result in an illumination of a larger area of the PRSs.

A 2×2 array of slots is proposed here as a feeding structure. A sketch of the proposed feeding structure is shown in Fig. 5.10. The slot array periodicity is D_s. The PRS design of section 4.5 is used. The spacing of the PRS from the feeding aperture is in the range of half wavelength. This allows for an approximate description of the antenna radiation by Huygens principle [1, 2]. According to Huygens principle the PRS arrays can be considered as the radiation source of the antenna (secondary radiation), instead of the primary slot array. Thus, widely spaced slots could be used in order to achieve an excitation of larger area of the PRS with a simple feed structure. The grating lobes of the primary slot array due to large array periodicity, D_s, are not expected to appear in the radiation patterns of the antenna, since the radiating aperture consists of the PRS arrays. However, they could affect the uniformity of the illumination of the PRS. A uniform PRS illumination would be needed in order to avoid high sidelobe level and the appearance of grating lobes in the antenna radiation patterns.

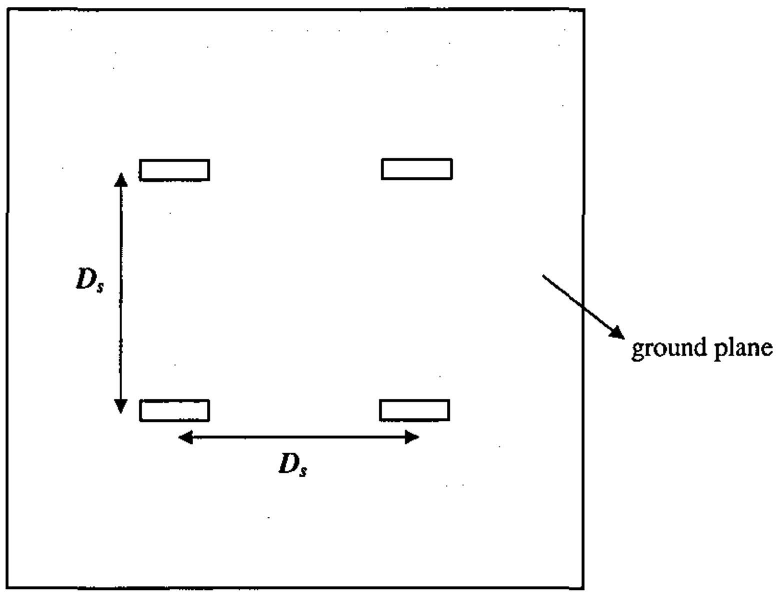

Figure 5.10 Sketch of the 2×2 slot array in the ground plane

An investigation has been carried out on the effect of the spacing of the slots in the antenna performance. The investigation was based on simulation results obtained in Microstripes. The double layer square patch PRS design and the 15×15 cm^2 ground plane (section 4.5 and 5.2) have been used to form the antenna. The slot size dimensions are the same (L=10mm, W=2mm) as in the designs of the previous sections. Symmetry conditions (magnetic and electric walls) have been used in the antenna model in Microstripes, thus only a quarter of the antenna has been included in the TLM model. The slots in the model were fed by separate waveguides instead of a waveguide network including E and H-splitters, which would have been used if the antenna was manufactured. Thus, the losses and mismatch effects in the waveguide feeding network are not taken into account here, although they are expected to be small.

Initially a slot array periodicity of $D_s = 5.5\,\text{cm}$ has been used. The PRS array consisted of 10×10 square patches, i.e. its size was 10.9×10.9 cm^2 (on the first layer). The resonant distance of the first PRS form the ground plane was 11.5 mm and the separation of the two PRSs 11 mm. The simulation required 500 Mb of memory (3.7 million cells) and it took 15 hours on a 1.2 GHz Athlon PC for 12,400 time steps. A gain of more than 23 dBi has been achieved, as shown in Fig. 5.11. The 3dB fractional bandwidth is more than 8%. The return loss is quite low (less than 10 dB) in the frequency band of high gain, as shown in Fig. 5.12. However, the radiation patterns obtained from this design exhibit high SLL due to a distorted main lobe. The patterns are shown in Fig. 5.13 (*H*-plane) and Fig. 5.14 (*E*-plane) for three representative frequencies. The poor SLL performance can be attributed to the non-uniform illumination of the PRSs, due to the large periodicity, D_s, of the feeding slot array. The large periodicity D_s also results in the appearance of grating lobes in the radiation pattern of the primary slot array, which deteriorates the uniform illumination of the PRS.

A better SLL performance has been obtained using $D_s = 3.3\,\text{cm}$. The slots are still widely spaced, since $D_s \approx 1.5\lambda_0$, where λ_0 is the free space wavelength. Each PRS array consisted of 8×8 square patches, i.e. a total array size of 8.7×8.7 cm^2 (first layer). Larger PRS size does not result in higher gain. The gain of the new design is also shown in Fig. 5.11. The maximum gain value is 22 dBi, thus it is reduced by about 1 dB as compared to the previous design. The antenna efficiency however is quite high, with a maximum of 85% (at 13.3 GHz). The bandwidth is quite wide, about 9.5%. The return loss is better than 14dB in the operating frequency band. Furthermore, a better SLL performance has been obtained. The radiation patterns are shown in Fig. 5.13 (*H*-plane) and Fig. 5.14 (*E*-plane), superimposed on those obtained with the slot array of larger periodicity. The improvement in the radiation patterns reveals a more uniform illumination of the PRS arrays, which is expected due to the smaller periodicity of the slot array. In addition, the grating lobes of the primary slot array due to the large periodicity ($D_s \approx 1.5\lambda_0$) do not appear in the radiation patterns of the antenna and low SLL is achieved.

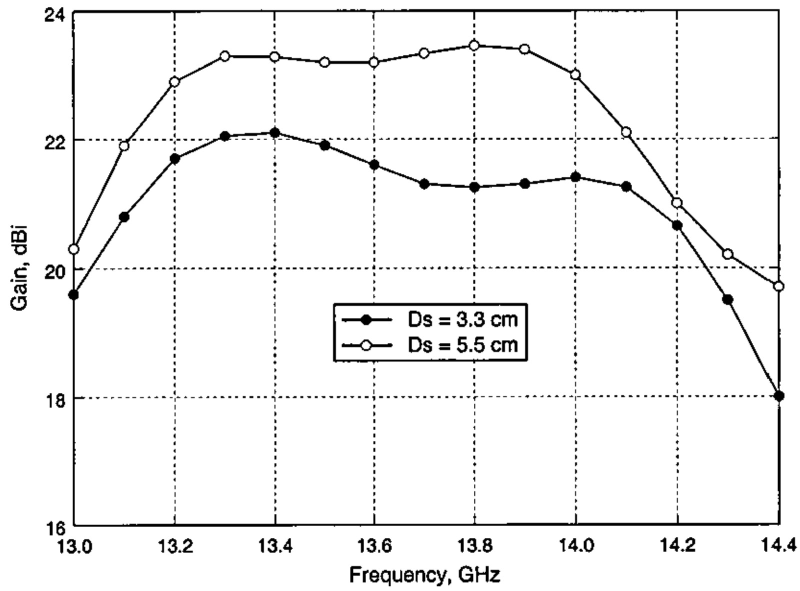

Figure 5.11 Gain of antenna fed by a 2×2 slot array with different periodicity

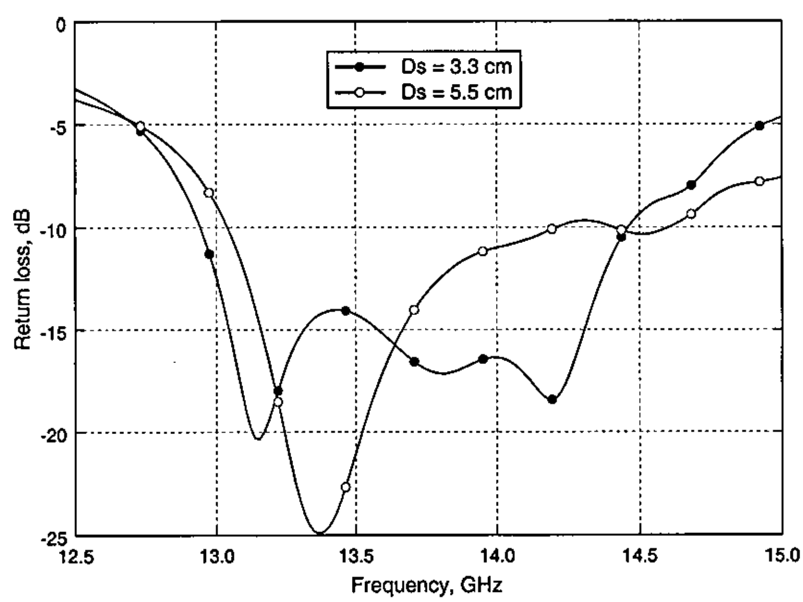

Figure 5.12 Return loss of antenna fed by a 2×2 slot array with different periodicity

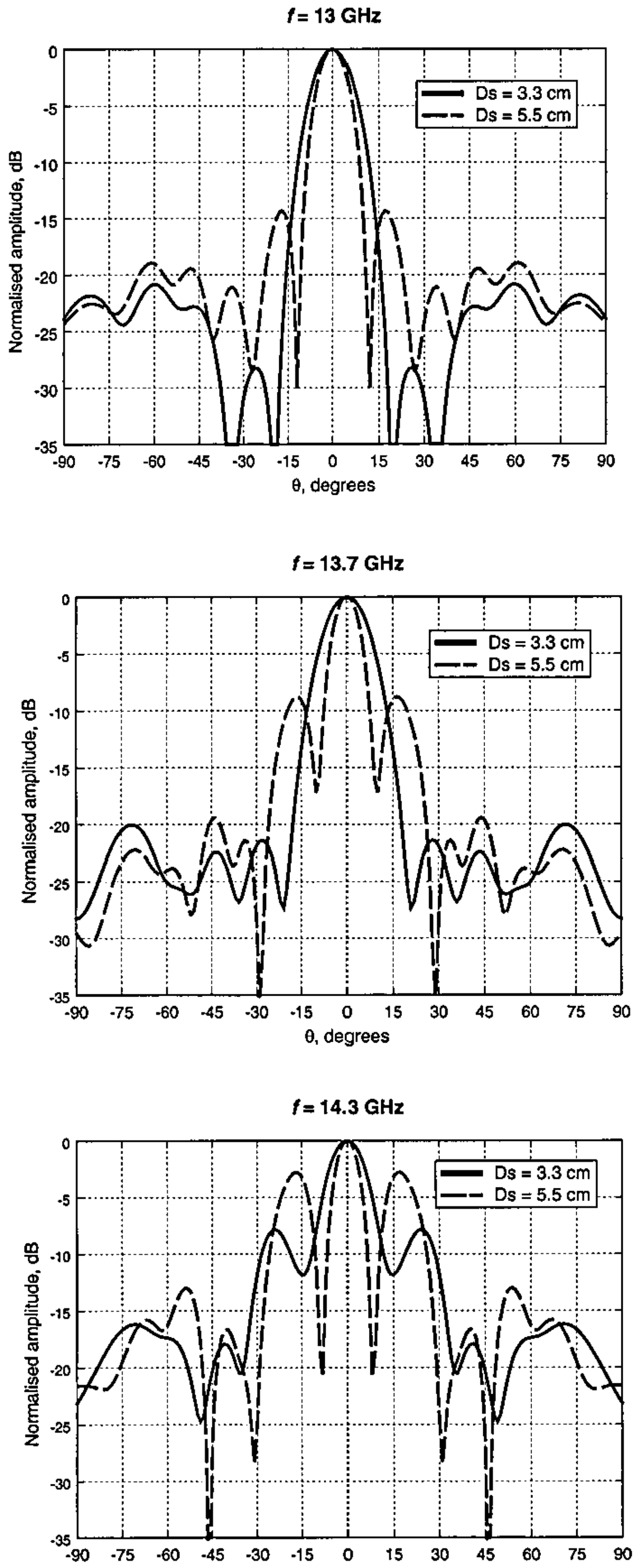

Figure 5.13 H-plane radiation patterns of antenna fed by a 2×2 slot array with different periodicity

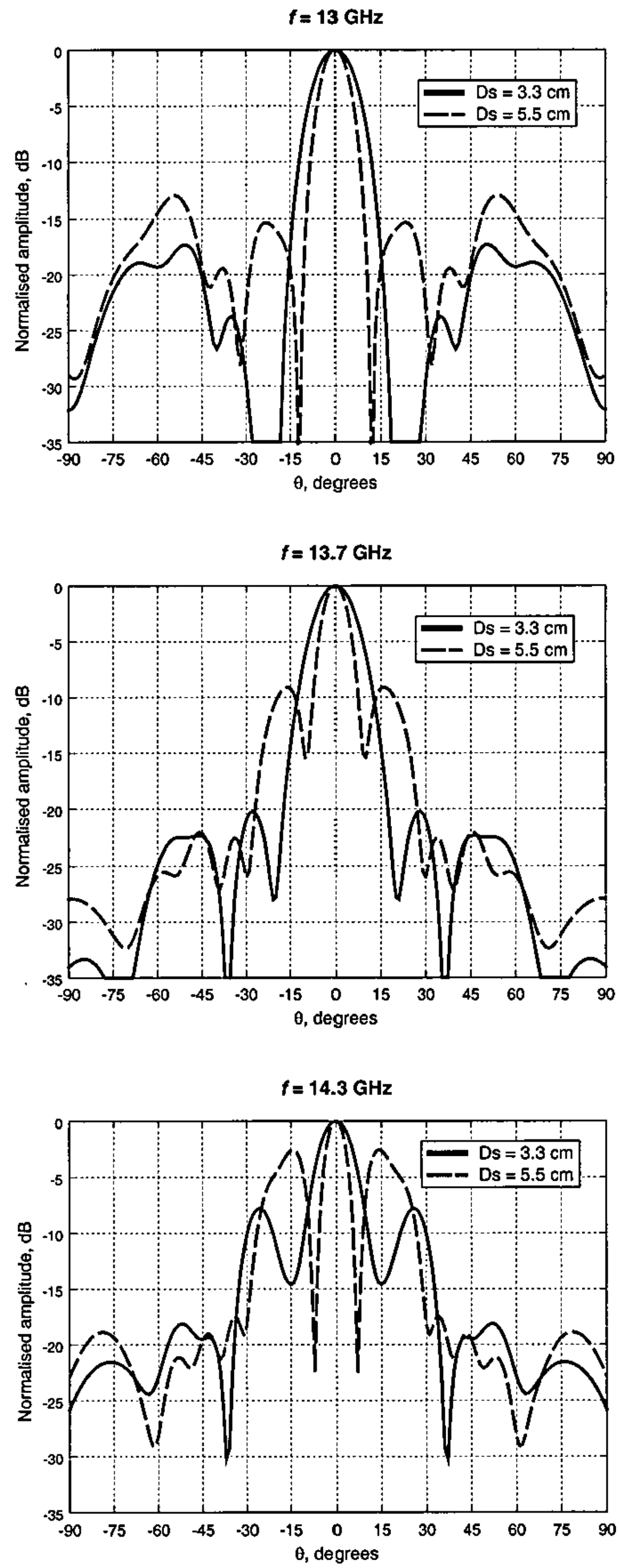

Figure 5.14 E-plane radiation patterns of antenna fed by a 2×2 slot array with different periodicity

5.4 Conclusions

Two improved designs of the broadband leaky-wave antenna have been presented in this chapter. At first, an open cavity of 8×8 cm^2 size and 11.4 mm length was placed between the ground plane and the first PRS of the design presented in section 4.5, resulting in higher and more uniform (with frequency) gain and better SLL. The cavity size and length was determined from simulation results. The maximum gain obtained was 20 dBi, which corresponds to a gain increase of 3.5 dB compared to that of the antenna without the cavity. A visualisation of the simulated near field of the antenna as well as the field over the first PRS demonstrates the concentration of the diffracted fields near the PRSs and explains the improved performance.

A multiple feed structure has also been studied based on simulation results. A 2×2 array of widely spaced slots was used as a feeder. The results show a significant increase in antenna gain and efficiency, which indicates that a larger area of the PRS array is excited and also the PRS illumination is quite uniform. A maximum gain of 22 dBi and low SLL values have been obtained for a slot array periodicity of 3.3 cm.

References

[1] HECHT, E. : 'Optics', Addison-Wesley, Reading, Mass., 1990

[2] BALANIS, C. A. : 'Antenna Theory: Analysis and Design', John Wiley, New York, 1997

Chapter 6

Conclusions

This thesis has researched and described a study into the beamforming effect of planar single and double layer PRSs in a leaky-wave antenna configuration and presented novel broadband high-gain leaky-wave antenna designs. A GO approach has been used in conjunction with a plane-wave modal analysis of the PRS array for an initial prediction of the antenna gain and radiation patterns. Although the analysis of the antenna was only approximate it provided a valuable insight into the dependence of the antenna performance on the geometry of the PRS. As a result, design guidelines have been produced for the optimisation of the PRS for high gain and wideband antenna performance.

Single layer PRSs have been investigated in the leaky-wave antenna configuration with a grounded waveguide aperture used as a feeder. An improved ray analysis of the antenna has been achieved by using a plane-wave modal PRS analysis which takes into account the angle of incidence in the calculation of the PRS reflection coefficient. The ray analysis has predicted the radiation patterns of large ($\approx 10\lambda$) PRSs with a satisfactory agreement. Using the plane wave modal analysis, an optimisation study has been carried out in order to produce PRS designs with reflection characteristics similar to the optimum ones as laid out from the approximate analysis. A planar leaky-wave antenna with a high gain of 22 dBi and improved bandwidth has been produced using an optimised dipole PRS. In order to take into account the finite size of the PRS, the antenna with a 10×10 cm^2 dipole PRS has been simulated in Ensemble. The edge effects due to the small PRS size have been modelled, however approximations have been made regarding the waveguide aperture feed and the size of the ground plane. Simulation results verified the improved performance of the antenna with the optimised PRS. In addition to Ensemble, a 3D FDTD code (LC) has been used to simulate the antenna in its entirety. A good agreement between measured and simulation results has been achieved. The effect of the size of the optimised dipole PRS on the antenna gain has also been investigated experimentally. The study showed that the 10×10 cm^2 is the optimum PRS size for maximum antenna efficiency (54%).

A further bandwidth enhancement of the leaky-wave antenna has been achieved using double layer PRSs. A novel double layer PRS design has been produced whereby the two layers are separated by about half wavelength and have different element dimensions. The design results in a plane-wave array response whereby the reflection phase increases with frequency in a certain range. This phase response meets the optimum PRS reflection characteristics in a better degree. A double layer dipole PRS design has been produced used to form an antenna with 19 dBi gain and over 7% fractional bandwidth. However, the matching of the antenna was poor. The size of the PRS has been optimised for maximum gain after an experimental study. FDTD simulation results were in good agreement with measurements. A waveguide-fed slot has been subsequently designed in order to improve the antenna matching. In this stage a TLM based simulation package, Microstripes, has been used. In addition, an optimised double layer square patch PRS has been designed and the leaky-wave antenna has been manufactured in a more rigid structure. A PRS size of 5.4×5.4 cm^2 proved to exhibit a better antenna gain performance as it was obtained in measurements. A maximum antenna gain of 17.5 dBi has been achieved with a broad bandwidth of more than 10%. High efficiency values of 50% to 76% have been obtained throughout the operating frequency band of the antenna. A good return loss has also been achieved. Simulation results in Microstripes were in satisfactory agreement with measurements and moreover provided the surface currents and near fields of the antenna.

The gain of the broadband leaky-wave antenna with the double layer square patch PRS has been increased further to 20 dBi by using an open cavity feed technique. The size of the metallic cavity has been optimised after simulations in Microstripes. Measurements were in good agreement with simulation predictions. The antenna bandwidth was more than 11% and the return loss was not affected significantly by the presence of the cavity. A multiple feed technique has finally been investigated based on simulation results. A 2×2 array of widely spaced slots has been used as a feeder. This improved the illumination of the PRS and resulted in an antenna gain of 22 dBi. A low SLL in the radiation patterns has also been achieved.

The broadband high-gain leaky-wave antenna designs presented in this thesis could be used as the basis for specific high-gain antenna designs. The gain could be further increased with a multiple feed technique in conjunction with a cavity feed. A slot feed array fed by microstrip lines could offer the advantage of a more simple fabrication method. The wide spacing of the slots reduces dramatically the complexity of the feeding structure, as compared to that of microstrip arrays. Furthermore, the implementation of the leaky-wave antenna designs with aperture PRS arrays could be investigated. An antenna design with perforated screens as PRSs would dispense with the need for dielectric substrates and their losses, particularly in millimetre wave frequencies.

By scaling the dimensions, the high-gain planar antenna can be designed for several applications at different frequency bands. It can be developed for use in the LMDS system (28GHz), where a high gain of over 26dBi and a bandwidth of about 8% is required. Furthermore, the antenna could be designed with a dual or circular polarisation (CP) feeder in order to be used for satellite reception at 10 GHz to 12 GHz. In addition, further study could be carried out into a multi-band antenna design for point to multipoint links. In order to operate in more than one frequency bands, the antenna would require a multiple feed in conjunction with an appropriate multi-band design of the arrays.

The flat plate antenna has the advantage that it can be conformal to building walls or roofs. However, further development in the antenna design would be needed for beam tilting. This could be achieved by changing the geometry of the leaky-wave arrays, possibly using a non-uniform array geometry. Moreover, the use of existing techniques for active arrays could result in an active antenna design, for example active beam steering.